Fast Neutron Resonance Radiography for Elemental Imaging: Theory and Applications

by

Gongyin Chen

B. Eng. in Engineering Physics, Tsinghua University, 1991

M.S. in Nuclear Engineering, MIT, 1999

Submitted to the Department of Nuclear Engineering

in Partial Fulfillment of the Requirements for the Degree of

Doctor of Philosophy in Nuclear Engineering

AT THE

MASSACHUSETTS INSTITUTE OF TECHNOLOGY

April 2001

[June 2001]

Signature of Author _____

Department of Nuclear Engineering

April 24, 2001

Certified by _____

Dr. Richard C. Lanza

Department of Nuclear Engineering

Thesis Advisor

Certified by _____

Assistant Professor Kenneth R. Czerwinski

Department of Nuclear Engineering

Thesis Reader

Accepted by _____

Professor Sow-Hsin Chen

Chairman, Department Committee on Graduate Students

Fast Neutron Resonance Radiography for Elemental Imaging: Theory and Applications

By

Gongyin Chen

Submitted to the Department of Nuclear Engineering

on April 24, 2001, in partial fulfillment of the requirements for the degree of

Doctor of Philosophy in Nuclear Engineering

Abstract

Fast Neutron Resonance Radiography (NRR) has been devised as an elemental imaging method, with immediate applications to detecting explosives and drugs in passenger suitcases. In the NRR method, the 2-D elemental mapping of hydrogen, carbon, nitrogen, oxygen and the sum of other elements are obtained from fast neutron radiographic images taken at different neutron energies chosen to cover the resonance cross section features of one or more elements. A radiographic image provides the 2-D mapping of the sum of elemental contents (weighted by the attenuation coefficients) and transmission measurements taken at different neutron energies form a set of linear equations, which can be solved to map individual elemental contents. Explosives and drugs can be identified by their characteristic elemental composition. The object-detector assembly rotates around the neutron source and different energy (2-6 MeV) neutrons can be obtained at different angles from a DD neutron source. A fixed-energy RFQ (2.3 MeV deuteron energy) with a thick target (0.4-0.8 MeV) can be used to generate fast neutrons. The physics of image formation in fast neutron radiography has been studied and a thick (4 cm) plastic scintillator has been recommended as the neutron detector. Variance-checking median filters have been recommended for removing sparkles in the digital image and the direct Householder Transform has been used to solve the ill-conditioned Least-Squares problem. Source shielding for $2x10^9$ neutrons/second has been suggested.

Experiments and simulation have proven NRR to be effective. Explosives can be identified with their high nitrogen and oxygen content and drugs with their high C/O ratio. With a 10 μA deuteron current and 6 atmosphere-cm D_2 gas target, total imaging time for each piece is expected to be 1-2 minutes. Because multiple objects can be inspected at the same time, it is possible to meet the FAA standard of 8 seconds per piece. Spatial resolution of the image is estimated to be ~7.5 mm.

Thesis Supervisor: Richard C. Lanza
Title: Senior Research Scientist, Department of Nuclear Engineering

Thesis Reader: Kenneth R. Czerwinski
Title: Assistant Professor, Department of Nuclear Engineering

Acknowledgements

I would like to thank my thesis advisor, Dr. Richard C. Lanza, for his guidance and financial assistance in the past three years. His intelligence, energy, and broad knowledge have been very important for me in the whole research process and in the invention of the NRR method. His dedication, patience, humor and understanding made my experience with him enjoyable.

I thank my thesis reader, Professor Kenneth R. Czerwinski of Nuclear Engineering, for his critical reading and suggestions for the thesis.

Special thanks go to Professor Jeffrey S. Schweitzer of University of Connecticut for his help in the work and on the thesis. He was also my advisor and thesis reader.

Thanks also go to Professors Andrew C. Kadak and David G. Cory of Nuclear Engineering, for serving as my thesis committee members.

I would like to thank the following people for their assistance and inspiring discussions and suggestions:

- Professor Jacquelyn C. Yanch, David Gierga and Brandon Blackburn of MIT-LABA;
- Professor Gunter Kegel and Dr. David DeSimone of UMass Lowell;
- My fellow graduate students Eric R. Empey and Roberto Accorsi.
- Dr. James Hall of Lawrence Livermore National Laboratory.
- Mr. James A. Petrousky at the Office of National Drug Control Policy.
- Professor John I. W. Watterson of University of the Witwatersrand, South Africa.

This work is supported by:
the Office of National Drug Control Policy (ONDCP) under Contract DAAD07-98-C-0117 and the Federal Aviation Administration under Grant 93-G-053.

To Ming and Jiming for their smile

Contents

List of Figures

List of Tables

Chapter 1

Introduction

Neutron imaging using thermalized (25 meV) neutrons from reactors has long been used to image light elements, especially hydrogen within structures composed of heavy elements, such as metals. Thermal neutron radiography is often described as being complementary to conventional X-ray imaging in the sense that imaging with X-rays detects heavy elements, while imaging with neutrons detects light elements. Fast neutron radiography with neutron energies of more than 1 MeV opens up a new range of possibilities for non-destructive inspection. Fast neutrons may be used to image extremely dense objects e.g. uranium where the mass traversed by the incident beams is large and consequently X-ray transmission even at 10 MeV and above is not practical. In this thesis another aspect of fast neutron radiography has been investigated in which element specific resonances in total attenuation cross-sections which are in the 1 to 8 MeV range are exploited to enhance the contrast for imaging light elements such as carbon, oxygen and nitrogen. The goal of this work is to utilize this contrast enhancement mechanism to produce elementally resolved images of objects under inspection and thus to identify the material composition of the object.

This work was originally motivated by the need to develop methods for non-destructive inspection for the detection of explosives and other contraband in baggage and cargo. Other groups have used similar principles and applied them to problems in the minerals industry for detection of e.g. diamonds in a dense Kimberlite rock matrix. The practical problems associated with the minerals industry have led them to a somewhat different approach to their imaging methodology. In order to place the work of this thesis in context, the nature of the contraband detection problem and other methods, which have been used, for inspection will be briefly discussed.

1.1 Drugs and Explosives Detection

The United States of America is the major consuming market of narcotic drugs and the primary target of terrorist attacks [1 & 2]. Drug dependence is a chronic, relapsing disorder that exacts an enormous cost on individuals, families, businesses, communities, and nations. Terrorist bombings, especially those targeting civilian airplanes, greatly jeopardize the lives of the public.

Drugs and explosives are transported illegally by various methods. Large objects such as trucks or cargo containers are checked at the southwest (U.S.-Mexico) border for large amounts of drugs or other goods of interest, while passenger's luggage is screened for a small amount of explosives or drugs (100—300 grams) or for weapons at airports. There are a lot of techniques used or proposed for drug and explosive or other contraband detection.

There have been many governmental efforts to develop drugs and explosives detection technology, led by the Office of National Drug Control Policy (ONDCP) and the Federal Aviation Administration (FAA). In this thesis, Fast Neutron Resonance Radiography is proposed for 2-D elemental imaging. Great emphasis has been given to the imaging of systems of hydrogen, carbon, nitrogen, oxygen and other elements, which are the key elements for separating drugs and plastic explosives from ordinary organic goods. [3].

1.1.1 Methods in Use

We discuss the commonly used drugs and explosives detection methods in this section. Our interest is parcel or cargo inspection and therefore land mine detection is not included.

Manual Check

The oldest and perhaps the most reliable way of detecting hidden drugs and explosives is to check the suspected object manually. After the baggage or cargo container is opened and carefully searched, we can determine, with the highest confidence, whether an explosive device or an illegal drug presents.

Manual checking is slow, expensive and perhaps dangerous. In addition, it could violate privacy. Usually only some randomly selected or highly suspected items are checked manually.

Canine Detection

A detector dog and its handler is another old but still broadly used technique for drugs and explosives detection. Canine olfactory systems are capable of reacting to the vapor of a number of compounds in drugs or explosives. When a dog is trained to detect a substance, it learns to discriminate the vapor of that substance from other odors in the environment by reacting to the compound(s) and earns positive reinforcement from the handler.

A dog usually works for several hours a day but may not be willing to work at the required time. In addition, canine detection fails if no vapor is coming out of the package.

Trace Detection

Drugs and explosives can also be detected by trace contaminants such as vapor or particulate residue. Air samples are collected, condensed, and then analyzed, very often with ion mobility spectrometer (IMS) detectors. Ways of collecting samples range from sniffing the vapors to wiping the surface, but they all depend on contamination. This detection method is used to screen people and/or boarding passes.

Electrical (Metal) Detection

Metal detectors are widely used at security checkpoints. This method employs an electric field, which is disturbed if a conductor such as a metal component enters its field. Metal detectors are simple, cheap, effective and reliable in detecting hidden explosive devices or weapons if they contain metal components. Unfortunately, modern explosives (plastic explosive) can be made without metal and will escape a metal detector.

X-Ray Detection

X-ray detection systems are the most commonly used for parcel and cargo inspection. X-ray transmission radiography or tomography is based on the attenuation of x-ray and it images the electron density in the object under inspection. An experienced operator can identify different items by their density and shape distribution. X-ray systems are very effective in telling metal from organic material, but lack the ability to distinguish drugs or plastic explosives from ordinary goods.

When low energy x-rays are used as the source, a second detector may be used to record the scattered x-ray. This generally helps to map low-Z material near the surface of the inspected object and is used to detect sheet explosives hidden in the parcel wall or other contraband beneath the wall of a cargo container.

To reduce the cost, a radioactive gamma-ray source (^{137}Cs or ^{60}Co) is sometimes used to replace the X-ray machine.

1.1.2 Elemental Bulk Analysis

The methods discussed in the previous section represent the current generation of contraband detection technology. In general, they do not directly use the primary signature of the drugs or explosives themselves. Another way of detecting such contraband is elemental bulk analysis, that is, to analyze the elemental composition of bulk material—not the density of the bulk or the composition of any trace contamination that may escape from the bulk material.

Drugs, such as cocaine and heroin, have a high carbon to oxygen ratio, high carbon and hydrogen content (and high chlorine content in some forms), low oxygen content and little nitrogen. Explosives have high nitrogen and oxygen content, and low carbon to oxygen ratio [2 & 3].

The elemental characteristics of explosives and drugs have been studied in great detail in research projects sponsored by the FAA [3], and long-time effort has been given to developing techniques that exploit the elemental signature of drugs and explosives. The most promising of these are nuclear techniques.

1.2 Nuclear Methods for Contraband Detection

Nuclear techniques have essential capabilities required for effective drug and explosive detection systems. These are non-intrusiveness, high penetrability, specificity and sensitivity. A nuclear drugs/explosives detection system has four functional parts [4]: (1) source of penetrating radiation; (2) the object under inspection; (3) detector suitable for the resulting radiation; (4) data collecting and analysis device. The two most important issues in developing such a system are practical viability and effectiveness.

1.2.1 Neutron Activation Methods

Neutron activation methods use neutrons as the probing radiation. Neutrons interact with atomic nuclei within the inspected object and the resulting radiation, usually gamma rays, is detected or imaged. Different elements emit gamma rays of different energy, if any.

Thermal Neutron Analysis

Thermal Neutron Analysis (TNA) is the only nuclear based explosive detection system that has been reported operational [5]. A ^{252}Cf isotopic source is used and its neutrons are thermalized. ^{14}N, which is rich in explosives, captures thermal neutrons and the induced 10.8 MeV gamma ray is recorded using NaI(Tl) detectors. The cross section

is low (11.24 mb) and therefore this method has very low sensitivity. In addition, this method has very limited imaging ability and a decision is often made based on the total amount of nitrogen detected. In other words, TNA only measures nitrogen in the inspected object, and very often it only measures the total amount of nitrogen in the luggage. The TNA system is not too difficult to construct, but has very limited success.

Fast Neutron Analysis

Fast Neutron Analysis (FNA) is technically a better approach [6]. A D-T neutron source (14 MeV) is usually used and gamma rays from neutron inelastic scattering on carbon, nitrogen and oxygen are recorded using NaI(Tl) or BGO detectors. In principle, the combined information of C, N, O contents improves the performance in identifying materials.

Unlike the thermal capture gamma ray of nitrogen, which has the highest energy (10.8 MeV) from neutron capture and therefore is free of background, inelastic gamma rays of C, N, O have energies ranging from 2MeV to above 6 MeV. Due to the intrinsic poor energy resolution of NaI(Tl) or BGO detectors, the measured pulse height spectra are usually fitted to recover the amount of carbon, nitrogen and oxygen.

FNA usually uses a microsecond pulsed neutron source, and thermal neutron analysis is done during the intervals between neutron pulses, with no additional cost. TNA offers hydrogen and chlorine information (Drugs are often in hydrochloride form).

FNA or FNA/TNA [7] has very low sensitivity and limited imaging ability. Information about the total amount of hydrogen, carbon and oxygen over a large volume does not help much because they are the major components of most organic goods. Since the gamma ray production cross section is low and only a very small fraction of gamma rays is detected, FNA/TNA has low sensitivity.

Coded Aperture Fast Neutron Analysis

Coded Aperture Fast Neutron Analysis (CAFNA) is an improved imaging method based on FNA/TNA [8 & 9]. A compact sealed D-T neutron tube is used and gamma rays

from inelastic scattering are again detected. A 2-D array of NaI(Tl) or BGO detectors is used and a coded aperture plan is placed between the gamma ray source (inspected object) and the detector array.

The coded aperture (or coding mask) is usually a plate with areas of equal size, some transparent and some opaque to gamma rays, distributed on a regular grid in a pre-determined pattern. A point source casts a projection of the coding mask onto the detector array, and an extensive source casts overlapped projections onto the detector. From knowledge of the aperture and of the detected projection pattern, the original distribution of the source can be reconstructed. In CAFNA, there is no need to collimate the source neutrons. The object is irradiated with a broad fan beam and elastic scattering before the neutron induces a gamma ray improves the uniformity of neutron flux, with no side effects.

CAFNA is an imaging method and the localized information of elemental content can be used to identify different goods. The Coded Aperture Imaging method has been very successful in astronomy and medical imaging. For a large volume gamma ray source (the inspected object, e.g., a cargo container), the reconstruction becomes increasing difficult. Another challenge is to build an appropriate gamma ray detector. The detector is required to have large area, high efficiency, good spatial resolution and good energy resolution for gamma rays of energy 2-6 MeV.

Pulsed Fast Neutron Activation

In Pulsed Fast Neutron Activation (PFNA) [10], nanosecond pulsed neutrons of energy less than 8 MeV (mono-energetic) are generated by the D-D reaction, and collimated to irradiate a line (to be exact, a narrow cone) of the object under inspection. During the time the neutron burst passes through the object, inelastic scattering induced gamma rays are recorded. The gamma ray energy carries elemental information. The time interval between the generation of the neutron burst and the gamma ray arrival is the neutron flight time before being scattered and localizes a voxel along its path. The whole object is scanned and therefore PFNA is a direct 3-D elemental imaging method.

PFNA needs a large particle accelerator (electrostatic accelerator or cyclotron) for the nanosecond pulsing, and its detector/spectrometer works in counting mode requiring very fast electronics. Due to the high speed of neutrons and the relatively slow response of NaI(Tl) detectors, the smallest achievable voxel size is about 5 cm, regardless of the object size.

Associated Particle Imaging

Associated Particle Imaging (API) is a clever idea [11]. No nanosecond pulse or scanning of collimated neutrons is needed. A compact D-T neutron source is used, and inelastic gamma rays from various elements are detected as in PFNA. The alpha particle, associated with the source neutron (The two particles fly in opposite directions), is detected (with a position sensitive detector) to indicate the neutron direction and time of emission. API is also a direct 3-D imaging method.

In a D-T neutron source, the deuteron energy is low (about 100 keV) and space charge effects cause difficulty in beam focusing, which is a key issue for positioning the alpha particle. In addition, the API system works in coincidence counting mode and needs a long imaging time. The practicality of API is limited by physics principles.

1.2.2 Neutron Transmission/Scattering Methods

Neutron transmission/scatter methods are based on the interaction of probing neutrons with nuclei in the inspected object and the transmitted/scattered source neutrons are detected. Different elements have different energy dependence of neutron cross section. To obtain elemental information, neutron energy spectrum is measured or different energy source neutrons are used.

Neutron Resonance Attenuation/Elastic Scattering

Neutron Resonance Attenuation (NRA) [12] requires a nanosecond pulsed white neutron source, usually from the D-Be reaction. The source neutrons travel through the object under inspection, and the energy spectrum of transmitted neutrons is analyzed.

Carbon, nitrogen and oxygen have unique resonance structures in total neutron cross section, and they change the resulting neutron spectrum. Therefore, the projected (along the neutron path) content of these three elements can be inferred by fitting the recorded neutron spectrum with their cross section curves. Scanning the object leads to a 2-D image.

Fast neutron detection is exclusively based on proton recoil and fast neutron detectors have poor energy resolution. NRA has very poor signal to noise ratio (S/N).

There is an alternative to NRA, Neutron Elastic Scattering (NES) [13]. Scattered neutrons are analyzed for elemental information in NES.

Pulsed Fast Neutron Transmission Spectroscopy

Pulsed Fast Neutron Transmission Spectroscopy (PFNTS) [14] has a similar physics principle as NRA: A nanosecond, white spectrum neutron source is used. PFNTS analyzes the transmitted neutrons with the time of flight technique and fits the recorded neutron spectrum for elemental content.

In general, more counts are required for transmission imaging methods than for emission imaging methods (In which the object serves as a gamma ray source). The recording of individual transmitted neutrons is a big problem. PFNTS has as high a system requirement as PFNA and has as poor a S/N as NRA.

Neutron Resonance Radiography

Neutron Resonance Radiography (NRR) [15] exploits the resonance features of the neutron cross section and uses off-the-shelf equipment to achieve elemental imaging with spatial resolution tens of times better than other nuclear methods. NRR is discussed in section 1.3.

1.2.3 Gamma Ray Methods

These methods are based on gamma ray interactions with nuclei. The traditional radiography with an isotopic gamma ray source does not involve interactions with atomic nuclei and is not discussed here.

Gamma Resonance Absorption

Gamma Resonance Absorption (GRA) is based on the resonance absorption of mono-energetic gamma ray by nitrogen [16]. A 9.17 MeV gamma ray is produced with proton bombardment on ^{13}C and collimated to a fan beam. A line of detectors records the transmitted gamma ray to form the absorption (negative) image. A 3-D image is also achievable with tomographic reconstruction.

GRA requires a large particle accelerator and a very high proton current. Only a nitrogen image is obtained with GRA.

Photo Nuclear Activation

Photon Nuclear Activation (PNA) [17] employs a high current electron accelerator to produce bremstrahlung radiation (X-ray). Nitrogen under irradiation is activated and a 0.511 MeV gamma ray is emitted as a consequence of positron annihilation. The 0.511 MeV radiation is then imaged to represent the nitrogen distribution.

PNA requires extremely high dose rates and the 0.511 MeV gamma ray (imaging source) suffers severe self-attenuation. It also is a very inefficient use of photons.

In general, the nuclear methods discussed above detect one or more elements that are essential for explosive and drug detection. They have crude spatial resolution, if any. Most of them require the detector to record individual neutron or gamma ray particles.

The most successful radiation imaging methods are X-ray radiography and tomography (for other applications). They employ a simple fixed radiation source and the

detector works in an integrating mode. This may suggest us on how to develop a nuclear-based elemental imaging method.

1.3 Fast Neutron Resonance Radiography

Fast Neutron Resonance Radiography (NRR) is a nuclear technique for determining a 2-D elemental content distribution. It has the major advantages of nuclear techniques, providing elemental information for explosive and drug detection and the ability to penetrate thick objects. NRR is based on fast neutron radiography. An accelerator is used to produce source neutrons (2-6 MeV) and a hydrogen-rich scintillator (typically plastic) is used to detect the transmitted neutrons. Light emitted from the scintillator is recorded using a CCD camera to form a radiographic image. For each image, the energy spectrum of the source neutrons is chosen to cover resonance features of one or more elements of interest.

Principle

Total neutron cross section below 10 MeV is given in figure 1.1. When a neutron beam travels through the object under investigation, the attenuation coefficient is related to the total neutron cross-section over the energy spectrum of the source neutrons (2-6 MeV neutrons are proposed for NRR). The basic idea of fast neutron resonance radiography is shown in figure 1.2. With a mono-energetic neutron source, we can map one element at a time. We look for an energy region with a resonance peak/valley for one element while the cross sections of other elements are flat over the same energy range. For example, we might choose the sharp resonance peak at 2.077 MeV for carbon. A radiographic image is taken on-resonance, and another taken off-resonance. The difference of the two images gives a 2-D map of the corresponding element.

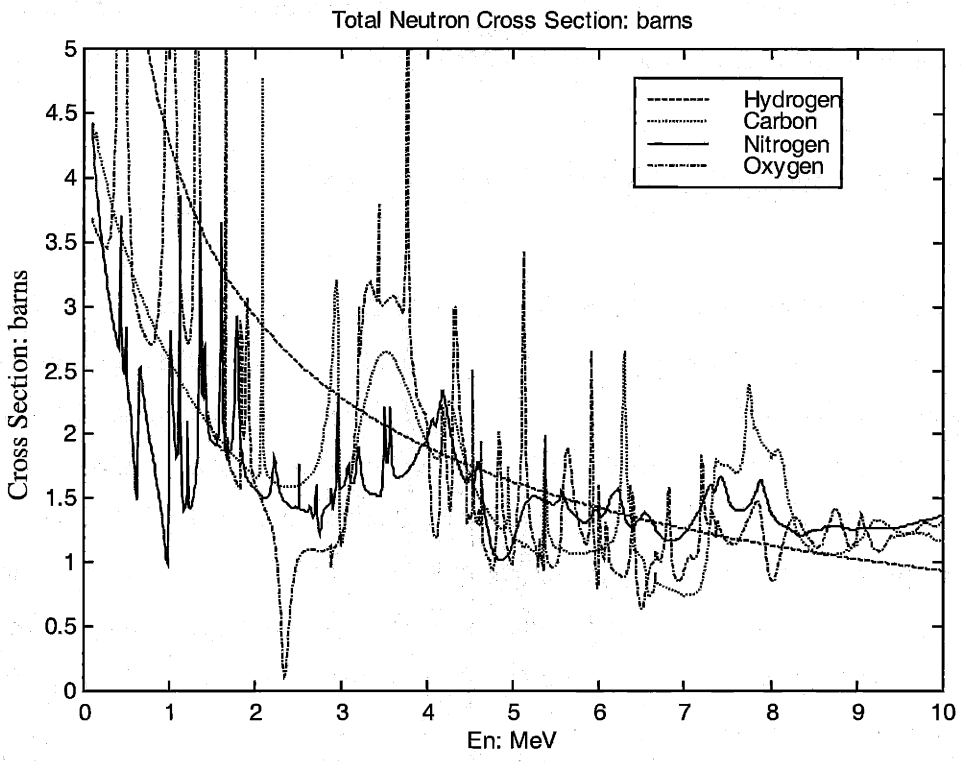

Figure 1.1 Total neutron cross section

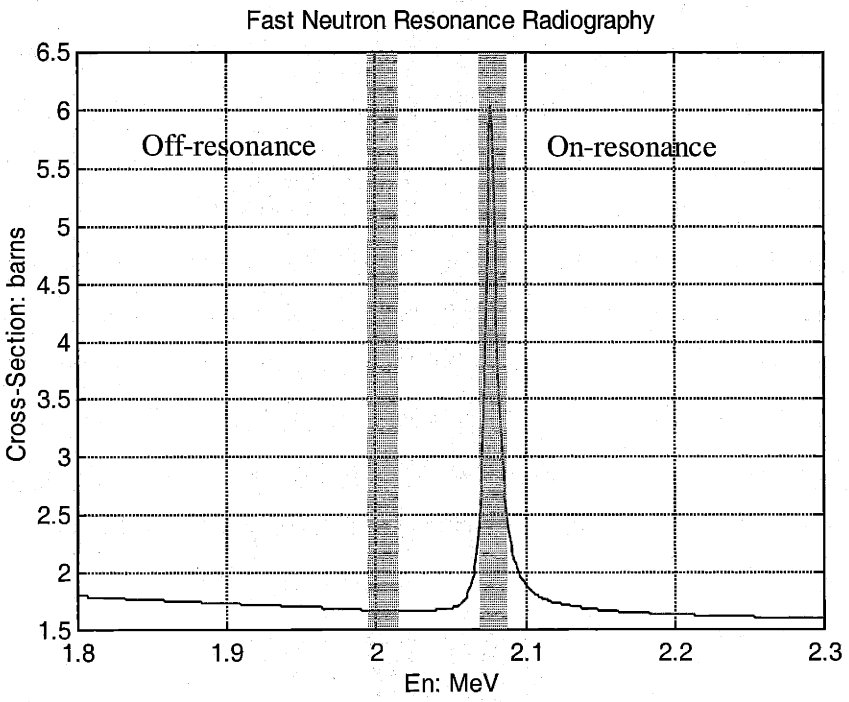

Figure 1.2 Resonance radiography with a single peak

Fast neutron resonance radiography with single peaks has low sensitivity and faces some practical difficulties. This will be discussed in more detail in later text. What we have proposed is to use neutrons of wide energy spectrum and to exploit the broad resonance features of elements of interest.

A radiographic image is a 2-D map of projected attenuation. It can also be thought of as a 2-D map of the sum of the contents of all existing elements, weighted by their attenuation coefficients. For each pixel in the image, there exists a linear equation stating that the total attenuation equals the weighted sum of projected elemental contents. When we take another radiographic image with a different energy spectrum, the resulting linear equations have different attenuation coefficients (weighting factors or attenuation coefficients) and total attenuation, but has the same projected contents, as the object is the same. In principle, when there are more equations than the number of existing elements, the set of linear equations can be solved as a definite Least-Squares solution for the projected elemental contents. NRR with overlapping broad peaks is covered in Chapters 3 and 4 in detail.

Unlike x-ray attenuation, fast neutron attenuation coefficients vary only moderately from energy to energy and from element to element. The difference is typically within a factor of 2 to 3 and is neither too small nor too large. As a result, the linear equation set is a "good" problem. Elements other than hydrogen, carbon, nitrogen, and oxygen are modeled as one component to reduce the number of equations required. We will use H, C, N, O, and "other" to represent these five components. This is generally appropriate for luggage scanning. Using a broad-spectrum neutron source exploits the characteristically broad resonance features of elements. This improves resonance contrast (compared to choosing narrow peaks). In addition, differences among the images (seven or more) are added up, which is very important for low content elements such as nitrogen.

Neutron Source

Using the angular dependence of the DD neutron energy spectrum allows us to use a fixed energy accelerator such as an RFQ and a thick target to generate fast neutrons.

RFQ ion accelerators are compact, high beam current devices usually designed to accelerate a specific ion to a fixed energy [18]. The deuteron is the ion to be accelerated in this application and the target can be either high-pressure deuterium gas or a solid (deuterated) target.

Due to the DD reaction kinematics, neutron energy is angular dependent. Therefore, different energy neutrons can be achieved by rotating the aligned object-detector assembly around the neutron source. This is different from tomography in which the detector and source are aligned and the object rotates around a fixed axis. Suppose E_d = 2.3 MeV and ΔE_d = 0.8 MeV (thick target). The energy range changes from 4.70-5.55 MeV at 0^o to 2.27-2.33 MeV at 115^o. At each nominal angle, the neutron energy spectrum varies over the image, so different attenuation coefficients must be used for different parts in the images. This will be covered in more detail in the following chapters.

1.4 Contributions of the thesis

1.4.1 Contributions

The major contributions of the thesis are summarized as follows:

The primary contribution is the invention of neutron resonance radiography as an elemental imaging method. Elemental bulk analysis seems to be the most promising method for drugs and explosives detection and nuclear methods are the most promising for elemental bulk analysis. NRR employs a compact RFQ accelerator and off-the-shelf detection equipment to acquire 2-D maps of hydrogen, carbon, nitrogen, oxygen and the sum of other elements. The spatial resolution could be below 1 cm, which is much better than other nuclear methods (several centimeters). The linear algorithm and the use of broad resonance peaks eliminate the need for a mono-energetic (adjustable) neutron source. Instead, the angular dependence of neutron energy is used to obtain different energy neutrons. An RFQ accelerator is a compact device, designed to accelerate a

specific particle (deuteron in our application) to a fixed energy. It runs at high current and is very reliable. The requirement of a large particle accelerator is often a fatal weakness of other nuclear techniques for drugs and explosives detection.

Another important contribution is the thorough study of image formation in fast neutron radiography. Fast neutron radiography has not been widely used and the experience from thermal neutron radiography is not directly usable. Factors affecting image formation are analyzed for different applications. The neutron detector is the most important part and its impact on image quality is studied. The imaging geometry, optical system and CCD camera are also studied and optimized. An improved non-linear filtering method is used in image processing and it removes sparkles resulting from CCD defects or cosmic ray interactions.

The study involved in the thesis work made use of analysis, calculation, simulation, and experiments.

1.4.2 Outline

The thesis is organized into five chapters.

Chapter 1 is an introduction and chapter 5 is a summary.

Chapter 2 addresses radiography with fast neutrons.

Chapter 3 discusses the principles of neutron resonance radiography.

Chapter 4 discusses practical aspects of security applications.

Chapter 2

Radiography with Fast Neutrons

Radiography is perhaps the oldest application of radiation technology. The object under inspection is placed between a radiation source (X-ray or neutron) and a recording device (a film or position sensitive detector). The attenuated radiation is recorded and gives the 2-D image of the object. When X-rays are used, the image is the projected electron density distribution. When thermal neutrons are used, the image is often the projected hydrogen (or other low-Z element) density.

Fast neutron radiography is not commonly used due to the relative difficulty in generating, detecting and shielding fast neutrons. Below are recent developments that may improve its utility.

U.S. scientists are building a fast neutron radiography facility to detect tiny defects (~1 mm^3) or cracks in very thick (~200 g/cm^2) high-Z material, which is heavily shielded by low-Z material such as lithium deuteride. In addition, the object has a multi-layer structure. X-rays are not capable of penetrating the high-Z material and thermal neutrons will be mostly attenuated by the low-Z material. Fast neutrons with energy above 12 MeV have the same cross section for almost all elements and is the only practical choice. Views at different angle are needed to reconstruct a 3-D image.

A research group at University of Witwatersrand/De Beers, South Africa is developing a fast neutron resonance radiography facility to look for small pieces (~3mm) of carbon material inside kimberlite rock [19]. This must be done at a moving conveyor belt, and there might be only one piece of carbon in large quantities of rock. The broad neutron-carbon resonance peak at 7-8 MeV neutron energy is employed as the carbon

signature. Carbon can be localized (if any) from the difference between two radiographic images, one taken on-resonance and the other take off-resonance. Different energy fast neutrons are obtained by changing accelerator energy.

Our research on drugs/explosives detection is also based on fast neutron radiography. Imaging formation is thus an important topic to be discussed. The additional requirement for resonance radiography is again a neutron source of variable energy.

2.1 Principle and Configuration

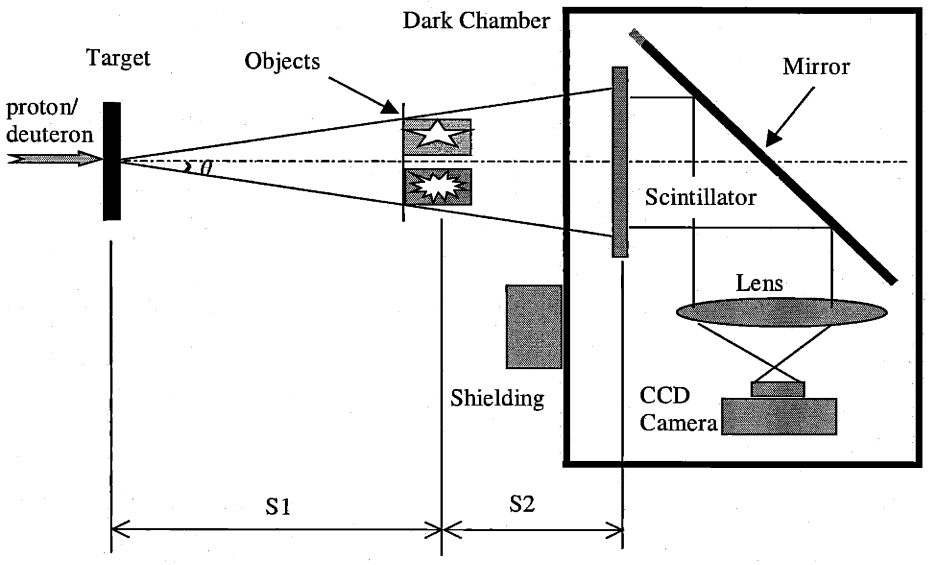

Figure 2.1 Fast neutron radiography hardware

A typical fast neutron radiography setup is illustrated in figure 2.1. The neutron source is usually accelerator based. A proton or deuteron beam is accelerated to the desired energy and bombards the target material to produce fast neutrons by a nuclear reaction. The object can be a passenger bag, flow of kimberlite rock, or a very thick device as mentioned on last page. Scintillation screens are typically used for fast neutron radiography, and a mirror, a lens and a CCD camera [20] are employed to record the image. The mirror is necessary to avoid direct neutron irradiation of the CCD camera, and the lens focuses light onto the CCD chip and helps to collect more light. The light

from neutron detection is extremely weak, so the scintillator, mirror, lens and CCD are light-sealed in a dark chamber. Additional shielding is required to protect the CCD chip against the direct irradiation from the neutron source.

The equation governing fast neutron radiography is from the exponential attenuation law.

$$N = N_0 \cdot e^{-\mu \cdot x} \tag{2.1}$$

Where N is the attenuated neutron number in a small area of the detector, N_0 is the corresponding source neutron number without attenuation, μ is the effective attenuation coefficient (unit: cm^2) and x is the effective total projected atomic content (unit: $\#/cm^2$).

Source neutrons often have an energy distribution. The attenuation coefficient is related to, but not equal to, the neutron cross section or average neutron cross section. This will be discussed in the next chapter.

The imaging contrast is the relative difference in detected neutron number corresponding to different parts of the object, or to images at different neutron energies. In other words, imaging contrast is caused by the product of μ and x, not just one of them.

$$C = 1 - e^{-\Delta(\mu \cdot x)} = 1 - e^{-[(\mu \cdot x)_1 - (\mu \cdot x)_2]} \tag{2.2}$$

It can be easily proved that the relative error of $\Delta(\mu x)/(\mu x)$ is minimized when $\mu x = 1$. That is, radiography is optimal for objects with a thickness of $x = 1/\mu$.

In fast neutron radiography, neutrons are mostly scattered rather than absorbed. If the scattered neutrons arrive at the detector and are recorded, the imaging contrast decreases. Gamma rays are produced by neutron interactions or sometimes as a by-product of the neutron source. Recording these gamma rays also leads to decreased contrast.

2.2 Fast Neutron Production

The most common way of producing fast neutrons for radiography is through nuclear reactions, which requires a particle accelerator and a target. A p-^{7}Li source and a DD source are used in our study. A sealed DT neutron tube is usually used to generate neutrons of about 14 MeV energy, which almost does not change with angle and is too high for radiography.

2.2.1 Particle Accelerators

In fast neutron radiography, protons or deuterons are usually accelerated up to 10 MeV. This can be achieved with an electrostatic accelerator or a linear accelerator with oscillating electric fields [21].

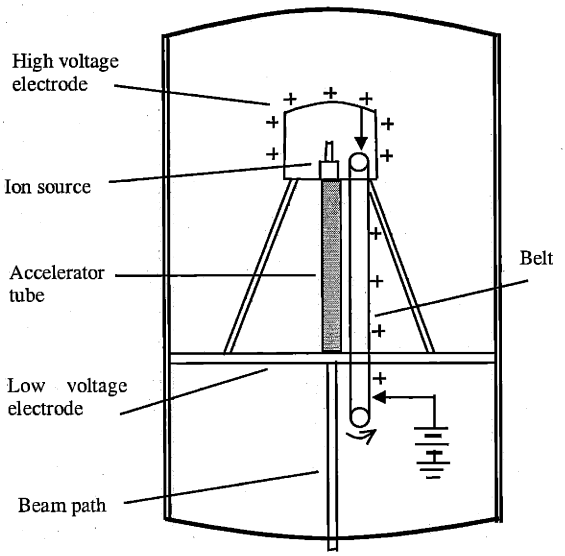

Figure 2.2 Schematic of a Van de Graaff accelerator

Electrostatic Accelerator

The simplest type of elementary particle accelerator is a source of ions and a pair of electrodes, activated by a potential drop. Modern electrostatic accelerators are built as variations on this theme. Figure 2.2 shows the sketch of a Van de Graaff electrostatic accelerator. A belt of insulating material runs between ground and a high voltage generator (~10,000 Volts). Corona discharge provides charge to the belt, which induces electrostatic charges on the high voltage electrode (1-10 MV). Another corona discharge is employed to neutralize the belt. Protons or deuterons are accelerated with the electric field in the accelerating tube. The high voltage is divided and applied to several cascading stages. The tank is often filled with high pressure gases providing insulation and material for corona discharges. A magnetic field is usually employed to focus the ion beam.

An improvement is the tandem accelerator, where negative ions are accelerated from ground to the high voltage electrode, then are stripped of electrons by a thin foil. The resulting positive ions are accelerated back to ground potential. In principle the energy gain can be doubled for protons or deuterons with respect to a simple acceleration.

By changing the terminal voltage, the energy of accelerated particles can be easily controlled. Electrostatic accelerators are therefore widely used in scientific research.

RFQ Accelerator

RFQ (Radio Frequency Quadrupole) accelerators belong to the type of accelerators that use oscillating electric fields to accelerate particles [18 & 21]. RFQ accelerators use four parallel electrodes around the beam axis as shown in figure 2.3. It is a resonant structure with adjacent electrodes having opposite charges. From the end, they look like an electric quadrupole. This arrangement of electric fields focuses the beam in one plane and defocuses the beam in the other plane. Since the electric field oscillates, a net focusing can be obtained. The electrodes are scalloped with a curve somewhat like a sinusoid, with the curves of adjacent electrodes differing by 180^{o} in phase. As a result, a component of longitudinal field will be produced to accelerate the particles.

The major advantage of the RFQ accelerator is that it uses radio frequency electromagnetic fields to simultaneously focus, bunch and accelerate the ion beam. Therefore, it has a strong ability to focus and bunch an ion beam at low energy and to capture almost the entire direct current beam extracted from the ion source at low voltage. An RFQ accelerator is used for preliminary acceleration in higher energy accelerators, or it is used by itself as a high current machine.

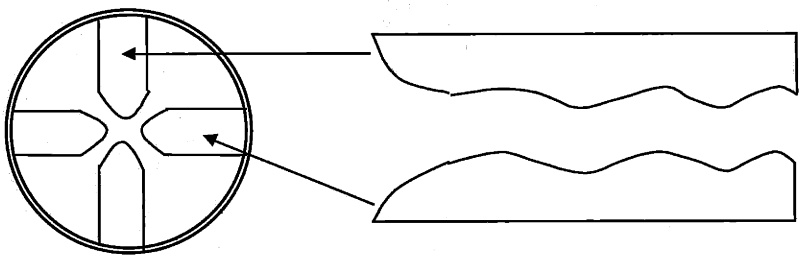

Figure 2.3 A cross section of an RFQ structure

2.2.2 Nuclear Reactions

Nuclear reactions frequently used to produce fast neutrons are ^{7}Li (p, n) ^{7}Be reaction, ^{2}H (d, n) ^{3}He reaction, ^{3}H (d, n) ^{4}He reaction and ^{9}Be (d, n) ^{10}B reaction. The DT reaction and d-^{9}Be reaction are not suitable for resonance radiography and only the first two are employed in our study.

^{7}Li (p, n) ^{7}Be Reaction

The p-^{7}Li reaction is endothermic. The resulting ^{7}Be nucleus can be in ground state or in an excited state, emitting a 428 keV gamma ray when de-exciting. The threshold proton energy is 1.88 MeV for the ground state reaction and 2.37 MeV for the

excited state reaction. The cross section of the second reaction is much lower than for the first reaction when the proton energy is below 5 MeV (Figure 2.4), so the first group of neutrons can be thought of as mono-energetic contaminated by lower energy neutrons.

$$^{7}Li + p = ^{7}Be + n - 1.646\ MeV \tag{2.3}$$

$$^{7}Li + p = ^{7}Be^{*} + n - 2.076\ MeV \tag{2.4}$$

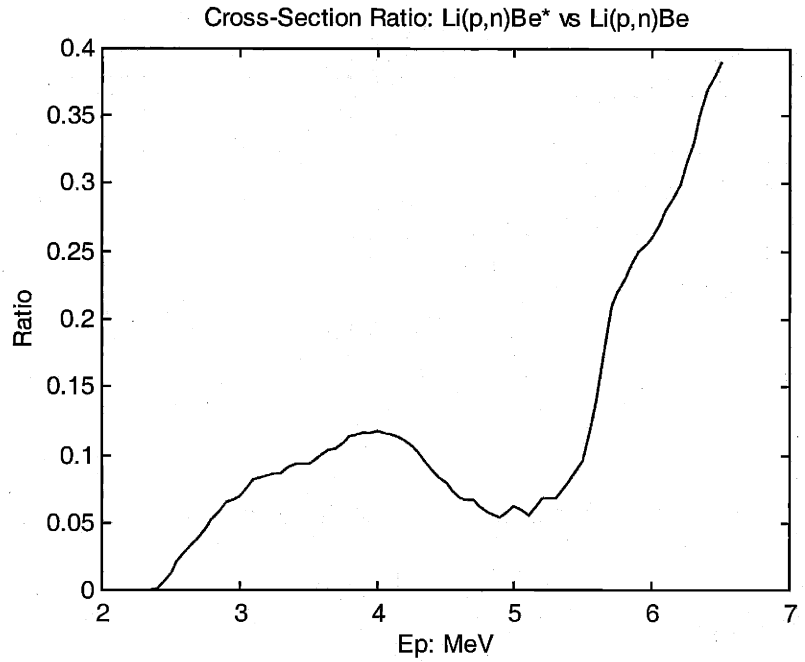

Figure 2.4 Ratio of two neutron groups

In the forward direction, neutron energy falls off gradually. This feature enables this reaction to be used as a mono-energetic neutron source when thin lithium or LiF targets are used. Figure 2.5 shows the neutron energy change with angle, for a 4.0 MeV incident proton and a 50keV thick target. When the object for imaging is within a cone of 10^{o}, the whole exposure area is under irradiation with neutrons of the same energy. This fact is extremely important for resonance radiography with single resonance peaks because the resonances are narrow. The neutron production cross section also falls off very slowly with angle, which gives a flat neutron flux across the image.

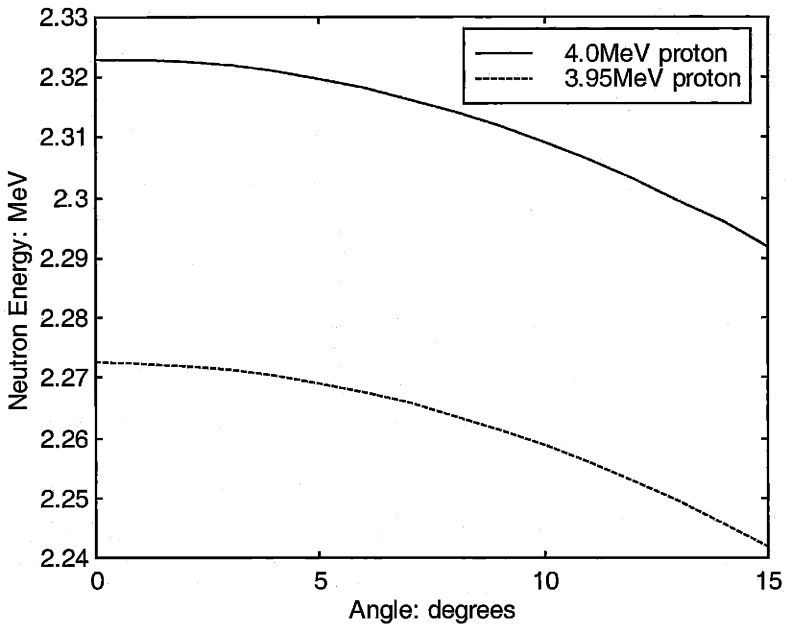

Figure 2.5 Energy fall off of p-Li7 neutron source

The p-Li7 fast neutron source usually has a high gamma ray yield. This causes a background in images and reduces the contrast. One source is the 428 keV gamma ray from the second reaction. It is not significant when proton energy is lower than 5 MeV. The major source of gamma ray yield is proton inelastic scattering.

When a thick lithium target is used, protons are scattered on lithium, producing gamma rays. The major line at relatively low proton energy is the 478 keV gamma ray. When a thin target is used for mono-energetic neutrons, protons are mostly scattered on the backing material, also producing gamma rays. Gamma-ray yield in a thick target or in backing material increases rapidly with proton energy. The reaction ^{7}Li (p, n) ^{7}Be has a negative Q-value. In the application of fast neutron radiography, the proton energy needs to be 4 MeV or higher. Tantalum has been used as the backing in our experiment.

The lithium target has a very low melting point (180^{o}C) and it is chemically active and can be easily oxidized. In general lithium is difficult to handle and not good for high current applications. Chad Lee [] proposed using a liquid lithium target to generate low energy neutrons for BNCT.

^{2}H (d, n) ^{3}He Reaction

The DD neutron source is the most commonly used for neutron production in the 3 MeV to 12 MeV energy range. The reaction is characterized by a single neutron group. It's exothermic and has a Q-value of +3.27 MeV. The minimum neutron energy in the forward direction is 2.6 MeV.

$$^2H + d = ^3He + n + 3.27\,MeV \tag{2.5}$$

Neutrons from ^{2}H (d, n) ^{3}He reaction are kinetically collimated in the forward direction and have a rapid energy and angular cross section fall off. Figure 2.6 shows the energy fall off for 2.0 MeV and 1.95 MeV deuterons. The object must be restricted within a 5° cone to be effectively irradiated by mono-energetic neutrons across the image. The DD neutron source is not a good candidate for mono-energetic neutron generation.

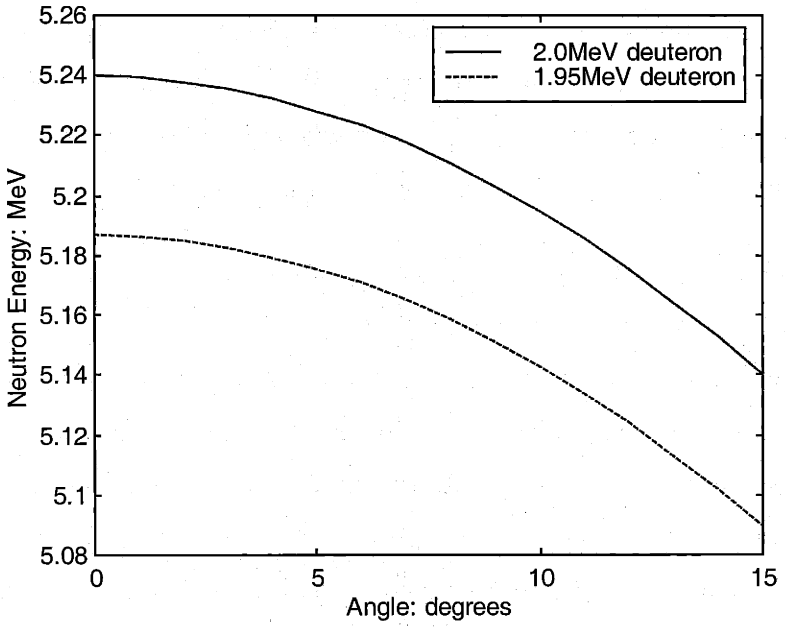

Figure 2.6 Energy fall off of DD neutron source

A major advantage of the DD neutron source is that a D_2 gas target could be used. The gas is radioactively, chemically and physically stable. The gas could be circulated to

remove heat delivered by the ion beam. A plasma window enables the use of high pressure gas (6-7 atmosphere) and a very high beam current for intense neutron beams.

The DD neutron source has a low gamma ray yield. Neutron energy (2.0 MeV deuteron) changes from 5.25 MeV at 0^{o} to 2.11 MeV at 125^{o}. We obtain different energy neutrons at different angles for resonance radiography, using a compact RFQ to accelerate deuterons.

2.3 Fast Neutron Detection

Like gamma rays, neutrons are uncharged particle and have no Coulomb interaction. Neutrons are detected through nuclear collision, which result in energetic charged particles such as protons or alpha particles. Every type of neutron detector involves the combination of a target material designed to carry out this conversion, with a conventional radiation detection mechanism to record the energy of the resulting charged particle. For radiography, the detector must have reasonable spatial resolution.

The only effective way to detect fast neutrons is proton recoil in hydrogen rich material. When a neutron is scattered by a hydrogen nucleus, it transfers all or part (half on average) of its kinetic energy to the recoil proton. The target hydrogen nucleus can be considered at rest so the sum of the kinetic energy of the reaction products, the recoil proton and the scattered neutron, is equal to the incident neutron energy. The scattered neutron could further interact with the detector material after traveling a distance and the process degrades the image quality. The recoil proton energy is angle-dependent. For non-relativistic neutrons, the recoil proton energy is:

$$E_p = \frac{1}{2} \cdot (1 - \cos\ \theta) \cdot E_n \tag{2.6}$$

where θ is the neutron scattering angle in the center of mass coordinate system. The recoil proton has a simple rectangular energy distribution for neutron energies below 10 MeV. In a quantum mechanics view, only the s wave has a significant contribution

and therefore the scattering process is isotropic and the scattering cross section $\sigma(\theta)$ is a constant.

In fast neutron radiography, neutron detectors work in an integrating mode. That is, individual neutrons are not counted. As illustrated in figure 2.1, the CCD camera accumulates light emitted from the scintillator and forms an image. The concerns are efficiency, spatial resolution, light output and sensitivity to gamma rays.

2.3.1 Scintillation Detectors

Scintillation detectors are used in fast neutron imaging. Fast neutrons are scattered by hydrogen nuclei and the energetic recoil proton ionizes and excites the molecule or crystal of the scintillator, causing the emission of light. The amount of light is an indicator of the recoil proton energy, not that of the incident neutron energy. Thus in fast neutron spectroscopy, the recorded pulse height spectrum for mono-energetic neutrons is a rectangle distribution, altered by statistics and noise.

The detector could be made of an organic scintillator such as plastic, or an inorganic scintillator dispersed in a hydrogen rich base. In our study, plastic scintillators NE102, BC400, BC430 and inorganic scintillator ZnS(Ag) (silver activated ZnS dispersed in Polypropylene) are involved. Table 2.1 gives their properties.

Table 2.1 Properties of scintillators (*: % of Anthracene)

Scintillator	H/C ratio	Density g/cm^3	Refractive index	Light output*	Emission maximum (nm)	Light attenuation length (cm)
NE102	1.104	1.032	1.581	65	423	250
BC400	1.103	1.032	1.581	65	423	250
BC430	1.108	1.032	1.58	45	580	Semitransparent
Polypropylene	2	0.897	1.51			N/A
ZnS(Ag)		4.09	2.36	290	450	Opaque

Plastic Scintillators

If an organic scintillation material is dissolved in a solvent, which can be subsequently polymerized, the equivalent of a solid solution can be produced. Plastics are easily shaped and fabricated and are an extremely useful form of organic scintillator.

As the recoil proton deposits its energy in a plastic, individual molecules of the scintillation material are excited. The transitions in its energy level structure could lead to the emission of visible light. (Prompt emission is called fluorescence, slower emission at longer wavelength is called phosphorescence, and delayed fluorescence has the same spectrum as prompt fluorescence but much longer emission time.)

In plastic scintillators, the excitation energy undergoes substantial transfer from molecule to molecule before de-excitation occurs. This energy transfer process is important, because the recoil proton energy is primarily absorbed by the solvent and only the solute molecules are light emitters. The molecules have usually achieved thermal equilibrium before emitting a photon and the emission process is isotropic.

The emission and absorption spectra of a plastic scintillator are mainly determined by the energy level structure of the solute molecule. Not all transitions lead to the emission of light. Indeed, a solute molecule is often excited to a high level, losing energy through several decays to the ground state. Photon(s) could be emitted. The absorption spectrum usually has short wavelength than the emission spectrum for a transparent emitter.

The light output of plastic scintillators is relatively low and its linearity with recoil proton energy is poor. The light output is given by an empirical formula:

$$dL = k \cdot E_p^{1/2} \cdot dE_p \tag{2.7}$$

where k is a constant for a given material. At higher recoil proton energy, more light (dL) is emitted for the same amount of energy loss (dEp). Similarly, for a given material, the constant (k) for fast electrons is larger than for protons. This difference is

due to a smaller *dE/dx* and therefore less ionization screening effect for fast electrons than for protons. When an incident neutron delivers its full energy to a recoil proton in one collision, the event produces highest light emission. If the neutron loses all its energy in the detector through several collisions, much less total light will be emitted.

NE102 and BC400 plastic scintillators are almost identical and they emit short wave length photons. They are transparent with a 250 cm absorption length for their own light. BC430 is a yellow emitter that better fits the spectral response of the CCD camera we used. Plastic scintillators have a low refractive index that helps light to exit.

ZnS(Ag) Scintillator

A fast neutron detector can also be made by dispersing inorganic scintillation material into a hydrogenic substance. ZnS(Ag) in polypropylene is an example. In inorganic crystals, electrons are either in valence band (lower band) or activated to the conduction band (higher band). Although these two bands are separated by a gap called the forbidden band, absorption of energy can elevate the electron from its normal position in the valence band across the gap into the conduction band.

In pure crystals, the transition from the conduction band to the valence band leads to very inefficient photon emission. In addition, the gap is usually big so that the resulting photon is in the ultraviolet region. Impurities are often added creating trapping sites in the lattice, in which the normal energy band structure is modified. The impurities are called activators and serve as light emitters. The absorption spectrum of the host crystal should be at lower wavelengths than the emission spectrum of the activators so the light can escape.

ZnS has the highest light output among scintillation materials and is therefore widely used. Equation (2.7) is also true for ZnS. We investigated a scintillator with ZnS(Ag) dispersed in polypropylene. The light output has been optimized by carefully choosing particle size and fraction. ZnS is available only in a polycrystalline powder and is therefore opaque to its own light. This fact limits the thickness of a ZnS-polypropylene screen to about 2 mm.

2.3.2 Efficiency

In fast neutron radiography, the detector works in an integrating mode, in which the CCD records the total amount of light emitted from small areas of scintillation screen. As we previously mentioned, light output from individual neutron events is different. The incident neutron may transfer its full energy to the recoil proton in a head-on collision or part of its energy when scattering at an angle. It could also scatter on a carbon nucleus, losing some energy, or it could experience multiple scattering within the scintillator. Furthermore, equation (2.7) tells us that different amounts of light are expected for the same amount of total energy if the scattering histories are different. (Losing the energy in one collision vs. in two or more collisions.)

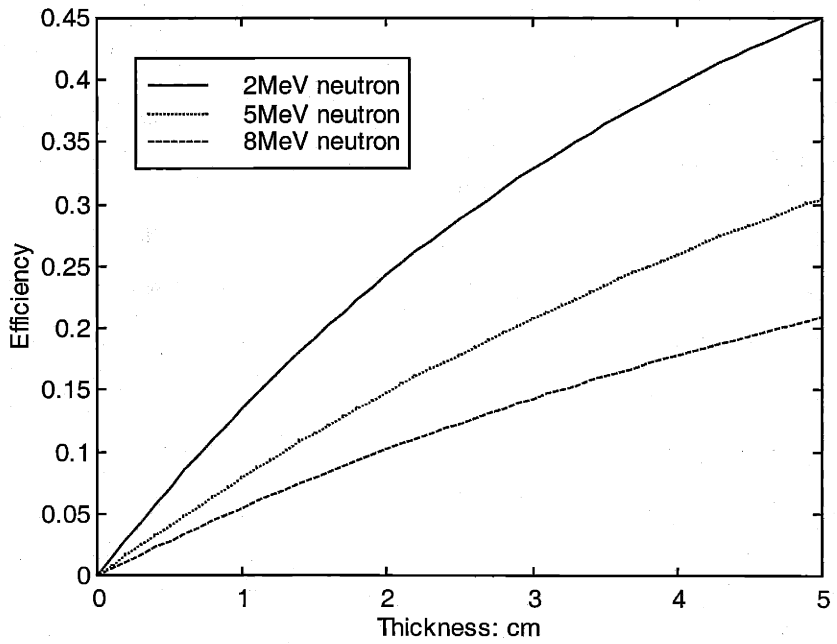

Figure 2.7 Detection efficiency of BC400

With large numbers of neutron events, there exists an average light output per detected neutron. We can define the neutrons that scatter on hydrogen as being detected, neglecting multiple scattering and regarding the scintillator as a composition of only hydrogen and carbon. This defined detection efficiency is:

$$\varepsilon = \frac{N_H \sigma_H}{N_H \sigma_H + N_C \sigma_C} \cdot [1 - e^{-d(N_H \sigma_H + N_C \sigma_C)}] \tag{2.8}$$

The calculated detection efficiency of BC400 is given in figure 2.7. Plastic scintillators have similar H/C ratio and density and have about the same efficiency. The efficiency of 2.4 mm thick ZnS—polypropylene is 0.05, 0.027 and 0.019 for neutron energies of 2 MeV, 5 MeV and 8 MeV respectively.

2.3.3 Spatial Resolution

Spatial resolution is a measure of how fine a detail can be detected, in terms of distance in space. Experimentally, it is often measured with a point spread function (PSF) or line spread function (LSF). The sharp edge of a object shows as a gradual transition in the image, and the FWHM (full width at half maximum) of the derived LSF is the spatial resolution. Overall spatial resolution (detector intrinsic resolution, source size and geometry effect) is affected by the following factors:

- Finite range of recoil protons.
- Multiple neutron scattering in detector.
- Spread of scintillation light.
- Detector thickness.
- Focus depth of lens.
- Finite dimension of neutron source.
- Angular dispersion of the source.
- Image magnification.
- Object thickness

The first four items are intrinsic to the detector. The recoil proton may have enough energy to travel a distance before it stops (Figure 2.8), emitting light along its path. This generally leads to a transverse spreading. Recalling equation (2.7), little light is emitted near the end of the path. In addition, recoil protons have relatively lower energy if they are not forward directed (relative to θ=0° in figure 2.1). The spread caused by finite proton range should be much smaller than the range itself. Multiple neutron

scattering leads to multiple recoil protons. When the detector material is not transparent to its own light, light spreads and is scattered instead of traveling in a straight line. This process decreases spatial resolution and enhances the light output at normal direction of detector surface. That is, scintillation light is no longer isotropic. It favors the normal direction instead. This is true for ZnS and BC430 detectors.

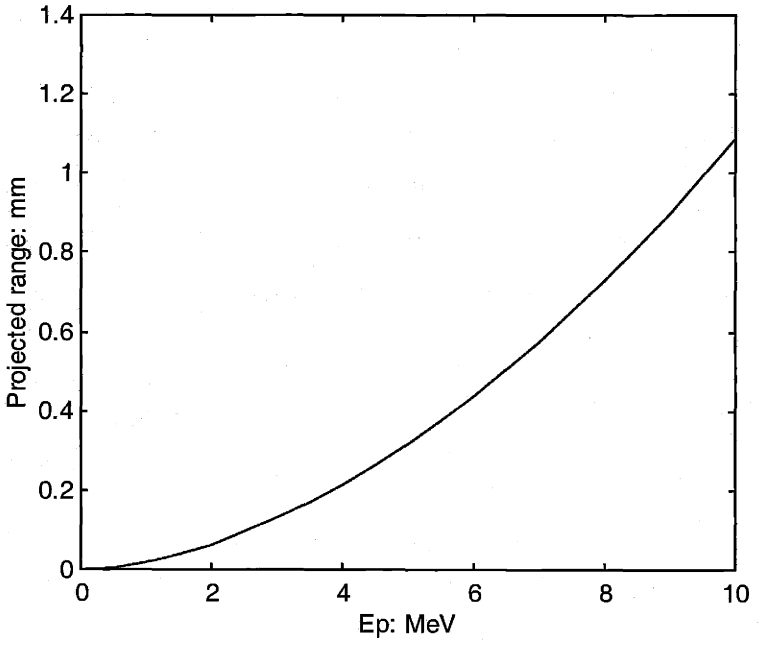

Figure 2.8 Projected proton range in plastic scintillators

Intrinsic spatial resolution has been measured with 12 MeV neutrons. The object is four meters away from the source and the detector is right behind the object (Image magnification is unity). Spatial resolution is measured at the center of the detector, which lies on the axis of the neutron source (accelerator axis). Table 2.2 lists the measurement results (courtesy of James Hall of LLNL).

Table 2.2 Intrinsic spatial resolution of scintillators (En=12 MeV)

Detector	2.4 mm ZnS	2 cm BC430	2 cm BC400	4 cm BC400
FWHM	1.36 mm	2.15 mm	0.79 mm	1.10 mm

2.3.4 Light Output

The amount of photons that exit the scintillator surface near the normal direction is affected by scintillation efficiency (or light yield, the photons produced in the material per unit incident energy), angular distribution of light and surface reflectivity.

Recoil protons lose their kinetic energy in the scintillator, and the energy will eventually lead to excitation of molecules or crystals. Some of the excitations will be transferred to a molecule of the scintillation agent (or activation center in the case of a crystal). The subsequent deexcitation could lead to the emission of a photon. Scintillation efficiency is the ratio of the total energy of scintillation photons to the energy of recoil proton. It can be as high as 20% for ZnS or as low as several percent for plastics.

The scintillation process itself is isotropic. However, this does not guarantee an isotropic distribution at the surface. The outer surface of a scintillator is usually flat and specula, but the suspended particles inside diffuse the scintillation light. Some photons are absorbed in the process and others are redirected. The result is that more light exits the detector in the normal direction. Extracted light from ZnS and BC430 has been greatly enhanced. Shi [22] has quoted ZnS as a Lambert surface (A 4-fold increase in the normal direction). There is no way other than experiment to prove this point because Lambert's law itself is empirical. Light output of BC430 is not enhanced as much as ZnS, and we can be sure that BC430's surface is not a Lambert source. BC400 is transparent to it own light and is free of this effect.

The refractive index of scintillators does not match that of air. Reflection at the interface leads to loss of light. Plastic scintillators have a refractive index of 1.5-1.6, and light loss increase at angles greater than 20^{o}. (Total reflection angle is about 40^{o}.)

Figure 2.9 gives the measured light output of several scintillators with 12 MeV neutrons (courtesy of James Hall of LLNL). It is the recorded light on the central line of images. CCD quantum efficiency is virtually the same for all these light spectra, and the plot represents the light output at the surface. The vertical axis is normalized to light per incident neutron, so the neutron detection efficiency has not been compensated. BC430

has lower scintillation efficiency but higher light output than BC400, due to the diffuse enhancement. The 2.4 mm ZnS has very low neutron detection efficiency (~1.5%), and its high light output is due to the high scintillation efficiency and diffuse enhancement.

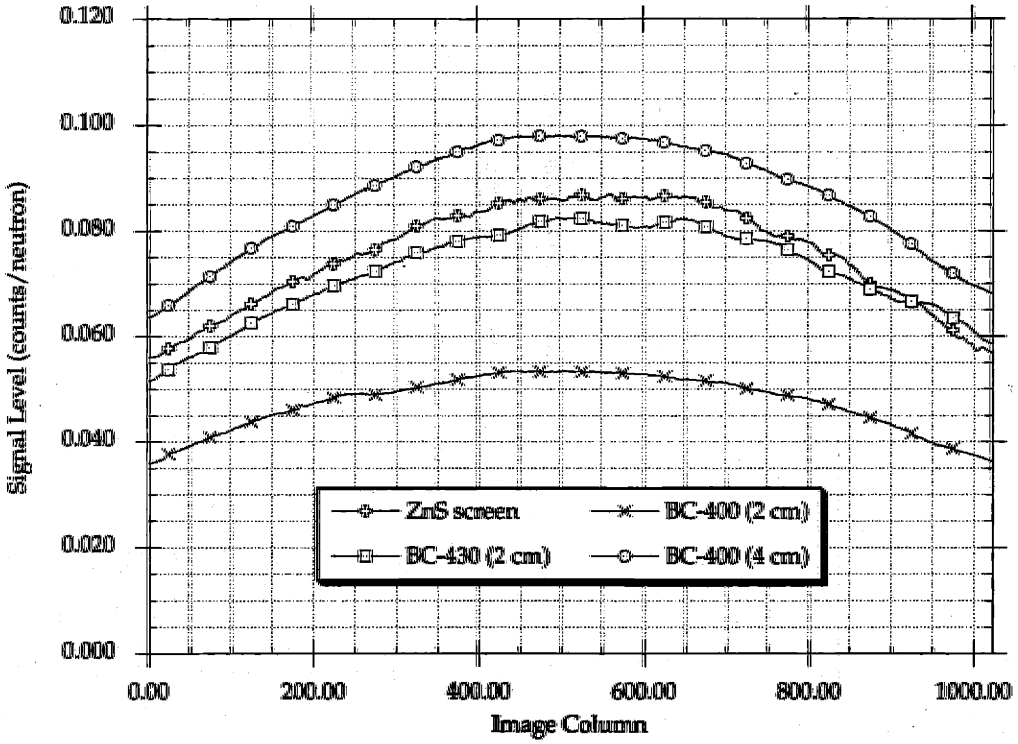

Figure 2.9 Comparison of light output (En=12 MeV)

2.3.5 Sensitivity to gamma rays

The p-^{7}Li neutron source is intrinsically contaminated with gamma rays. In addition, neutron interactions in the inspected object, detector and structure or shielding material may produce gamma rays. Scintillation detectors are sensitive to gamma rays. Fast electrons (from Compton scattering of gamma rays) have higher scintillation efficiency than does the recoil proton. As a result, gamma ray events lead to much more light output than fast neutron events, for incident particles of the same energy. Figure 2.10 shows the measured pulse height spectra with a ϕ4"x3" NE102 detector.

Fast electrons have relatively long range (~5 mm in plastic at 1 MeV). Therefore reducing the scintillator thickness to 1-2 mm can significantly improve the situation. Fast

electrons deliver only a fraction of their energy to the scintillator and exit the detector, greatly reducing the light output per detected gamma ray. Watterson made such a screen with ZnS(Ag) dispersed in polypropylene and it is used in their search for small pieces of carbon from kimberlite rock.

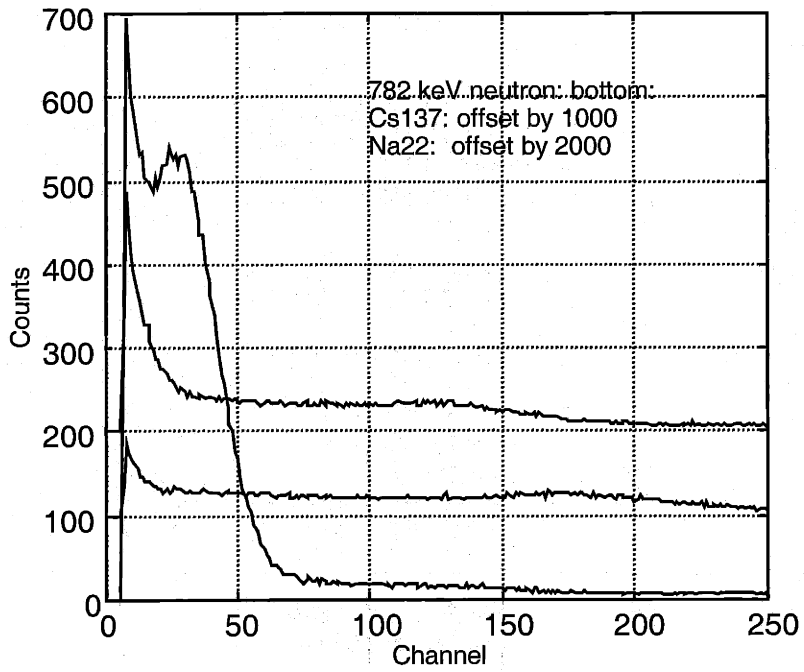

Figure 2.10 Pulse height spectra with large NE102 detector

2.4 Geometry Effects

Source-object distance (s1), object-detector distance (s2), imaging magnification (m=1+s2/s1), source dimensions, viewing angle (θ), and thickness of object and detector are the major geometric factors. (See Figure 2.11.) They greatly affect image quality.

2.4.1 Imaging Magnification

In radiography, an image of the object is cast onto the detector. The ratio of image size to object size is called the imaging magnification. Imaging magnification is determined by source-object distance (s1) and object-detector distance (s2), m=1+s2/s1.

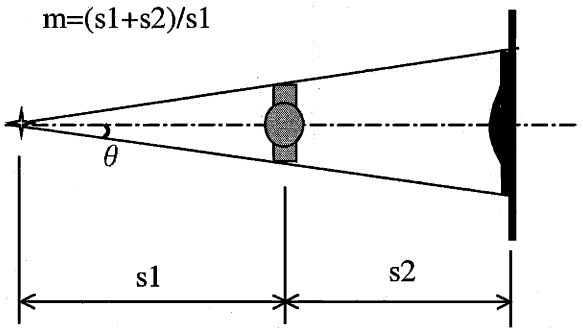

Figure 2.11 Imaging magnification

Object-Detector Distance

Object-detector distance (s2) is chosen based on two concerns: (1) to control the recording of scattered neutrons and (2) to change magnification (m).

In fast neutron radiography, neutrons are attenuated mainly by elastic scattering. Imaging contrast comes from the fact that only a fraction of source neutrons are not scattered and are detected. Since scattered neutrons go in every direction, it is impossible to eliminate the detection of neutrons scattered by the inspected object. Recording scattered neutrons leads to decreased imaging contrast.

Source neutron intensity in the detector plane decreases by $1/(s1+s2)^2$, while scattered neutron intensity decreases by $1/(s2)^2$. When s2 increases, there is a net gain in the ratio for detecting source neutrons as compared with scattered neutrons. An additional advantage of increasing s2 is that the scattered neutrons are more evenly distributed on the detector. In principle, a constant background in the image can be subtracted and only statistical noise of the background is added to the resulting image.

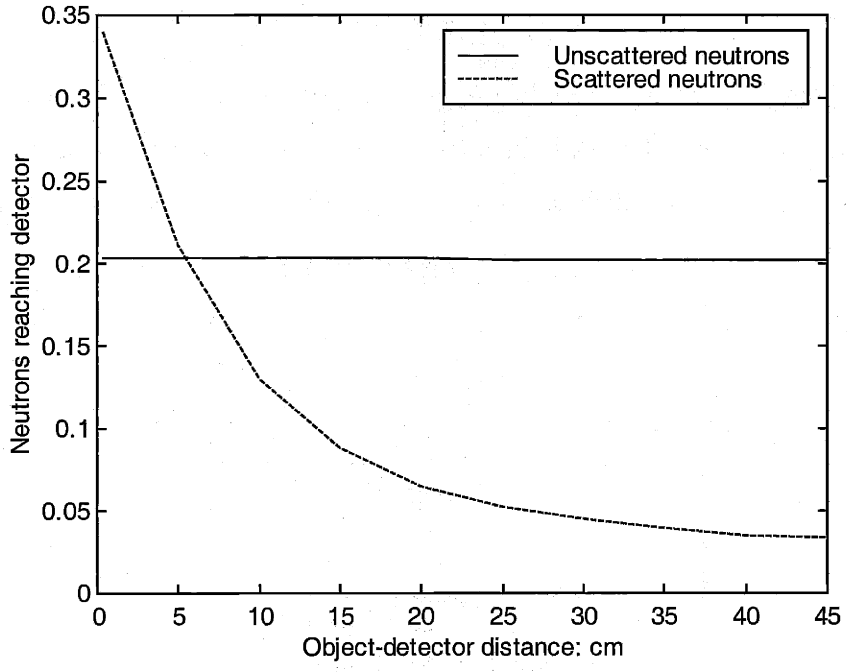

Figure 2.12 Neutron penetration and scattering (2 MeV, 5 cm polyethylene)

Figure 2.12 shows the fraction of transmitted neutrons and scattered neutrons that reach the detector plane as a function of s2 (Source to detector distance is kept constant). The incident neutron energy is 2 MeV and the object is 5 cm thick polyethylene. Between 30 cm and 50 cm seems to be the optimum object-detector distance for reducing the detection of scattered neutrons.

Source-Object Distance

Source-object distance (s1) is also chosen based on two concerns: (1) to control the viewing angle (θ) and (2) to change magnification (m).

An ideal radiation source is a parallel beam of particles. (L/D, the length to diameter ratio of collimators is a traditional measure of parallelism in practice.) In fast neutron radiography, a cone beam of fast neutrons is employed. Since both neutron energy and production cross section fall off with angle, it is desirable to control the viewing angle θ so that the change in neutron energy and intensity across the image is acceptable. Large viewing angles also lead to large imaging distortion and poorer spatial

resolution. (This will be discussed later.) Therefore, once we know what we are imaging (object size) and how broad the beam cone (θ) is allowed to be, we know how far the object should be from the source.

For the example of detecting ~1 mm^3 defects or cracks in thick high-Z material, the object diameter is about 25 cm. Narrow cone beam (θ=3°) should be used for the required image quality. The source-object distance is thus set at 2.5 m. In our application, the viewing angle should be controlled to θ=10-15°.

Magnification

An important concern in choosing s1 and s2 is the image magnification, which controls image size and influences image quality. For small objects, it could be beneficial to cast a bigger image on the detector for convenience.

Large magnification reduces the requirement on a detector's spatial resolution. Since the object is smaller than the image (in the detector plane) by a factor of 1/m, spatial resolution requirements in the detector plane (R_d) are reduced (improved) by 1/m as compared with the object plane (R_o).

$$R_o = R_d \cdot \frac{1}{m} = R_d \cdot \frac{s1}{s1 + s2} \tag{2.9}$$

That is, if the detector has a 2 mm spatial resolution and m=2, the resulting spatial resolution in object plane is 1 mm. In the example of detecting ~1 mm^3 defects or cracks in thick high-Z material, magnification of 2 is used.

Small magnification reduces the requirement for small neutron sources. A real source has finite dimensions. As a result, the image of an object point appears as the pin hole image of the source, instead of as a simple point. (Figure 2.13) This causes blurring and contributes to the overall spatial resolution. The shadow is s2/s1 times (or m-1 times) as big as the source itself. The shadow size represents the resolution in the detector plane (R_d), which is further reduced by 1/m in the object plane (R_o).

$$R_o = R_d \cdot \frac{1}{m} = [R_s \cdot (m-1)] \cdot \frac{1}{m} = R_s \cdot \frac{s2}{s1+s2} \tag{2.10}$$

R_s can be thought of as the FWHM of the source intensity distribution. To reduce the image blurring caused by a non-point source, small magnification is desired. In experiments measuring detector intrinsic resolution, detectors are placed directly behind the object (s2=0).

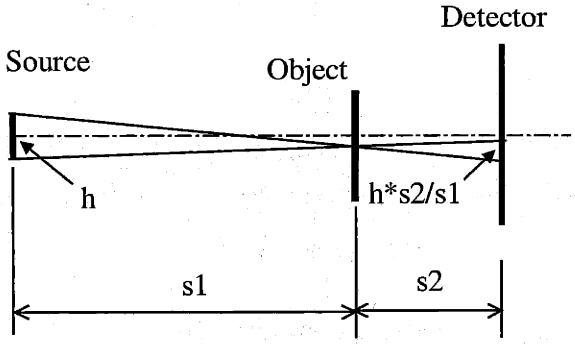

Figure 2.13 Image defining optics

2.4.2 Imaging Distortion and Blurring

Radiography is a 2-D imaging method. That is, a 3-D distribution of a property is projected into a plane. X-rays project electron density along its path onto the detector plane, while neutrons project a weighted atomic density along its path to form a flat image. Ideally, the radiation beam is parallel and the object is projected along the beam direction. In practice, a cone beam is used and different parts of the object are projected in different directions (along the local beam path). This leads to image distortion. Both thick objects and thick detectors cause image distortion when nonparallel beams are used.

As we have discussed previously, finite source size and detector intrinsic spatial resolution cause image blurring and their effect in the object plane may be controlled by the geometric arrangement. Imaging distortion is another source of blurring when thick detectors are employed.

Object Thickness

A physical object is always a 3-D body. Only in the perpendicular direction (usually through the object center) is the projection the way we desire (See figure 2.14). Image distortion in a thick object, by itself, does not cause image blurring. A sharp picture is available on a thin detector. This is similar to looking at a side mirror of a car, where the image is sharp but looks slightly different from the object.

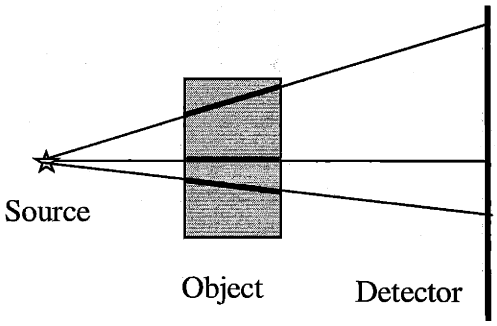

Figure 2.14 Image distortion in thick object

Detector Thickness

In fast neutron radiography, scintillation light is collected with a lens, which has a focal depth comparable to the detector thickness (t) and usually focuses at the middle plane of the detector. The scintillator is a 3-D light source and is projected by the lens onto a flat plane (CCD chip), in the perpendicular direction. At this time, the light source corresponding to an object point is a line at an angle. Therefore this process also leads to image distortion. The difference is that, neutron beam projects the correct object in a wrong way, while the lens projects the wrong light source (scintillation detector) in the correct way.

The distortion in a thick detector leads to image blurring. The contribution to overall spatial resolution is of the order of $t*\tan(\theta)$, where t is the detector thickness and θ the projection angle.

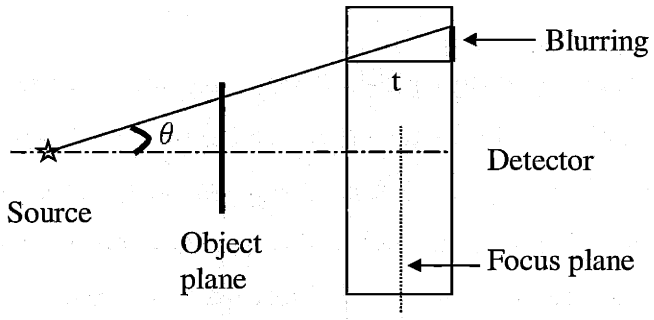

Figure 2.15 Image distortion and blurring in thick detector

2.5 Image Recording

Scintillation light from the neutron detector is generally reflected with a mirror and then collected with a lens onto a CCD chip, which converts individual photons into electrons. After a desired exposure time, the collected electrons in each pixel are converted into a voltage level, forming a digital image.

2.5.1 Optical System

Dark Room

A dark room provides light sealing for optical components including the scintillation detector, mirror, lens and CCD head. Since light from fast neutron detection is extremely low, any light leak adds an overwhelming background (with fluctuation and statistic noise) to our image and therefore must be eliminated. Although the imaging lens has a relatively large field of view (15^{o}-25^{o}), only a small fraction of scintillation light is directly collected. Flat black paint is generally applied to absorb light that does not travel directly to the lens. The front surface (the one facing the object) of scintillator is also painted flat black or coated with a reflective layer.

Ideally the dark room wall is transparent to fast neutrons. The wall between the inspected object and the neutron detector directly attenuates neutron beam. Furthermore, when a neutron interacts with structural material, the scattered neutron or induced gamma ray may reach the scintillator or CCD chip, deteriorating image quality. A hollow structure is desired and the thickness of structural material should be minimized, especially those in neutron beam path.

Mirror

Neutron irradiation damages CCD chips. A flat mirror is employed to reflect the scintillation light through an angle of 90 degrees, as shown in figure 2.1. For similar reason that a dress mirror can be shorter than ourselves, the reflection mirror can be slightly smaller than the scintillation detector itself. Since the mirror is under direct neutron irradiation, its thickness should be minimized. A 2-3 mm pyrex mirror provides adequate strength and is preferred as a base material. The reflectivity of the mirror should match the spectrum of scintillator. Since emission spectra of most scintillators lie in the blue or UV wavelength region, an aluminum coating is a good match.

Lens

The lens is the major component of the optical system. It focuses scintillation light onto the CCD chip. In our lens optical system, the "object" is our neutron detector (scintillation light source) and the "image" plane is where the CCD chip is. The basic relationship is

$$\frac{1}{S_o} + \frac{1}{S_i} = \frac{1}{f} \tag{2.11}$$

S_o is the "object" to lens distance and is measured from the scintillator to the primary principal point of the lens (Principal points are where the optical axis intercepts the lens surfaces). S_i is the "image" to lens distance, measured from the CCD chip to the secondary principal point of lens. f is the focus length of lens.

Minification is the ratio of "object" height to "image" height:

$$m_L = \frac{H_o}{H_i} = \frac{S_o}{S_i} \tag{2.12}$$

$$\text{or,} \qquad S_o = (1 + m_L) \cdot f \tag{2.13}$$

A large area (small f-number) lens is desirable to collect more light from the "object" (scintillator). The f-number (or f-stop) is the ratio of the focal length to aperture diameter of the lens. Unfortunately, using a small f-number lens leads to a smaller minification number m_L, which requires a larger CCD chip. For fast neutron radiography, lenses of f-number around 1 are used.

The fast neutron detector is a 3-D scintillation light source. According to equation (2.11), only one plane in the scintillator is perfectly in focus. A light source in front of or behind the plane is out of focus and casts a circle of confusion in the "image" plane (CCD chip). The diameter of the circle of confusion increases with the deviation from in focus plane [23] (Figure 2.16). If the circle of confusion is small enough, given the magnification in projection, the optical quality throughout the system, the image will appear to be sharp. Focus depth (or field depth) is the allowed deviation from the in focus plane for an acceptable circle of confusion, although there is no clear boundary between fuzzy and clear. The experimentally measured intrinsic spatial resolution (on the detector plane) is 0.79 mm and 1.10 mm for 2 cm and 4 cm thick BC400 scintillators respectively. (Table 2.2). The difference is due to the circle of confusion effect.

2.5.2 CCD-Camera

A charge-coupled device (CCD) is an analog integrated circuit that converts an optical image into an electronic one. Electrons (induced by photons) are accumulated in each pixel during the exposure time and transferred to readout electronics (usually sequentially) thereafter. The number of electrons in each pixel is converted to a digital level, forming the final digital image.

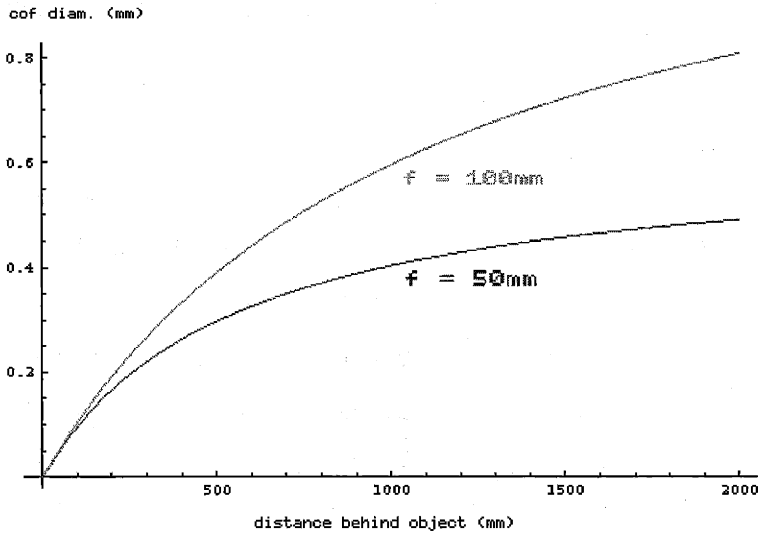

Figure 2.16 Circle of Confusion

A CCD is a one-dimensional (line) or two-dimensional array of standard metal oxide (MOS) or photodiode based capacitors. Each pixel may contain one or more of these elements. When a photon interacts with silicon, an electron-hole pair is generated. The electrons accumulate in a depleted zone (the capacitor), and the hole is re-combined in the silicon substrate. The charge is stored in a potential well when a positive voltage is applied to the central electrode of the particular pixel. The voltage across electrodes can be varied to transfer charge from one segment to the next.

A CCD chip can be made as big as 6 cm x 6 cm, with 4096 x 4096 pixels. Most commonly used is a 1-2 cm CCD, with 512 x 512 or 1024 x 1024 pixels. The CCD camera is not the limiting factor of the overall system spatial resolution. A CCD well capacity is typically around 500,000 electrons (each capacitor unit).

Quantum Efficiency

Quantum efficiency is the ratio of number of induced electrons to the number of incident photons. Light may be reflected by the CCD surface. The photon may also pass through the silicon without being detected. Quantum efficiency is wavelength dependent. Early CCD chips are front illuminated. That is, light enters from the front and exits from

the back surface (if there is no interaction). For UV application, the front surface is coated with a very thin layer of a converter (lumogen) which absorbs UV radiation and re-emits at a wavelength in the visible region.

To eliminate loss of response due to absorption by and reflection from the poly-silicon gates on the front surface of the CCD, special CCD arrays that can detect through the rear surface are used. These CCDs are usually thinned to less than 15 μm and the rear surface is sufficiently coated with anti-reflection material. This back illuminating method achieves great improvement in the overall quantum efficiency, especially in the UV region. Figure 2.17 gives a typical spectrum response.

Electron flux created on the CCD chip is directly proportional to photon flux, and therefore proportional to the detected neutrons per unit area per second. Shi [101] calculated and measured the electron flux at CCD (electron/cm^2-sec) for a ZnS screen, which is assumed as a Lambert light source:

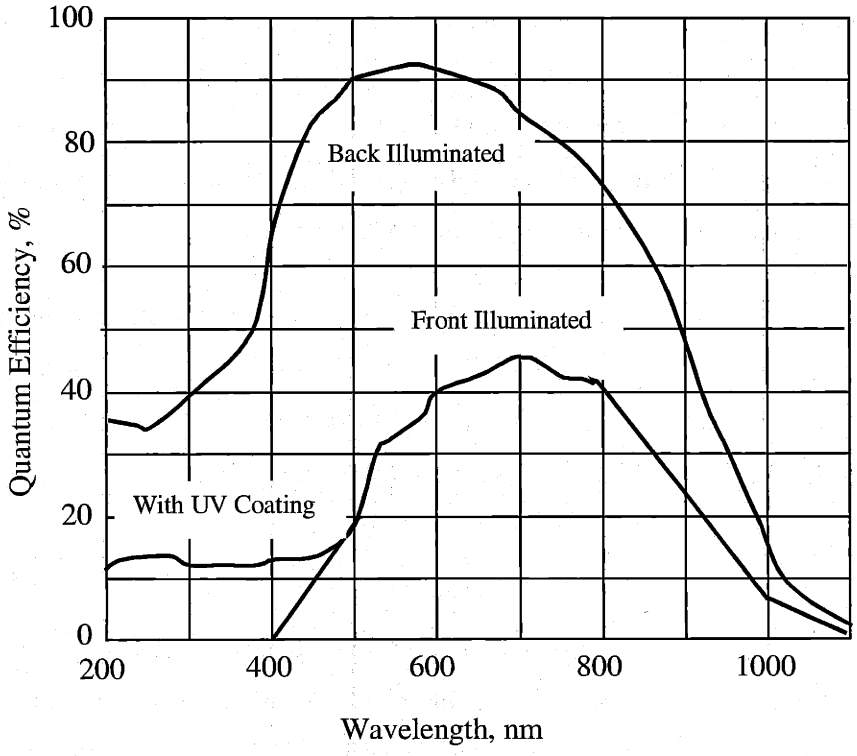

Figure 2.17 CCD quantum efficiency

$$\phi = \frac{\Phi_n \cdot \eta_{CCD} \cdot \eta_0 \cdot \eta_\gamma}{4 \cdot F^2} \cdot \frac{m_L^2}{(1+m_L)^2} \tag{2.14}$$

Φ_n: detected neutrons/cm^2-sec at scintillator

η_{CCD}: quantum efficiency of CCD

η_0: optical efficiency of lens (transmission)

η_γ: average photons/neutron produced in scintillator

F: f-number of lens

m_L: minification of lens system

CCD Noise

There are two noise sources, one is due to dark charge and the other is generated in the readout process.

Dark charge [24] is generated in silicon by the thermal motion of electrons. With sufficient thermal energy, electrons can move to the conduction band and are trapped, producing charge. Dark charge and signal generated charge are readout together, so there is no way to differentiate them. The number of dark charge N strongly depends on temperature and therefore the CCD chip usually operates at low temperature.

$$N \propto e^{\frac{-E_g}{2KT}} \tag{2.15}$$

where E_g is the band gap and K is Boltzman's constant.

Figure 2.18 gives the measured dark charge of the TEA/CCD-1024. Dark charge increases the background level, reducing the usable dynamic range and increasing the overall noise due to fluctuations in the dark charge signal. Although dark charge caused background can be digitally subtracted, the dark charge noise cannot.

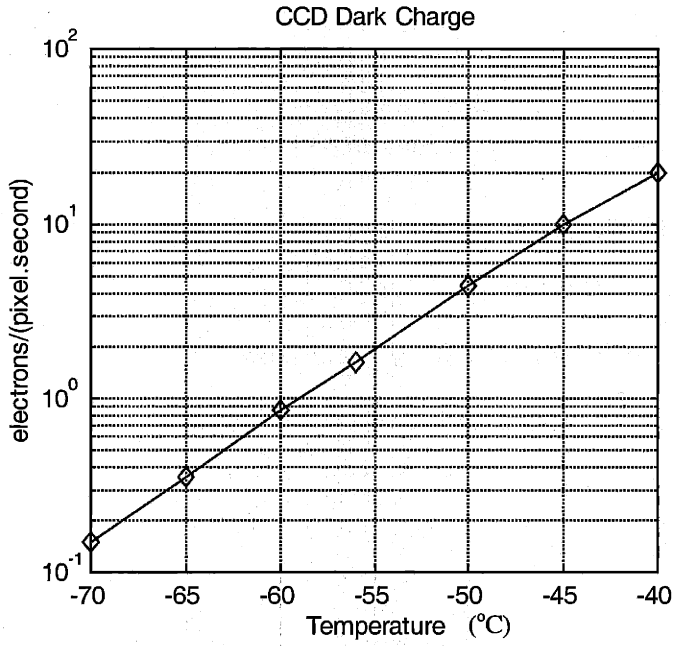

Figure 2.18 Dark charge of a TEA/CCD-1242E CCD camera

Another noise source is readout noise. Accumulated charges are sequentially transferred along the MOS capacitors to a readout stage. This transfer process adds fluctuations to the electron number. Readout noise is also generated in the readout electronics, primarily in the preamplifier. Readout noise increases with readout rate but can be significantly reduced when the temperature is below 60°C. Typical readout noise is 10 electrons/pixel (RMS).

CCD Defects

Not all CCDs are made to the NASA standard. CCD devices are usually manufactured with defects and irradiation leads to additional defects. Dark point defects represent reduced response compared to adjacent pixels. Hot point defects represent higher dark current (or dark charge) compared to the adjacent pixels. Pixel traps are pixels that interfere with the charge transfer process and usually result in either a partial or complete bad column (either dark or white). A cluster defect is a cluster of adjacent pixels which are either dark or white with respect to the neighboring pixels.

2.5.3 Nonlinear Filtering

CCD defects lead to dark or white points, lines or clusters in the digital image. When radiation (neutrons, gamma rays or cosmic rays) hits the CCD chip, there might be an interaction with silicon, creating an energetic charged particle. The resulting charged particle will generate a lot of electron-hole pairs and leads to a white point or points. These sparkles are generally treated with a nonlinear filter.

Median filter is a commonly used nonlinear filter. the pixel value is changed to have the median value of the pixels within its neighborhood (usually 3 x 3 or 5 x 5), i.e. half of the pixels in the neighborhood will have values above the median and half will have values below the median.

The median filter changes the values of most pixels, whether they are sparkles or not. This eliminates the chance of improving S/N with a linear filter thereafter. An improved median filter has been used in our study. Sparkles are detected with a deviation check. That is, the pixel value is replaced with the median only when it deviates from the median within the neighborhood to a certain extent. (For example, one standard deviation of the neighborhood values.) The modified median filter removes sparkles but preserves fine structures in the digital image. Figure 2.19 shows the result of such filtering.

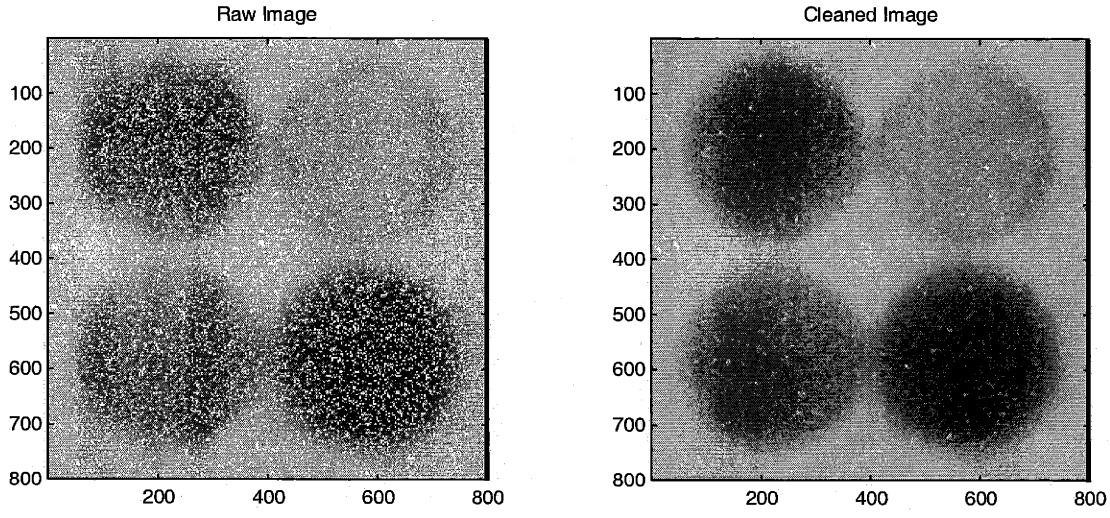

Figure 2.19 Non linear filtering

2.5.4 a-Silicon Flat Panel

An alternative to a CCD is an amorphous silicon flat imaging panel [24 & 25]. Amorphous silicon can be deposited on large surfaces in a uniform layer, it is sensitive to visible light, and it has relatively low manufacturing cost. A large flat panel a-silicon sensor is directly attached to the scintillator for radiography or other imaging applications.

Amorphous silicon has a disordered crystalline structure, which scatters charge carriers (electrons or holes) in such a way that their mean free path is proportional to the scale of the disorder. The localized nature of the order implies that the disorder-affected energy band structure in the small crystals will not extend throughout the solid. The inclusion of hydrogen removes the structural defects and saturates dangling bands (lying between valence bands and conduct band) in the amorphous material. This feature makes hydrogenated amorphous silicon radiation hard. A flux of 10^{14} neutrons/cm^2 (1 MeV) causes acceptable deterioration.

An a-silicon sensor has a Schottky photodiode design, which requires no n-doped region (which exists in a PIN design leading to no signal generation) and therefore has higher quantum efficiency than a CCD. The disadvantage of an a-silicon sensor is its high dark current (therefore dark charge) and the difficulty of achieving uniform response and uniform dark charge.

Prototype a-silicon flat imaging panels are commercially available. Further improvement could enable them to replace CCD cameras in large area imaging.

2.6 Quantum noise in Fast Neutron Detection

As we have indicated, fast neutrons are expensive. There is a strong desire to use as few neutrons as possible and image quality is usually quantum noise limited. The fluctuation in accumulated electron number of each CCD pixel (subtracting dark noise

and readout noise) is a direct measure of quantum noise. When imaging with natural light, the variance can be estimated as the electron number *ne,* and S/N as $(ne)^{1/2}$.

In fast neutron radiography, each detected neutron knocks out a recoil proton (with a rectangular energy distribution), which leads to light output from the scintillator. A fraction of the light will be collected by CCD and will generate electrons. The ratio of signal (detected neutron events) induced electron number (*ne*) to detected neutron number (*nn*) differs with incident neutron energy, detector scintillation efficiency, collection efficiency of the optical system and CCD quantum efficiency.

The detected neutron number obeys Poison's statistics and its variance is:

$$Var\ (n) = Mean\ (nn) \tag{2.16}$$

Without considering other source of noise such as dark charge, variance in accumulated electron number is expressed as:

$$Var\ (e) = Var\ (n) \times (1+\alpha) \times [\frac{Mean\ (ne)}{Mean\ (nn)}]^2 + Mean\ (ne) + Var\ (device\ ) \tag{2.17}$$

where α results from the difference in electron number caused by each detected neutron.

$$(S/N)_e = \frac{Mean(ne)}{\sqrt{Var(e)}} < \frac{Mean(ne)}{\sqrt{Var(n)\cdot(1+\alpha)}\cdot\frac{Mean(ne)}{Mean(nn)}} = \frac{1}{\sqrt{1+\alpha}}\cdot(S/N)_n \tag{2.18}$$

That is, electron S/N is always poorer than neutron S/N, although no other noise source has been included in the analysis.

Simulation

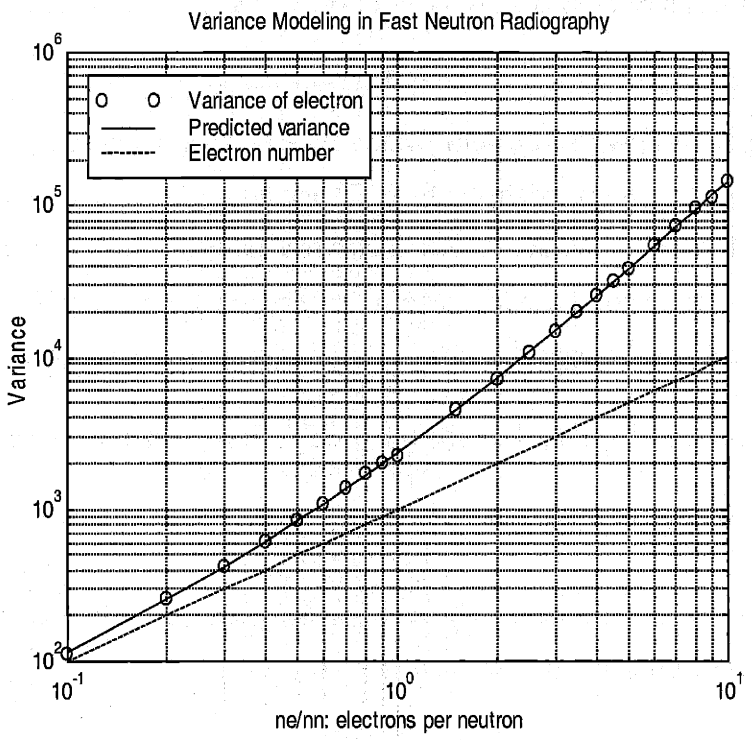

Figure 2.20 Variance of accumulated electrons (α=1/3)

The process from neutron detection to electron generation is studied with Monte Carlo simulation, with the following method:

- 100,000 neutrons reach an area of the neutron scintillator.
- The average detection efficiency is 1%, or ~1000 neutrons are detected.
- Each detected neutron generates 0-10,000 photons, with a rectangular distribution.
- The product of lens efficiency and CCD quantum efficiency is adjusted from $2x10^{-5}$ to $2x10^{-3}$. (For a practical system, optical efficiency is ~0.1%)
- Each photon has a chance to cause one electron in the CCD. This process is independent for individual photons.

Figure 2.20 shows electron variance as a function of *ne/nn*. The simulation matches prediction (solid line) with equation (2.17). The dashed line gives the electron number, which equals the electron variance if the electrons had been generated by independent photons.

Figure 2.21 shows electron S/N as a function of *ne/nn*. At the low end, the curve approaches *1/sqrt(ne)*, which is the expected S/N for an independent photon source. At the high end, it approaches the limit described in equation (2.18). As long as there are ~3-5 electrons for each detected neutron, there is very little benefit from further increasing the optical efficiency or the CCD quantum efficiency or from using a light intensifier.

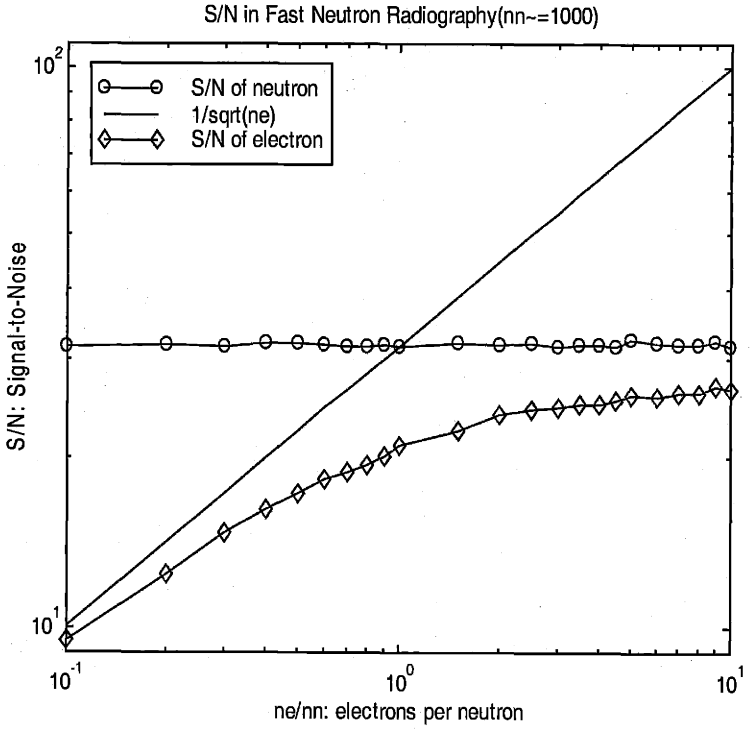

Figure 2.21 S/N of accumulated electrons

Experiment

Figure 2.22 shows experimental data on electron variance. A 1.5 mm thick ZnS-polypropylene scintillator and a 1 cm thick BC430 scintillator were tested in the experiment. The CCD camera was a front illuminated TEA/CCD-1242E model, which has ~5% and ~30% quantum efficiency for the two scintillators respectively.

The data are taken from randomly chosen neighborhoods (thousands of pixels each) in cleaned images (with sparkles removed). For the same counts/pixel (electron

number are digitized into counts), ZnS-polypropylene has much larger variance. BC430's light is from more detected neutron events and therefore has less variance.

Higher neutron detection efficiency improves electron S/N and image quality. This improves the ability of detecting fine structures or calculating elemental mapping from resonance images.

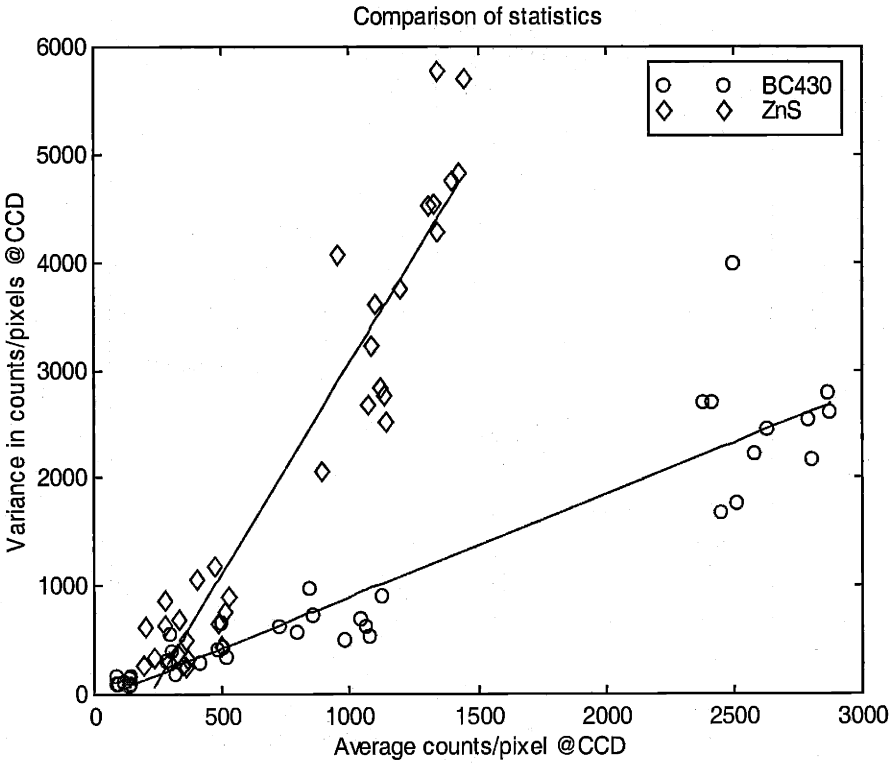

Figure 2.22 Measured variance in images

Comments

A thin ZnS-polypropylene scintillator may emit more light and lead to more accumulated electrons than a thicker plastic scintillator. However, its light is from fewer detected neutron events and therefore carries less information.

As long as a few electrons are generated from each detected neutron, quantum noise is always dominated by the detected neutron number, therefore neutron detection efficiency (not light output) is the dominant factor and a thicker detector should be

chosen with regard to quantum noise. Similarly, a light intensifier in front of the CCD camera will not help. (It does help if the CCD operates at room temperature and dark current is extremely high.)

A 2 cm thick BC400 is adequate for detecting ~1 mm^3 defects or cracks in thick high-Z material, while 4 cm BC400 may be the best choice for security applications of neutron resonance radiography.

Chapter 3
Principles of Fast Neutron Resonance Radiography

Fast neutron attenuation is strongly energy dependent, as shown in the neutron cross section curves (Figure 1.1). A resonance occurs when the incident neutron energy corresponds to an energy level of the compound nucleus. A single resonance peak is formed in the cross section curve in this situation. For fast neutrons, the observed structure often represents an average over many overlapping single resonance peaks.

Some of the resonance peaks are distinct and some peaks overlap. Neutron resonance radiography is an elemental imaging method that exploits the resonance features of neutron attenuation by different elements. When single distinct peaks are employed, most elements can be imaged one by one. When overlapping broad resonance peaks are used, all elements could be imaged by taking a set of radiographs and solving the resulting linear equations. The linear equation set is required to be over determined and is solved with a least squares method. Careful choice of neutron energies and representing elements optimizes neutron resonance radiography.

3.1 Neutron Resonance Radiography with Single Peaks

3.1.1 Principle

A straight forward way of doing neutron resonance radiography is to map one element at a time. At an energy region with a resonance peak or valley for one element while the cross sections of other elements are flat over the same energy range, we:

(1) take a radiographic image at on-resonance energy;
(2) take a radiographic image at off-resonance energy; and
(3) take the pixel-by-pixel difference of the two images.

The 1.5-2.5 MeV region is suitable for this purpose. Figure 3.1 shows the peaks used for three different elements. Unfortunately, hydrogen has no resonance peak.

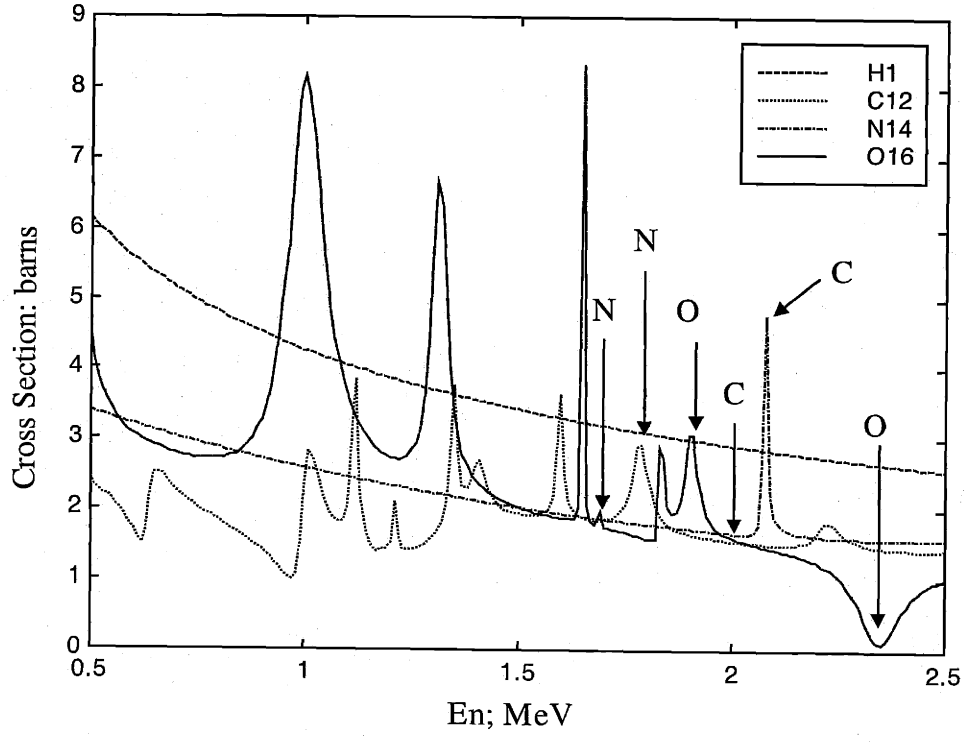

Figure 3.1 Single peaks chosen for resonance radiography

Resonance contrast is $\Delta(\mu x)$ between the two neutron energies chosen for each element. See equations (2.1) and (2.2). The relative error, $\Delta(\mu x)/(\mu x)$, is minimized when $\mu x = 1$. That is, radiography is optimal for objects with a thickness of $x=1/\mu$. At 2 MeV, the optimal thickness is about 5 g/cm^2 for common organic goods, and it decreases to about 4 g/cm^3 at 1.5 MeV. The relatively high cross section of hydrogen has a negative effect on neutron penetration and imaging contrast.

3.1.2 Experiment

Experiments were performed for neutron resonance radiography with single peaks at the University of Massachusetts Lowell Radiation Laboratory. Since we are interested in drugs and explosives detection, organic samples were tested and elemental images of carbon, nitrogen and oxygen were derived from the difference.

Neutron Source

A p-^{7}Li neutron source was used, with a 5-10 μA proton beam from a Van de Graaff accelerator. Neutron yield was about 5x10^7 neutrons/sr/s at 0 degree. Since resonance peaks are mostly 10-30 keV in width, a thin target was required for mono-energetic neutron generation. The target material was a pure lithium layer (~50 keV thick at 2 MeV neutron energy) evaporated onto a tantalum backing. Tantalum has virtually no gamma ray yield except for low energy (~100 keV) photons from Coulomb excitation. Heat delivered by the proton beam was removed with a turbulent falling water film.

Samples and Geometry

Drug simulant, explosive simulant, graphite powder and melamine, in 35 mm photographic film containers are used as testing objects. Figure 3.2 shows the test objects and table 3.1 lists their composition. Source-object distance was ~30 cm and object-detector distance was ~15 cm. The objects are within a 10° cone beam. (s1=~30 cm, s2=~15 cm, $\theta < 10^o$)

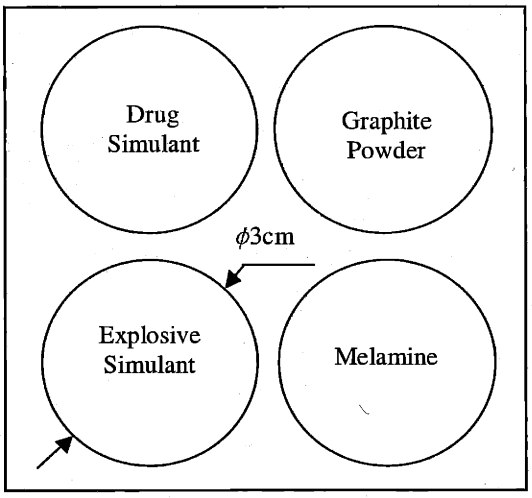

Figure 3.2 Test object

Table 3.1: Object composition

		Drug Simulant	Explosive Simulant	Melamine	Graphite Powder
Mass (grams)	Total	23.90	27.59	37.33	10.56
	H	1.49	1.02	1.78	--
	C	16.32	7.15	10.67	10.56
	N	0.91	7.15	24.89	--
	O	5.18	12.26	--	--
Mass Thickness (g/cm^2)	Total	3.38	3.90	5.28	1.49
	H	0.21	0.14	0.25	--
	C	2.30	1.01	1.51	1.49
	N	0.13	1.01	3.52	--
	O	0.73	1.73	--	--
$Atoms/cm^2$	H	$12.7x10^{22}$	$8.7x10^{22}$	$15.1x10^{22}$	--
	C	$11.6x10^{22}$	$5.2x10^{22}$	$7.6x10^{22}$	$7.5x10^{22}$
	N	$0.6x10^{22}$	$4.4x10^{22}$	$15.1x10^{22}$	--
	O	$2.8x10^{22}$	$6.5x10^{22}$	--	--
Equivalent Formula		$C_{21}H_{23}N_1O_5$	$C_7H_{12}N_6O_9$	$C_3N_6H_6$	C

Image Formation and Processing

Two scintillators were used as neutron imaging screens, a piece of 1 cm thick BC430 plastic and a piece of 1.5 mm thick ZnS-polypropylene. BC430 emits yellow light and ZnS-polypropylene has its maximum emission at 450 nm. The ZnS detector emits 10 times more light for each detected neutron and is less sensitive to gamma rays. However, its neutron detection efficiency is unacceptably low.

We used a Perkin-Elmer lens (f=100 mm, F=0.95) and a TEA/CCD-1242E CCD camera to record the images. The camera is front illuminated and has 1152 x 1242 22.5 x 22.5 μm pixels. The camera has a built-in thermoelectric cooler (Peltier effect) and was cooled to –72°C with chilled water applied to its heat rejecter. The amplification of readout electronics was adjusted to 0.8 counts/electron. The baseline (in images) of the readout electronics was ~250 counts and the dark charge was 0.1 electrons/pixel/s at -72°C, or ~150 counts/pixel in 30 minutes.

Radiographs were processed in the following procedure:

- A non-linear filter (deviation check) was used to remove sparkles.
- Readout baseline and contribution of dark charge are subtracted.
- Combining 4 by 4 pixels into 1 pixel.
- Pixel by pixel ratio of off-resonance image vs. on-resonance image was taken.

Results

Figure 2.19 shows a radiographic image of the test objects at the carbon resonance energy with a BC430 detector. Measured overall spatial resolution is 2 mm and 3 mm, respectively, when ZnS and BC430 are used. Figure 3.3 and Figure 3.4 show the major results of single-peak resonance radiography. The BC430 detector gives acceptable elemental images for carbon and oxygen, but is poor for nitrogen. ZnS-polypropylene gives a reasonably good image for carbon, but it is poor for oxygen and nitrogen.

Quantative analysis shows that only the carbon images properly describe the objects for both detectors. BC430 gives a poor O/C map and ZnS gives an irrelavant one.

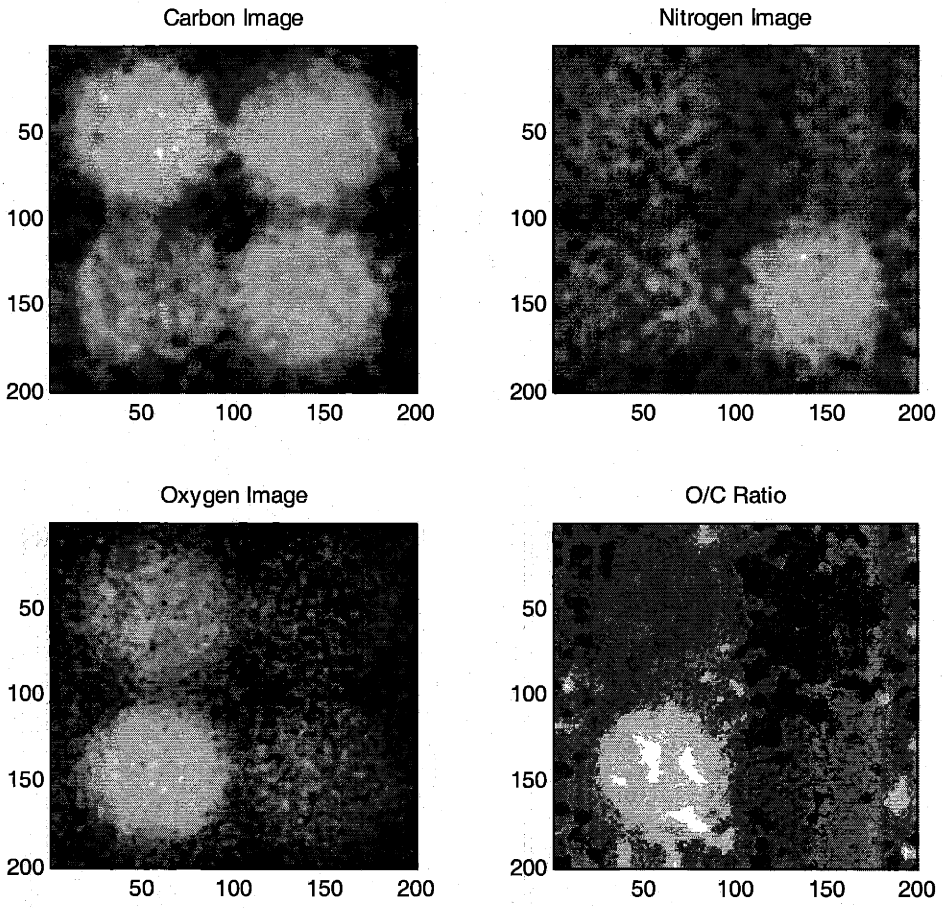

Figure 3.3 Single-peak resonance radiography (BC430)

3.1.3 Discussion

Neutron resonance radiography with single peaks maps one element with two images, one on resonance and the other off resonance. The procedure is simple and easy to understand. BC430 gives a better result because more neutrons are detected and radiographs have better S/N.

Single, distinct resonance peaks are usually found in the 1.5-2.5 MeV neutron energy region, where the total neutron cross section (especially that of hydrogen) is large and therefore neutron penetration is poor. The resonance peaks are 10-30 keV in width,

which requires a thin target to maintain a beam of essentially mono-energetic neutrons. A small viewing angle (θ<10°) is required so that the neutron energy fall-off across the image is significantly smaller than the difference between on and off resonance energy. Different energy neutrons are obtained by changing accelerator energy, an undesired requirement in industrial applications. The thin lithium target is difficult to handle and maintain. It's helpful to demonstrate the concept, but it is not recommended for use.

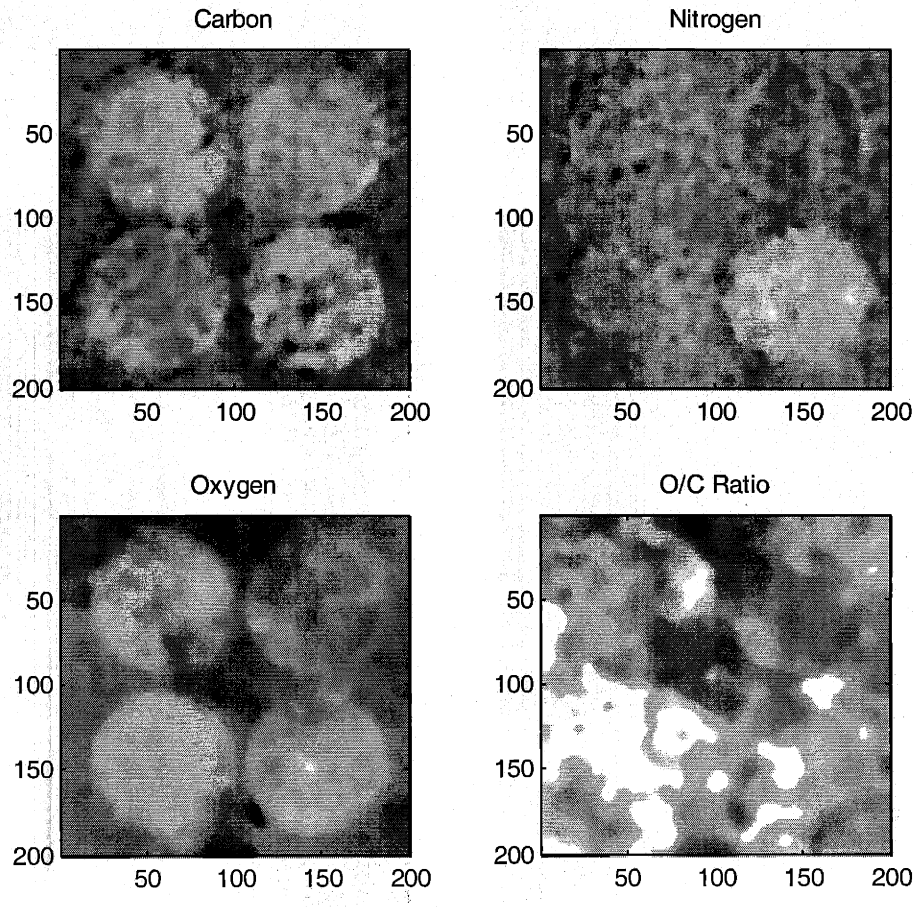

Figure 3.4 Single-peak resonance radiography (ZnS-polypropylene)

3.2 Neutron Resonance Radiography with Broad Peaks

In neutron resonance radiography we used isolated resonance peaks. Only one element is at resonance at each peak, and the difference between on-resonance and off-resonance images gives the mapping of that element. In the presence of more elements, it becomes difficult to find distinct resonance peaks for all elements of interest. In addition, neutron resonance radiography with distinct resonance peaks suffers from the following problems: (1) hydrogen has no resonance; (2) distinct peaks are narrow (10 keV-30 keV is typical), thus thin targets are required, which leads to inefficient use of accelerated particles; (3) neutron penetration is poor. To improve the method, we turn to look at the broad resonance structure at neutron energy of 2-6 MeV, and introduce neutron resonance radiography with broad peaks. We use the acronym of Neutron Resonance Radiography (NRR) for resonance radiography with broad peaks.

3.2.1 Linear Attenuation Model

In the 1 MeV-2 MeV neutron energy region, distinct are picked for resonance radiography. Now we turn to 2 MeV-6 MeV energy region, where the peaks are even broader, which favors the use of a large energy-spread neutron source (from a thick target). Figure 3.5 gives the total neutron cross section of hydrogen, carbon, nitrogen, and oxygen. Unfortunately, peaks of different elements overlap in energy, the simple difference method does not work any more.

Let us arbitrarily pick an energy bin [E_1, E_2] that contains resonance feature of one or more elements. Neutrons with energy within [E_1, E_2] (any distribution) travel through the bulk material, and the transmitted neutrons are recorded. Inter-molecular effects can be ignored and scattering buildup is not considered for now. Each element attenuates neutrons as if there were only this single element in the path, and that the total attenuation b is the sum of attenuation by all elements present. That is:

$$a_H x_H + a_C x_C + a_N x_N + a_O x_O + a_{Fe} x_{Fe} + \cdots = b \tag{3.1}$$

where a_H, a_C, a_N, a_O, a_{Fe}... are the overall attenuation coefficients, and x_H, x_C, x_N, x_O, x_{Fe}, ... are the contents of these elements. (From now on we use a for attenuation, in order to be consistent with the notation in mathematics.)

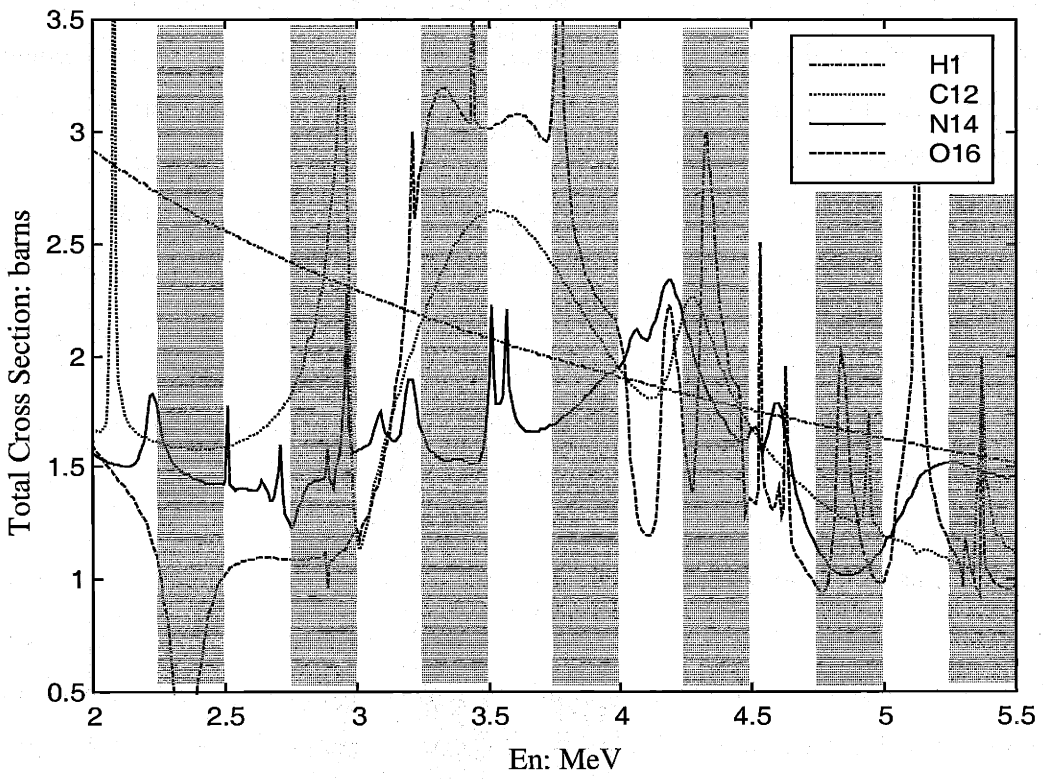

Figure 3.5 Total neutron cross section of H, C, N, O

The contents x have units of $\#/cm^2$, number of atoms per square centimeter, and the attenuation coefficients a have units of 10^{-24} cm^2 (1 barn). While the overall attenuation coefficients are related to the cross sections and also have the same units, they are not equal to the average of corresponding cross sections in general.

First, mathematically, the average of an exponent is not equal to the exponent of the average. To show this clearly, we consider the simplest case: only one element is present (x is known) and the source neutron has a flat distribution in the energy range [E_1, E_2]. The total source neutron number is N_0, and the transmitted neutron number is:

$$N = \frac{N_0}{E_2 - E_1} \int_{E_1}^{E_2} e^{-x \bullet \sigma(E)} dE \neq N_0 \bullet e^{-x \bullet AVE(\sigma)} \tag{3.2}$$

In industrial applications of radiation measurement, such as on-line monitoring, N is approximated by introducing a correction term [26]:

$$N = N_0 \bullet e^{-x \bullet [AVE(\sigma) - k \bullet STD(x \bullet \sigma)]} \tag{3.3}$$

where *STD* means standard deviation and k is a scaling constant.

Second, scattering contributes the most significant part to the total cross section (thus to attenuation), but the scattered neutron might still be transmitted and recorded. This is called scattering buildup.

The single equation (3.1) stating that the total attenuation is the sum of attenuation by all elements is not sufficient to tell us the contents of any element. We thus take radiographic images at more energy bins and obtain more similar equations. For example, we can take m radiographic image at m energy bins for the bulk material composed of n elements, and we obtain the following equations for each pixel over the image:

$$\begin{aligned}
&a_{11} x_1 + a_{12} x_2 + a_{13} x_3 + \ldots + a_{1j} x_j + \ldots + a_{1n} x_n = b_1 \\
&a_{21} x_1 + a_{22} x_2 + a_{23} x_3 + \ldots + a_{2j} x_j + \ldots + a_{2n} x_n = b_2 \\
&\qquad \ldots\ldots\ldots\ldots\ldots\ldots\ldots\ldots \\
&a_{i1} x_1 + a_{i2} x_2 + a_{i3} x_3 + \ldots + a_{ij} x_j + \ldots + a_{in} x_n = b_i \\
&\qquad \ldots\ldots\ldots\ldots\ldots\ldots\ldots\ldots \\
&a_{m1} x_1 + a_{m2} x_2 + a_{m3} x_3 + \ldots + a_{mj} x_j + \ldots + a_{mn} x_n = b_m
\end{aligned} \tag{3.4}$$

We can write the equations in the compact matrix form, $Ax = b$. The attenuation coefficients can be determined by experiment or by simulation. As long as $m \geq n$, the equation set is solvable. Note that:

1. We assume no knowledge of the source neutron's energy distribution. In other words, any distribution is acceptable.
2. We put no restriction on the selection of energy bins. They are not required to have equal spacing or equal width. Of course, there must be some resonance feature within each energy bin.

3.2.2 Affecting Factors

Scattering Buildup

Recall that scattering is the major contributor to total cross section and that scattered neutrons might still be recorded. That is, not only the neutrons that undergo no interaction transmit, but also some of those that have been scattered. This fact is called scattering buildup. As a result, the attenuation coefficient is always smaller than that corresponding to the average cross section.

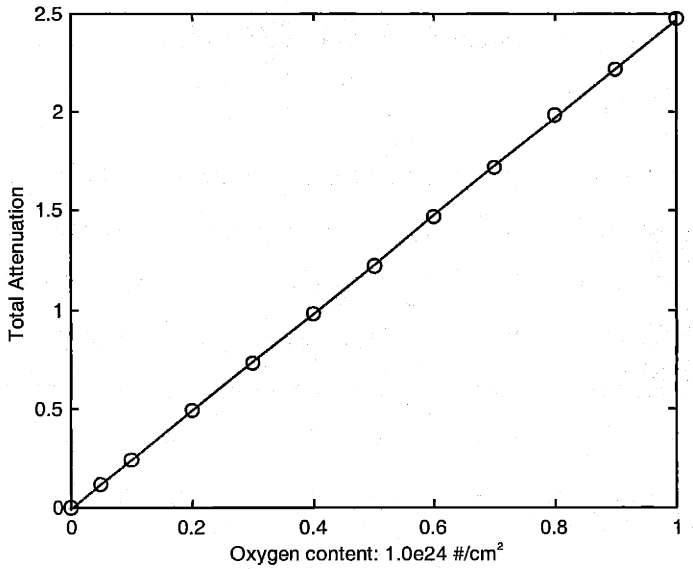

Figure 3.6: Attenuation (Oxygen, 3.25-3.5 MeV neutrons)

Scattering buildup and the "average of exponent" effect mentioned previously make it very difficult to calculate the attenuation coefficients from the total cross section. These two factors are nonlinear and need to be reduced. The only way to reduce the effect of scattering buildup is to move the neutron detector away from the inspected object. Simulation shows that 30-50 cm between the object (assuming a passenger bag) and scintillator is adequate. To see how well it works, we plot the attenuation-content fitting of oxygen. The energy bin is 3.25 MeV-3.5 MeV with a flat energy distribution, and the attenuation is obtained by MCNP simulation. (Statistical error is 1-2%.) It is clear that there exists a linear relationship up to 10^{24} #/cm^2 of material (See figure 3.6). The

resulting attenuation coefficient is 2.47×10^{-24} cm^2, compared with a total cross section of about 3 barns.

Mutual Interference

The fitted attenuation coefficient of an element for source neutrons (energy bin, distribution) includes the scattering effect. This makes our linear model work for single element objects. When two or more elements are present, mutual interference exists. That is, the presence of one element may influence the overall attenuation of another element.

Scattered neutrons have lower energy than the original neutrons. When there are two or more elements in the bulk material, each element is exposed to neutrons with a spectrum different from that of the source neutrons. This makes our linear model less accurate. Fortunately, when we reduce the scattering buildup by moving the neutron detector away from object, mutual interference also decreases.

Elements of Less Interest

The attenuation coefficient matrix a is determined in advance and the total attenuation vector b is measured experimentally. The elemental contents are calculated from the linear equations $Ax = b$. If the number of equations is less than the number of elements in consideration, or if $m < n$, there is no definite solution.

In our application, we are mostly interested in hydrogen, carbon, nitrogen, and oxygen. Other elements that are very likely to be present are aluminum, silicon, phosphorus, sulfur, chlorine, and iron. This is a total of at least ten elements. In addition, we may want several extra equations ($m > n$) so that a least squares solution is possible. With error sources of all kinds, least squares solutions are generally more stable than solutions from a definite equation set ($m = n$).

As we have mentioned, an equation derives from a measurement (a radiographic image). More measurements lead to higher cost and lower output in practice. Therefore, we would like to reduce the number of equations. Since there must be more equations

than elements involved in our linear model *(m > n)*, we must use fewer constituents to represent all elements in the model (decrease *n* in the equation).

To decrease the components used in the linear model, we represent two or more elements by one attenuation coefficient set $(a_{1j}, a_{2j}, a_{3j}, ..., a_{ij}, a_{mj})^T$ in the linear equations. Ideally, we hope to use 1–3 coefficient sets to represent all elements other than H, C, N, O. By doing this, we limit the components in the linear equations to 5–7, at the cost of a modeling error. Later on we will evaluate this cost in detail.

Summary

We now summarize this section.

1. Total attenuation is considered to be the sum of that of individual elements, as if they were present alone.
2. Attenuation coefficients are determined by experiment or by simulation in advance.
3. Total attenuation is obtained from measurement (radiographic image).
4. *There are m* equations obtained from measurements in *m* energy bins (m > n).
5. Elemental contents are obtained by solving an equation set $Ax = b$.
6. Increasing object-scintillator distance reduces scattering buildup, the "average of exponent" effect, and mutual interference.
7. Elements of less interest are represented by a reduced number of constituents in the linear model. This reduces the number of equations (measurements) needed.

As an example, we give the simulated attenuation coefficients of two groups of elements. (Figures 3.6&3.7.) Source neutrons have a flat distribution at energy bins: [2.25 MeV, 2.5 MeV], [2.5 MeV, 2.75 MeV], [2.75 MeV, 3.0 MeV], [3.0 MeV, 3.25 MeV], [3.25 MeV, 3.5 MeV], [3.5 MeV, 3.75 MeV], [3.75 MeV, 4.0 MeV], [4.0 MeV, 4.25 MeV], [4.25 MeV, 4.5 MeV], [4.5 MeV, 4.75 MeV], [4.75 MeV, 5.0 MeV], [5.0 MeV, 5.25 MeV]. As expected, the attenuation coefficients have a similar profile as the corresponding total cross section, and Al, P, S, Cl have similar attenuation coefficients.

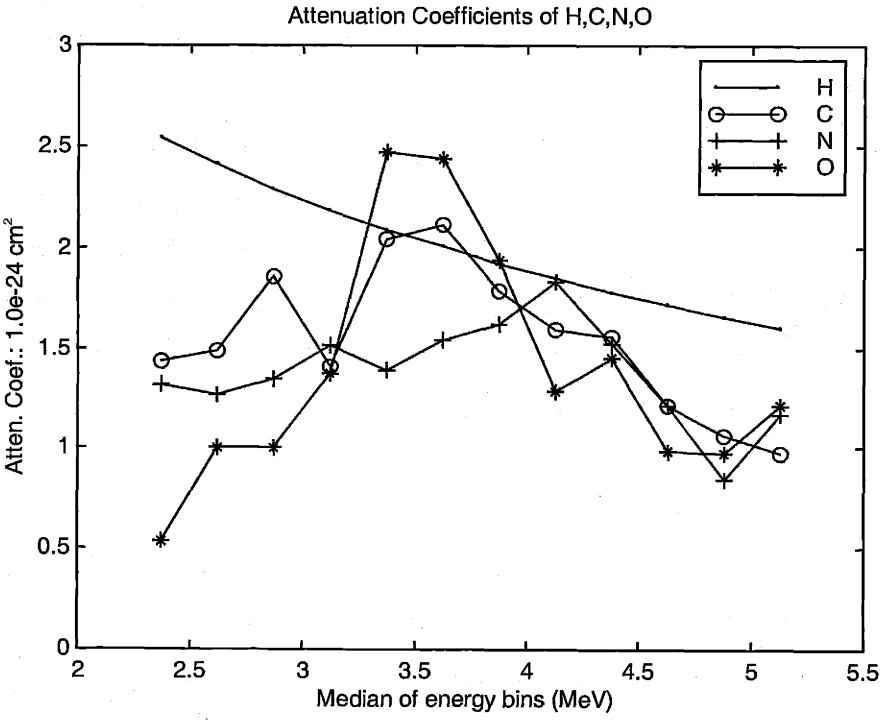

Figure 3.7 Attenuation coefficients of H, C, N, O

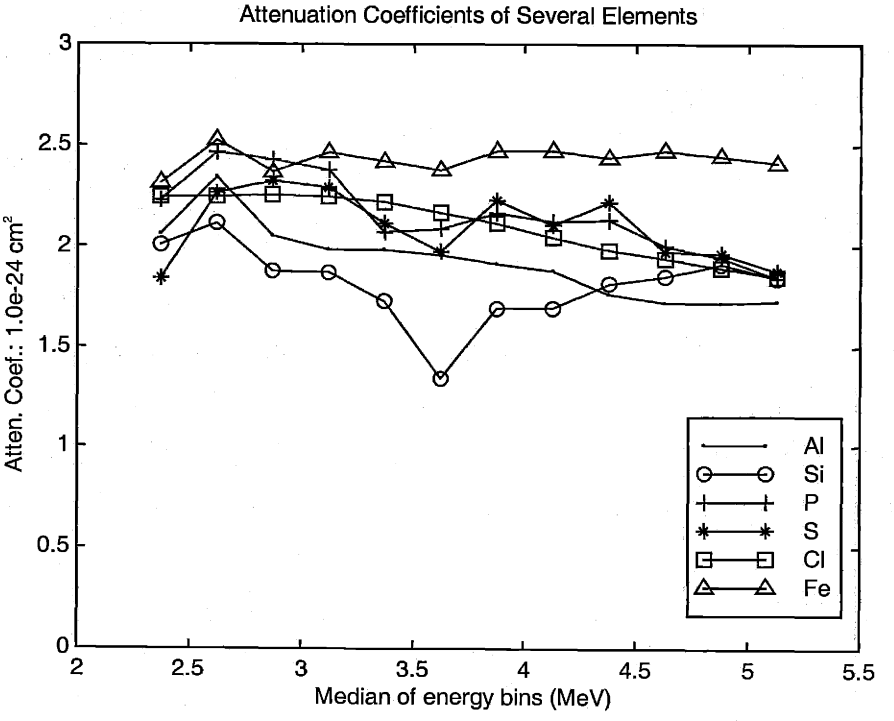

Figure 3.8 Attenuation coefficients of less interesting elements.

3.3 Least Squares Methods

Consider the problem of finding the elemental composition vector $x \in R^n$, where R is the vector space, such that $Ax = b$ when the attenuation coefficient matrix $A \in R^{mxn}$ and the measured attenuation vector $b \in R^m$ are given. Usually we have more equations than unknowns, that is $m>n$, and the set is over-determined. Unless b belongs to $R(A)$, the vector space defined by A, the over-determined set has no exact solution. There are many possible ways of defining the "best" solution.

3.3.1 Ordinary Least Squares (LS)

Any vector x_{LS} that minimizes $||Ax-b||_2$ is called a (ordinary) least squares (LS) solution of the set $Ax = b$. An LS solution satisfies the normal equations

$$A^T A\, x = A^T b \tag{3.5}$$

The matrix $A^T A$ is symmetric and nonnegative definite, and the normal equations are always consistent. In the full rank case, there is only one LS solution with the following closed-form expression:

$$x_{LS} = (A^T A)^{-1} A^T b = A^{\dagger} b \tag{3.6}$$

Where $A^{\dagger}$ is the pseudo inverse of A. And the residual error on b is:

$$\Delta b = [\Delta b_1, \Delta b_2, ..., \Delta b_m]^T = (A\, x_{LS} - b) \tag{3.7}$$

When the Δb_i have zero mean, and are uncorrelated random variables with equal variance, the LS solution fulfills the following two conditions:

1. There are no systematic errors (no bias) in the estimates.
2. The estimates are linear functions of b.

The second condition is of great computational importance. Because the pseudo inverse $A^{\dagger}$ is independent of b, we can calculate $A^{\dagger}$ before the measurement vector b is available. This makes our real-time or on-site process less computation-intensive. Now let us rewrite the equations as:

$$A_1 x_1 + A_2 x_2 + \ldots + A_n x_n = b \tag{3.8}$$

where A = (A_1, A_2, ..., A_n), and A_1, A_2, ..., A_n, and b are *m*-dimensional vectors. We then project vector b onto the hyper plane R (A) = R (A_1, A_2, ..., A_n),The projection b_{Proj} lies in the hyper plane R(A), and there is an exact solution x_{LS} for the equations:

$$A\,x = b_{proj.} \tag{3.9}$$

When $n=1$, i.e., x becomes a scaler, there is only one unknown to be estimated from the equations: $a_i\,x = b_i,\ i = 1, 2, \ldots, m.$

The LS method minimizes $\sum_{i=1}^{m} (b_i - a_i x)^2$, and the solution is (figure 3.9):

$$x_{LS} = \sum_{i=1}^{m} (a_i * b_i) \Big/ \sum_{i=1}^{m} a_i^2 \tag{3.10}$$

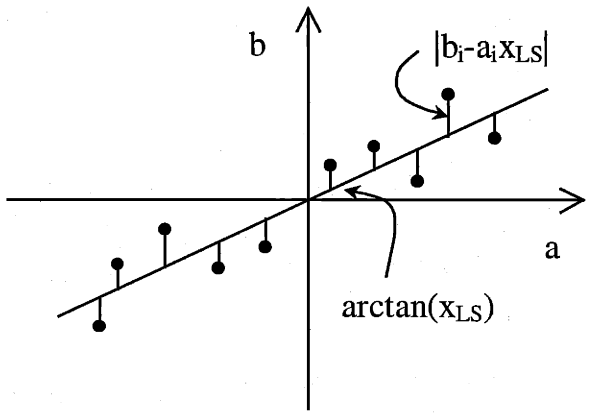

Figure 3.9 Geometric interpretation of LS method

3.3.2 Selective Least Squares (SLS)

In the LS method, we project vector *b* onto the hyper plane *R (A) = R (A_1, A_2, ..., A_n)*, and the exact solution x_{LS} of the resulting equations $A\ x = b_{proj}$ minimizes the squared residual error on *b*.

Sometimes the major source of error may occur on a vector (A_j) other than *b*. We therefore want to selectively minimize the squared residual error on that vector. In other

words, we want to project the vector A_j onto the hyper plane $R(A_1, A_2, ..., A_{j-1}, ..., A_{j+1}, ..., A_n, b)$ and solve the resulting projection equations, which have an exact solution x_{SLS}. Now we need to minimize the square residual error SE on vector A_j:

$$SE = \left(\frac{\sum_{k=1}^{n} a_{1k} * x_k - b_1}{a_{1j}} \right)^2 + \left(\frac{\sum_{k=1}^{n} a_{2k} * x_k - b_2}{a_{2j}} \right)^2 + ... + \left(\frac{\sum_{k=1}^{n} a_{mk} * x_k - b_m}{a_{mj}} \right)^2 \quad (3.11)$$

Let $\partial SE/\partial x_i = 0$, we have:

$$A^T * \begin{pmatrix} 1/a_{1j} & 0 & ... & 0 \\ 0 & 1/a_{2j} & ... & 0 \\ ... & ... & ... & ... \\ 0 & 0 & ... & 1/a_{mj} \end{pmatrix}_{mxm} * (Ax - b) = 0 \quad (3.12)$$

and the SLS solution can be expressed in the closed-form:

$$x_{SLS} = (A^T [*] A)^{-1} A^T [*] b \quad (3.13)$$

Where $[*]$ denotes the matrix in the previous expression. Noting that:

$$x_{SLS} = \left(\left(\sqrt{[*]} * A \right)^T * \left(\sqrt{[*]} * A \right) \right)^{-1} * \left(\sqrt{[*]} * A \right)^T * b \quad (3.14)$$

The SLS solution is obtained in two steps:

1. Multiply the original equation by $\sqrt{[*]}$ from the left.
2. Follow the Ordinary Least Squares (LS) procedure for a solution.

Apparently, the SLS solution is a linear function of the measurement vector b. When $n=1$, i.e., x becomes a scaler, there is only one unknown to be estimated from the equations: $a_i x = b_i$, $i = 1, 2, ..., m$.

The SLS method minimizes $\sum_{i=1}^{m} (b_i / x - a_i)^2$, and the solution is (figure 3.10):

$$x_{SLS} = \sum_{i=1}^{m} b_i^2 \Big/ \sum_{i=1}^{m} (a_i * b_i) \quad (3.15)$$

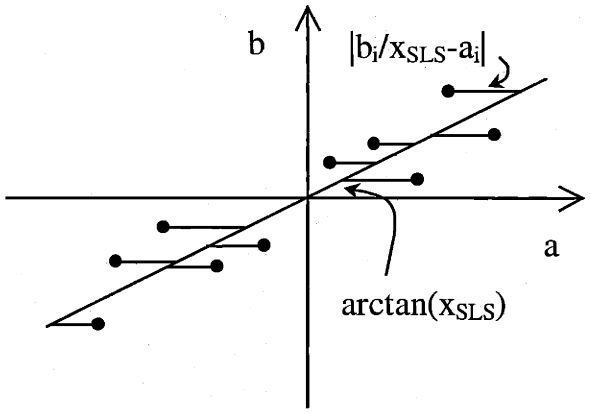

Figure 3.10 Geometric interpretation of SLS method

3.3.3 Total Least Squares (TLS)

Very often errors occur in both A and b. We thus want to treat A and b symmetrically. The Total Least Squares (TLS) method seeks to minimize

$$\| [A, b] - [\underline{A}, \underline{b}] \|_F, \text{ subject to the constraint of } \underline{b} \in R^m.$$

In other words, we look to find modified $\underline{A}$ and $\underline{b}$, so that $\underline{b}$ lies in the hyper-plane of $R(\underline{A}) = R(\underline{A}_1, \underline{A}_2, ..., \underline{A}_n)$, and the distance from $[A, b]$ to $[\underline{A}, \underline{b}]$ is minimized. The TLS solution x_{TLS} is the exact solution of the following equations: $\underline{A}\, x = \underline{b}$.

The total Least Squares problem is usually solved by Single Value Decomposition (SVD), and x_{TLS} can be expressed in closed-form:

$$x_{TLS} = (A^T A - \sigma^2_{n+1} I)^{-1} A^T b. \tag{3.16}$$

where σ_{n+1} is the $n+1^{th}$ diagnostic element from the SVD procedure and I the identity matrix. Unlike Ordinary Least Squares or Selective Least Squares methods, the TLS solution is not a linear function of vector b. This is seen from the fact that σ_{n+1} is obtained from a Single Value Decomposition of $[A, b]$ and thus depends on b.

When $n=1$, i.e., x becomes a scaler, there is only one unknown to be estimated from the equations: $a_i x = b_i$, $i = 1, 2, ..., m$.. The TLS method minimizes $\sum_{i=1}^{m} \frac{(b_i - a\ x)^2}{1+x^2}$.

Figure 3.11 illustrates the TLS method. The deviations are orthogonal to the fitted line: it is the sum of squares of their length that is minimized. Therefore, the TLS method is also known as orthogonal regression.

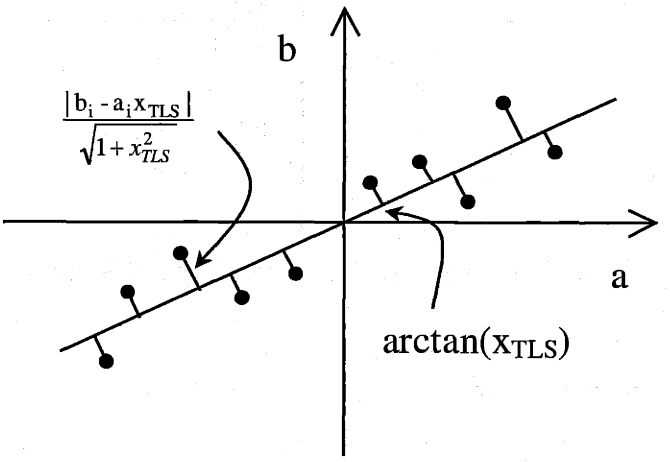

Figure 3.11 Geometric interpretation of the TLS method

3.3.4 Comparison

It is often thought that the Ordinary Least Squares method relies on the assumption that matrix (*A*) is exactly known and errors only occur in the measurement vector (*b*). In other words, people tend to think that the LS method does not consider errors in matrix *A* and LS only minimizes errors in vector *b*. Indeed, this is not correct.

In the Total Least Squares method, vector *b* and the vectors in matrix *A* are treated symmetrically. The errors in matrix *A* and that in vector *b* are all considered explicitly, which is a more reasonable description of the physics. The LS or SLS method, on the other hand, converts all error into a single vector and minimizes it. Errors in other vectors are not treated explicitly. However, we cannot say that some errors have been ignored. Each of the three methods mentioned above seeks to minimize a target function, the sum of certain squared residual errors. However, none of them minimizes the error of the unknown *x*. That is, no method minimizes $|x - x_t|^2$ from *A* and *b*, where x_t is the true value. For this reason, no method is better than another one.

It has been proved that the performance of the TLS method is better than the LS method if the following conditions are fulfilled:

1. There is no error in the linear model itself.
2. Errors in the matrix A and vector b are independent random variables with zero mean and equal variance.
3. The equation set is significantly over-determined, that is $m>>n$.

In NRR, none of the above conditions is satisfied. The model does not consider cross interference of elements, and it represents elements other than (H, C, N, O) by very few components. Matrix A can generally be determined with smaller errors than vector b is, and errors in different equations are generally different. More importantly, we can not afford too many equations—each equation means another radiographic image.

We tried the LS method to minimize squared residual errors on b, the SLS method to minimize that on each element (one at a time), and the TLS method to minimize the overall squared errors. It turns out that the LS method is at least no worse than SLS or TLS, for the reasons stated in the last paragraph.

3.3.5 Householder Transform

The LS solution of over determined equations $A\,x = b$ is expressed as:

$$A^T A\,x = A^T b \implies x_{LS} = (A^T A)^{-1} A^T b = A^{\dagger} b. \tag{3.17}$$

This does not mean that x_{LS} should be calculated in the above manner. In fact, it is not recommended for two reasons: (1) calculating the inverse matrix is computationally intensive, (2) it introduces large errors. Suppose x_{LS} is an approximation to x_t, the true value in $Ax = b$, the relative residual error on b is:

$$\varepsilon = \| Ax_{LS} - b \| / \| b \| \tag{3.18}$$

and the relative error $\| x_{LS} - x_t \| / \| x_t \|$ satisfies:

$$\frac{\varepsilon}{\kappa(A)} \leq \frac{\| x_{LS} - x_t \|}{\| x_t \|} \leq \varepsilon \bullet \kappa(A) \tag{3.19}$$

where $\kappa(A) = \| A \| \| (A^T)^{-1} \| \geq 1$. It is called the condition number of matrix A. The relative error of x_{LS} could be as large as the relative residual error on vector b multiplied by $\kappa(A)$. When matrix A becomes large, it becomes ill-conditioned and $\kappa(A)$ is very large.

In the normal equations $A^T A\, x = A^T b$, the matrix $A^T A$ is more ill-conditioned than A. Its condition number $\kappa(A^T A) = (\kappa(A))^2$. The upper limit of error is greatly increased and it causes a very unstable solution. The Single Value Decomposition (SVD) method is commonly used to solve the equations directly, i.e., without calculating the normal equations. SVD is computationally intensive. Hei [27] suggested using the Householder transform method to solve the LS problem.

One vector can be reflected on another vector, as shown in figure 3.12.

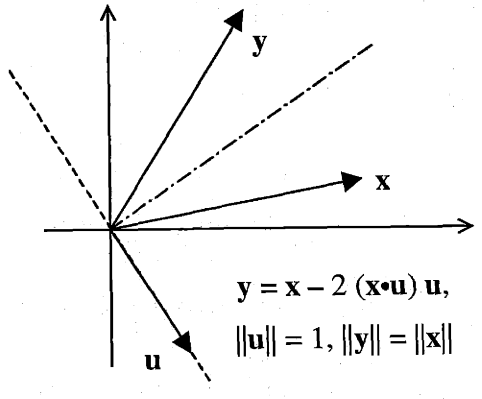

Figure 3.12 Vector reflection

The image vector **y** is determined by the object vector **x** and the mirror vector **u**. On the other hand, if we have the object vector **x** and want to reflect it into a certain direction (For example, $\mathbf{y} = \| \mathbf{x} \| \mathbf{e}_1$, where $\mathbf{e}_1 = (1, 0, 0, ..., 0)^T$), we can find the mirror vector **u** from the reflection equation $\mathbf{y} = \mathbf{x} - 2\,(\mathbf{x} \bullet \mathbf{u})\,\mathbf{u} = \| \mathbf{x} \| \mathbf{e}_1$.

$$\mathbf{u} = \frac{\mathbf{x} - \| \mathbf{x} \| \mathbf{e}_1}{\| \mathbf{x} - (\| \mathbf{x} \| \mathbf{e}_1) \|} \tag{3.20}$$

That is, $\mathbf{u}$ can be found by subtracting from $\mathbf{x}$ the desired image $\|\mathbf{x}\|\ \mathbf{e}_1$. Normalization is then needed of course. In matrix form,

$$\mathbf{y} = (\mathrm{I} - 2\,\mathbf{u}\,\mathbf{u}^{\mathrm{T}})\,\mathbf{x} = \|\mathbf{x}\|\ \mathbf{e}_1 \tag{3.21}$$

where $\mathbf{u}$ is found in the above expression. The matrix $Q = I - 2\,\mathbf{u}\,\mathbf{u}^{\mathrm{T}}$ is called a Householder Matrix. It is orthogonal and normalized. It has the following properties:

$$Q^T = Q;\ Q^TQ = I;\ Q^2 = I;\ Q^{-1}=Q \tag{3.22}$$

Now it is straightforward to up-triangularize matrix A column by column (treat each column as an object vector, one at a time), till it consists of n up-triangularized equations and m-n residual equations. We can thereafter solve the n equations by backward elimination.

The process is expressed as: $Q_n\,Q_{n-1}\,...Q_2\,Q_1 A\,x = Q_n\,Q_{n-1}\,...Q_2\,Q_1\,b$, *or*

$$\begin{bmatrix} a_{11} & a_{12} & \cdots & a_{1n} \\ a_{21} & a_{22} & \cdots & a_{2n} \\ \cdots & \cdots & \cdots & \cdots \\ a_{n1} & a_{n2} & \cdots & a_{nn} \\ \cdots & \cdots & \cdots & \cdots \\ a_{m1} & a_{m2} & \cdots & a_{mn} \end{bmatrix} \bullet x = \begin{bmatrix} b_1 \\ b_2 \\ \cdots \\ b_n \\ \cdots \\ b_m \end{bmatrix} \Rightarrow \begin{bmatrix} a_{11} & a_{12} & \cdots & a_{1n} \\ 0 & a'_{22} & \cdots & a'_{2n} \\ \cdots & \cdots & \cdots & \cdots \\ 0 & a'_{n2} & \cdots & a'_{nn} \\ \cdots & \cdots & \cdots & \cdots \\ 0 & a'_{m2} & \cdots & a'_{mn} \end{bmatrix} \bullet x = \begin{bmatrix} b_1 \\ b'_2 \\ \cdots \\ b'_n \\ \cdots \\ b'_m \end{bmatrix} \Rightarrow \ldots \Rightarrow \begin{bmatrix} * & * & \cdots & * \\ 0 & * & \cdots & * \\ \cdots & \cdots & \cdots & \cdots \\ 0 & 0 & \cdots & * \\ \cdots & \cdots & \cdots & \cdots \\ 0 & 0 & \cdots & 0 \end{bmatrix} \bullet x = \begin{bmatrix} * \\ * \\ \cdots \\ * \\ \cdots \\ \Delta \end{bmatrix} \tag{3.23}$$

$Q = Q_n\,Q_{n-1}\,...Q_2\,Q_1$ is also orthogonal and normalized. The resulting matrix QA is no more ill-conditioned than matrix A, $\kappa(QA)= \kappa(A)$. In other words, the Householder transform does not increase the upper limit of error. Therefore we can in general expect this method to be more stable than other methods.

In the detailed matrix expression above, * marks represent modified numbers and Δ represents small residual errors. It is easy to prove that the Householder method leads to the same solution as the normal equation does, $x_H = x_{TLS}$. When programming, there is no need to calculate the matrices Q1, Q2...explicitly.

3.4 Optimizing NRR

So far we have introduced a linear model to describe the total attenuation of neutrons and the Householder transform to solve the over-determined equation set. Let us now consider how we should construct this equation set for good NRR performance.

3.4.1 Method

We are concerned with the following questions:

1. How many components are needed to describe the elements of less interest?
2. How many and which energy bins (measurements) are necessary?
3. How can we handle gamma rays recorded by the scintillator?
4. To what extent do scattering and mutual interference influence the performance?
5. What is the S/N requirement on measurements?

Questions 1-4 are answered by studying the *stability* and *bias* of the NRR solution, and the answer is verified by the *relative error* from simulated pseudo samples. The S/N requirement is also studied by simulation.

We do not solve the matrix equation $Ax = b$ directly. Instead we find $A^{\dagger}$, the pseudo inverse of matrix A. When the measurement vector b is available thereafter, the contents can be calculated by $x = A^{\dagger}b$. In addition, we are only interested in the contents of H, C, N, O and the sum of all other elements, so we add the row vectors in $A^{\dagger}$ representing elements other than H, C, N, O to get the total content coefficients of all elements of less interest. (Only the sum of all other elements is needed in the final report, but more than one constituents might be needed when solving the equation set.) We denote it by $C = Combine\ (A^{\dagger})$. That is, the row vectors for H, C, N, O contents in matrix C are the same as those in matrix $A^{\dagger}$, but the fifth row vector in matrix C is the sum of all other vectors in matrix $A^{\dagger}$. The five-constituent contents are then calculated by $x' = Cb$.

$$A_{mxn} A^{\dagger}_{nxm} = I_{mxm} \Longrightarrow A^{\dagger}_{nxm} \Longrightarrow C_{5xm};\ Ax = b \Longrightarrow x = A^{\dagger}b \Longrightarrow x' = Cb \qquad (3.24)$$

Our study is still based on the ten elements and 12 energy bins mentioned in section 3.2. The source neutrons have a flat distribution within each energy bin. When fewer than 10 constituents are used in the model, the selection of representing elements is given in Table 3.2. (All elements exist, but they are represented by the selected elements.) When fewer than 12 energy bins are used, the selected bins are listed in Table 3.3.

Table 3.2 Representing elements used

Number of constituents	H, C, N, O	Al	Si	P	S	Cl	Fe
4	xxxx						
5	xxxx						x
6	xxxx	x					x
7	xxxx		x	x			x
8	xxxx	x	x	x			x
9	xxxx	x	x	x		x	x
10	xxxx	x	x	x	x	x	x

Table 3.3: Neutron energy bins used (in MeV)

Number of Bins Used	2.25 -2.5	2.5-2.75	2.75 -3.0	3.0-3.25	3.25 -3.5	3.5-3.75	3.75 -4.0	4.0-4.25	4.25 -4.5	4.5-4.75	4.75 -5.0	5.0-5.25
6	x	x		x		x		x		x		
7	x	x	x	x		x		x		x		
8	x	x	x	x		x		x		x		x
9	x	x	x	x		x		x		x	x	x
10	x	x	x	x		x		x	x	x	x	x
11	x	x	x	x		x	x	x	x	x	x	x
12	x	x	x	x	x	x	x	x	x	x	x	x

Now let us illustrate the process with an example. We use 7 components in the equations. They are: H, C, N, O, Si, P, Fe. We take measurements (radiographic image)

in 8 energy bins. The matrix A_{8x7} is formed with the attenuation coefficients (See Section 3.2.) of the 7 elements in the 8 energy bins. The pseudo inverse matrix $A^{\dagger}_{7x8}$ is calculated, and combined into the five-constituent content coefficient matrix C_{5x8}. The five-constituent solution can be found from $x = Cb$.

$$A = \begin{bmatrix} 2.5440 & 1.4365 & 1.3223 & 0.5353 & 2.0063 & 2.2272 & 2.3119 \\ 2.4115 & 1.4890 & 1.2696 & 0.9995 & 2.1149 & 2.4656 & 2.5275 \\ 2.2890 & 1.8577 & 1.3434 & 0.9997 & 1.8770 & 2.4264 & 2.3629 \\ 2.1811 & 1.4076 & 1.5098 & 1.3710 & 1.8662 & 2.3782 & 2.4594 \\ 2.0021 & 2.1099 & 1.5428 & 2.4371 & 1.3360 & 2.0894 & 2.3790 \\ 1.8458 & 1.5920 & 1.8293 & 1.2818 & 1.6881 & 2.1227 & 2.4697 \\ 1.7119 & 1.2098 & 1.2181 & 0.9822 & 1.8479 & 1.9948 & 2.4700 \\ 1.5976 & 0.9805 & 1.1677 & 1.2166 & 1.8423 & 1.8407 & 2.4083 \end{bmatrix}, b = \begin{bmatrix} 1.1966 \\ 1.2916 \\ 1.2863 \\ 1.3300 \\ 1.5291 \\ 1.3251 \\ 1.0912 \\ 1.1027 \end{bmatrix},$$

$$\Rightarrow A^{+} = \begin{bmatrix} 2.0295 & -0.3232 & -2.0174 & 0.7095 & 0.8438 & -0.9057 & 1.1283 & -1.4163 \\ -0.2663 & 0.0291 & 2.1417 & -2.5021 & 0.1287 & 0.6383 & -1.4909 & 1.4264 \\ 0.1632 & -0.2215 & 0.1241 & -0.1105 & -0.5812 & 2.0100 & -2.7460 & 1.3962 \\ -0.4469 & 0.5245 & 0.2897 & -0.1130 & 0.2285 & 0.0106 & -2.4509 & 1.9869 \\ -1.1292 & 1.6923 & 4.1216 & -4.0787 & -1.3031 & 2.1227 & -9.8509 & 8.6430 \\ -2.0843 & 0.5614 & 0.3681 & 3.1621 & -0.7533 & -0.6806 & 2.0494 & -2.8386 \\ 1.3485 & -1.6062 & -3.2093 & 1.3296 & 1.1314 & -1.7178 & 8.3965 & -5.3702 \end{bmatrix}$$

$$\Rightarrow C = \begin{bmatrix} 2.0295 & -0.3232 & -0.2174 & 0.7095 & 0.8438 & -0.9057 & 1.1283 & -1.4163 \\ -0.2663 & 0.0291 & 2.1417 & -2.5021 & 0.1287 & 0.6383 & -1.4909 & 1.4264 \\ 0.1632 & -0.2215 & 0.1241 & -0.1105 & -0.5812 & 2.0100 & -2.7460 & 1.3962 \\ -0.4469 & 0.5245 & 0.2897 & -0.1130 & 0.2285 & 0.0106 & -2.4509 & 1.9869 \\ -1.8650 & 0.6474 & 1.2804 & 0.4131 & -0.9250 & -0.2757 & 0.5951 & 0.4342 \end{bmatrix}$$

$\Longrightarrow$ Five-constituent solution $x = C^{*}b = (0.1194 \quad 0.1345 \quad 0.2397 \quad 0.2450 \quad 0.1492)^{T}$, and the true value is $x_t = (0.1 \quad 0.1 \quad 0.2 \quad 0.2 \quad 0.2)^{T}$.

3.4.2 Stability

Stability is one of the most important properties of a method. Solutions from a stable method may not necessarily be the most accurate, but a stable method never leads to very large errors. In general, a more stable method also has smaller average errors.

Stability is determined from the A matrix and C matrix. The condition number of matrix A gives an upper limit of possible errors. If we are using the Householder method to solve the ordinary least squares problem $Ax = b$, and the residual error on vector b is ε,

$$\frac{\varepsilon}{\kappa(A)} \leq \frac{\| x_{LS} - x_t \|}{\| x_t \|} \leq \varepsilon \bullet \kappa(A) \tag{3.19}$$

Without any error in matrix A and the modeling, the error of the solution falls between $\varepsilon/\kappa(A)$ and $\varepsilon \bullet \kappa(A)$. One may find immediately that, while larger condition number leads to larger upper limit of the error, it also leads to a smaller lower limit of the error. In other words, a problem set with larger $\kappa(A)$ has a chance of larger errors, but it has a chance of smaller errors, too. Thus, $\kappa(A)$ is not a very good error predictor.

Each column vector in matrix A is the attenuation coefficients of one of the n components in the model, in the m selected energy bins. On the other hand, each row vector in matrix C is the content coefficient of one of the five constituents (H, C, N, O, or Sum of others). The scale product of one content coefficient vector and measurement vector b gives the content of the corresponding constituent. Matrix C has a closer relationship with elemental contents.

In our problem, the attenuation coefficients (entries in matrix A) do not vary greatly, over elements or energy. We can reasonably expect that content coefficients (entries in matrix C) vary to an extent not much greater than attenuation coefficients. In the previous example, most entries in matrix C have absolute values between 0 and 1, so an entry with a value of 5 is generally not welcome. Indeed, we can use the vector norm (2-norm) of content coefficients to quantitatively measure the stability of different selections of energy bins and components.

The vector norm in the previous example for H, C, N, O, and Sum of others is respectively 3.6889, 3.9498, 3.7378, 3.2524, and 2.6799.

We plot out the norm of row vectors in matrix C, for various combinations of number of energy bins (m) and component number (n), in Figure 3.13.

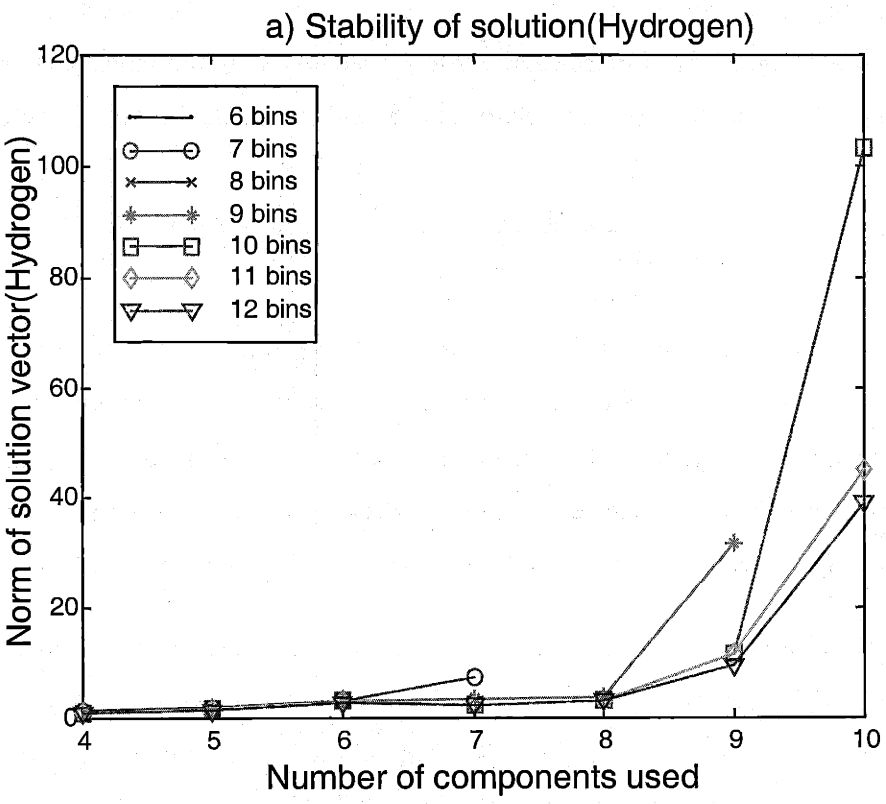
a) Stability of solution(Hydrogen)
Norm of solution vector(Hydrogen)
Number of components used
6 bins
7 bins
8 bins
9 bins
10 bins
11 bins
12 bins
0
20
40
60
80
100
120
4
5
6
7
8
9
10

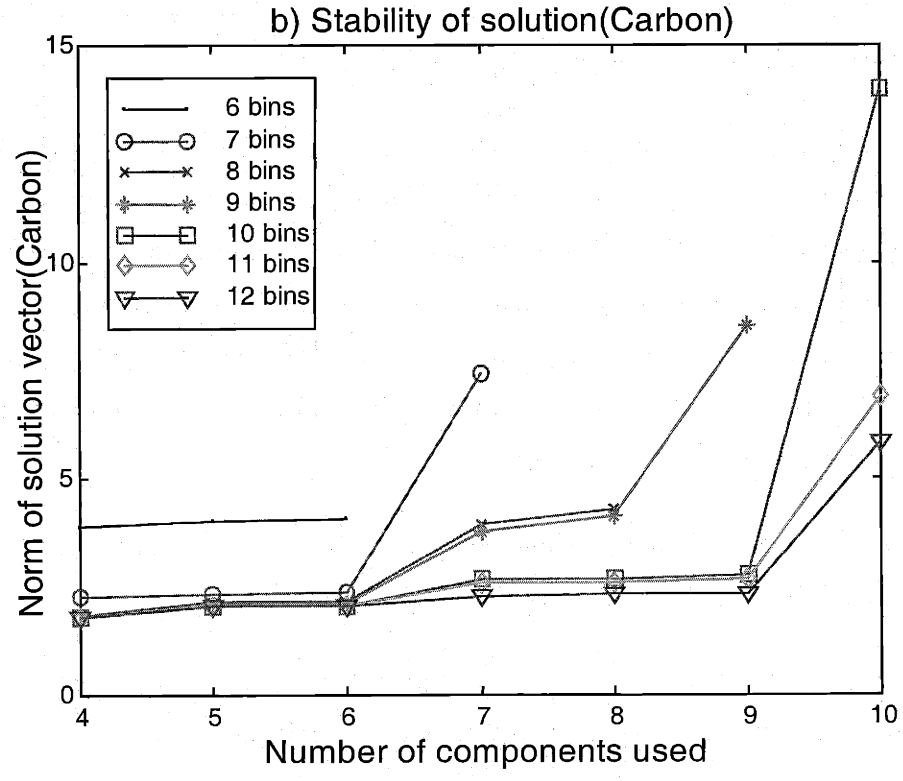
b) Stability of solution(Carbon)
Norm of solution vector(Carbon)
Number of components used
6 bins
7 bins
8 bins
9 bins
10 bins
11 bins
12 bins
0
5
10
15
4
5
6
7
8
9
10

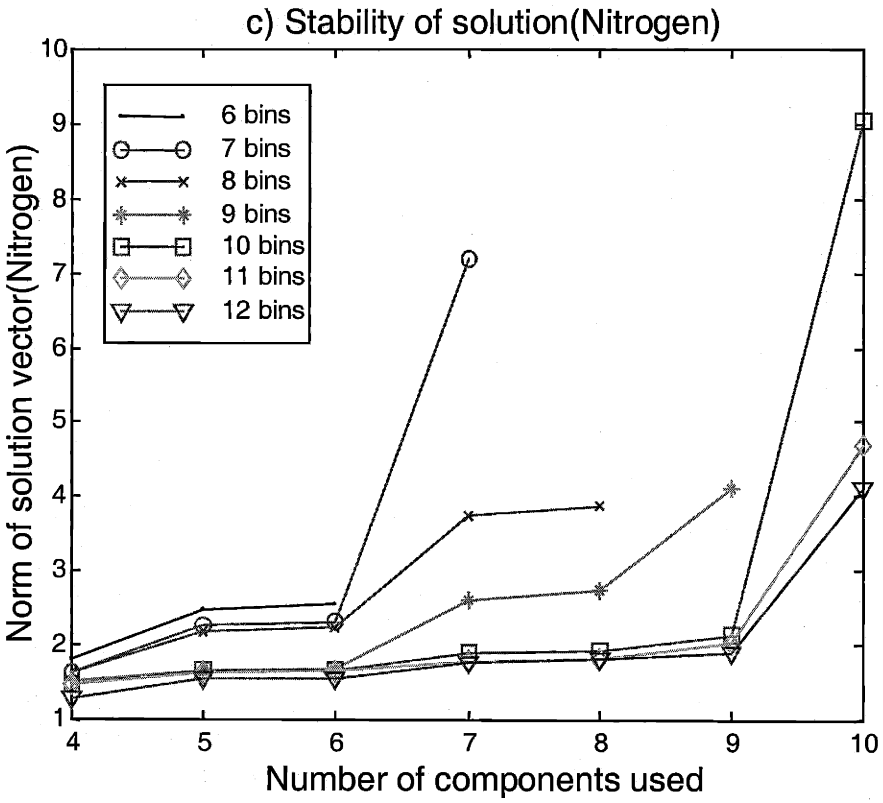
c) Stability of solution(Nitrogen)
Norm of solution vector(Nitrogen)
Number of components used
6 bins
7 bins
8 bins
9 bins
10 bins
11 bins
12 bins
1
2
3
4
5
6
7
8
9
10
4
5
6
7
8
9
10

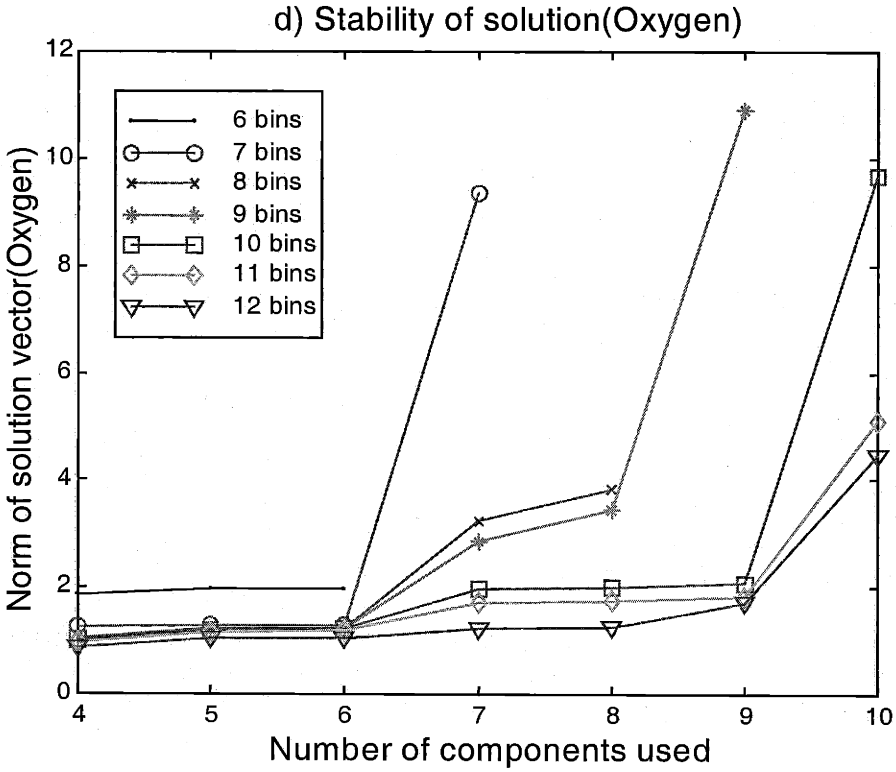
d) Stability of solution(Oxygen)
Norm of solution vector(Oxygen)
Number of components used
6 bins
7 bins
8 bins
9 bins
10 bins
11 bins
12 bins
0
2
4
6
8
10
12
4
5
6
7
8
9
10

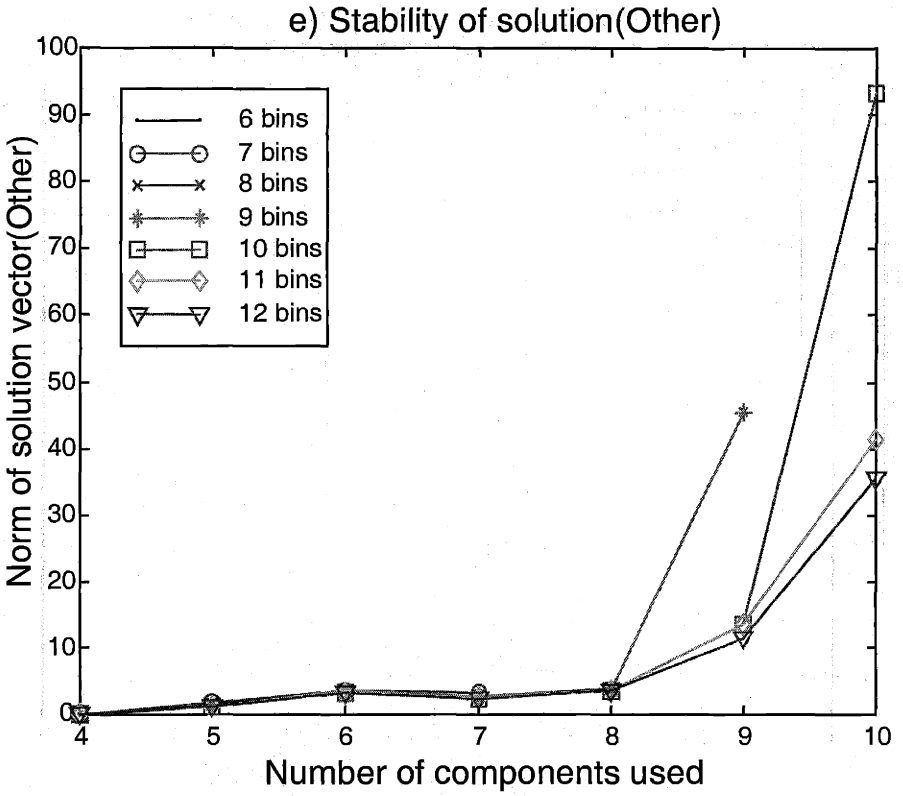

Figure 3.13 Stability of solutions for H, C, N, O, and sum of other elements

We can draw the following conclusions from the figures:

1. The vector norm increases steadily with the number of components (n) used in the equations. This is due to the increased number of entries in the row vector.

2. When more than 8 components are involved ($n > 8$) in the equations, the vector norm increases rapidly, leading to unstable solutions.

3. When there is no data redundancy (n = m), we are dealing with a determinate equation set and the vector norm is very large, leading to unstable solutions.

4. For the concern of stability, we should introduce no more than 8 components in the model, and the number of energy bins (equations) should be more than component number (That is: $n \leq 8$, and $m > n$.).

5. In addition, when ten or fewer energy bins are used, the vector norm for carbon, nitrogen, and oxygen is large if there are more than six components. (That is, when $m \leq 10$, we should keep $n < 6$.)

3.4.3 Bias

If, on average, the solution from a method tends neither to underestimate nor to overestimate the true value, we say this method is unbiased. Bias is a systematic error that could be partly compensated in some special cases. Ordinary least squares (LS) method is unbiased if there are only zero mean and equal variance errors in the measurement vector b.

Matrix C is also an indicator of bias. Recall that $A^{\dagger}$ is the pseudo inverse of A, and that $A^{\dagger}A = I$. If we set the measurement vector b to be any of the column vectors in matrix A, (the attenuation coefficients of one element in m energy bins) the LS solution will be: unity for the corresponding constituent and zero for the other four constituents. In other words, if only one element is present and if there were no measurement errors, matrix C leads to the exact solution.

Let us look back at the attenuation coefficient curves in the first section. The attenuation coefficients for the less interesting elements range between 2 and 2.5 ($x10^{-24}cm^2$). As a first order approximation, they do not change much with energy. What is the solution, then, if the measurement vector is roughly $(1 \quad 1 \quad 1 \quad 1 \quad ... \quad 1)^T$? We expect the solution to be $(0 \quad 0 \quad 0 \quad 0 \quad \sim 0.4\text{-}0.5)^T$. That is, we expect that the method reports zero content for H, C, N, and O, and ~0.4-0.5 $x10^{24}$ #/cm^2 for other elements.

This is very important not only for the modeling of less interesting elements. The background from gamma rays or neutrons scattered by environmental material varies slowly with energy. We would like the method to put these effect (error) into the content of "other elements", not the content of H, C, N, and O.

The bias property is quantitatively measured by the sum of m entries of a row vector in matrix C. (The sum of m content coefficients for one constituent.) We expect the sum to be zero for H, C, N, O, and ~0.4-0.5 for "Other elements". The sum in our example is $(0.0486 \quad 0.1049 \quad 0.0342 \quad 0.0293 \quad 0.3044)^T$. We plot out the sum of each row vector in matrix C, for various numbers of energy bins (m) and component number (n), in Figure 3.14.

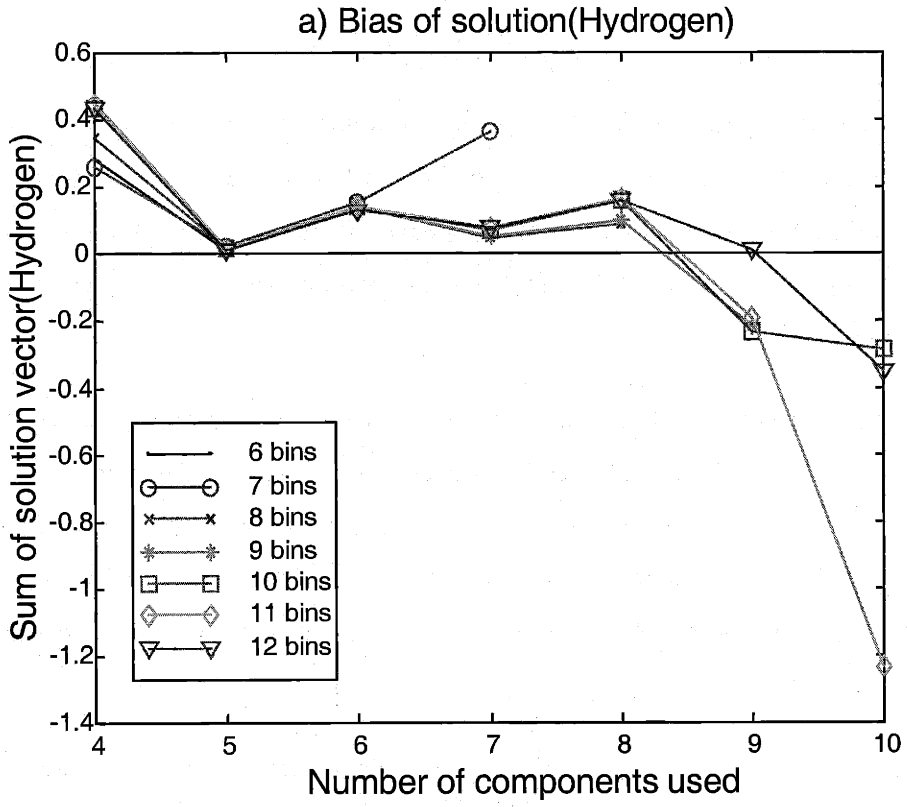
a) Bias of solution(Hydrogen)
Sum of solution vector(Hydrogen)
Number of components used
6 bins
7 bins
8 bins
9 bins
10 bins
11 bins
12 bins

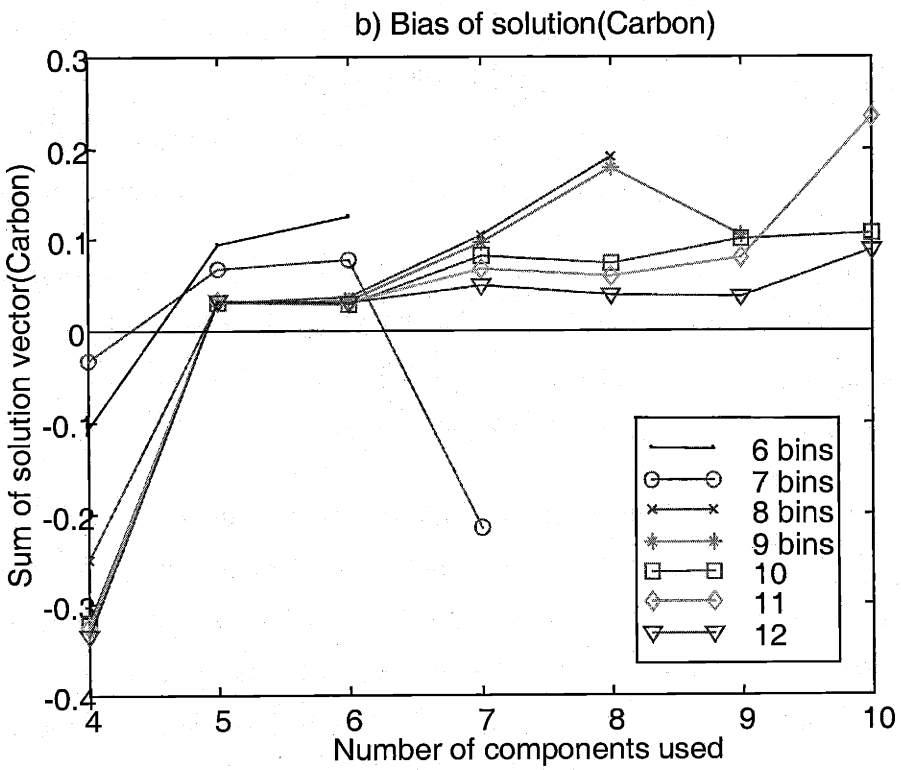
b) Bias of solution(Carbon)
Sum of solution vector(Carbon)
Number of components used
6 bins
7 bins
8 bins
9 bins
10
11
12

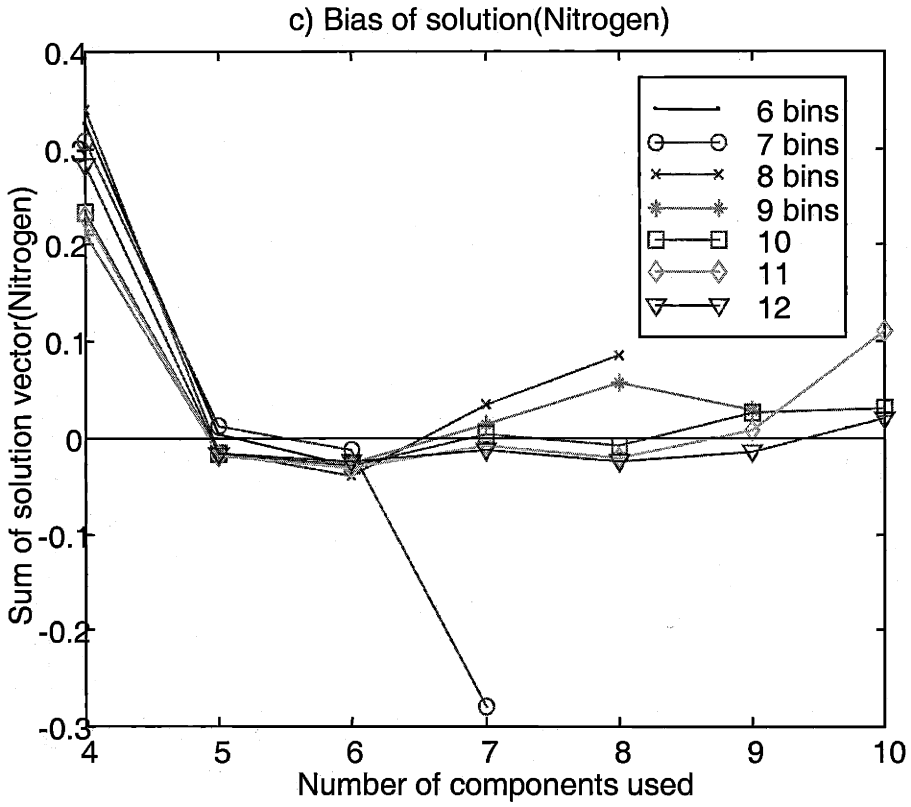
c) Bias of solution(Nitrogen)
Sum of solution vector(Nitrogen)
Number of components used
6 bins
7 bins
8 bins
9 bins
10
11
12

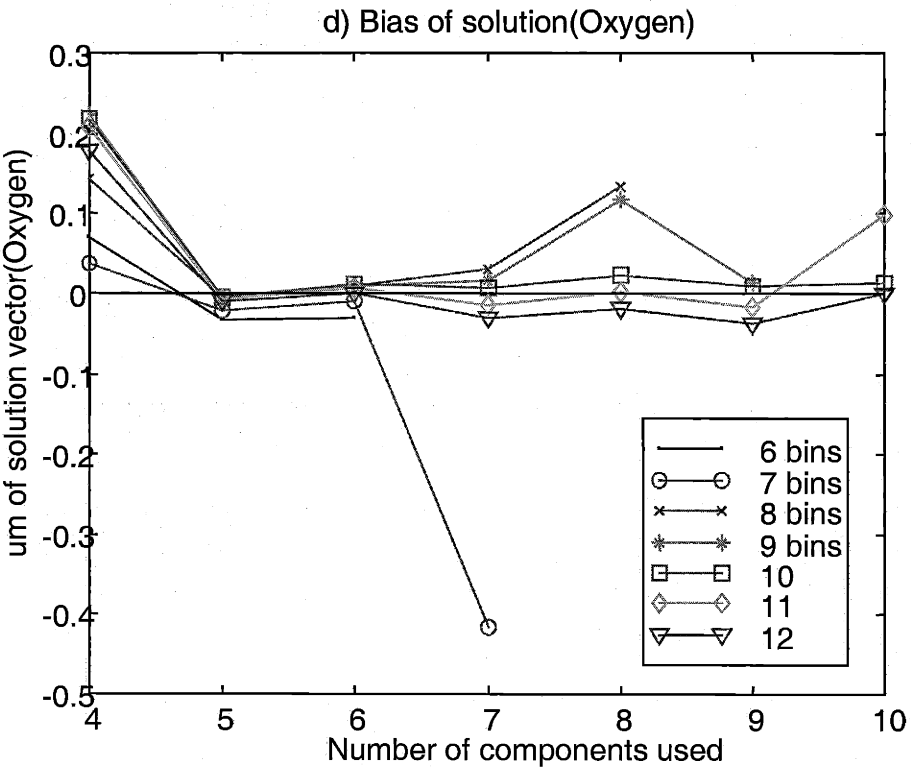
d) Bias of solution(Oxygen)
um of solution vector(Oxygen)
Number of components used
6 bins
7 bins
8 bins
9 bins
10
11
12

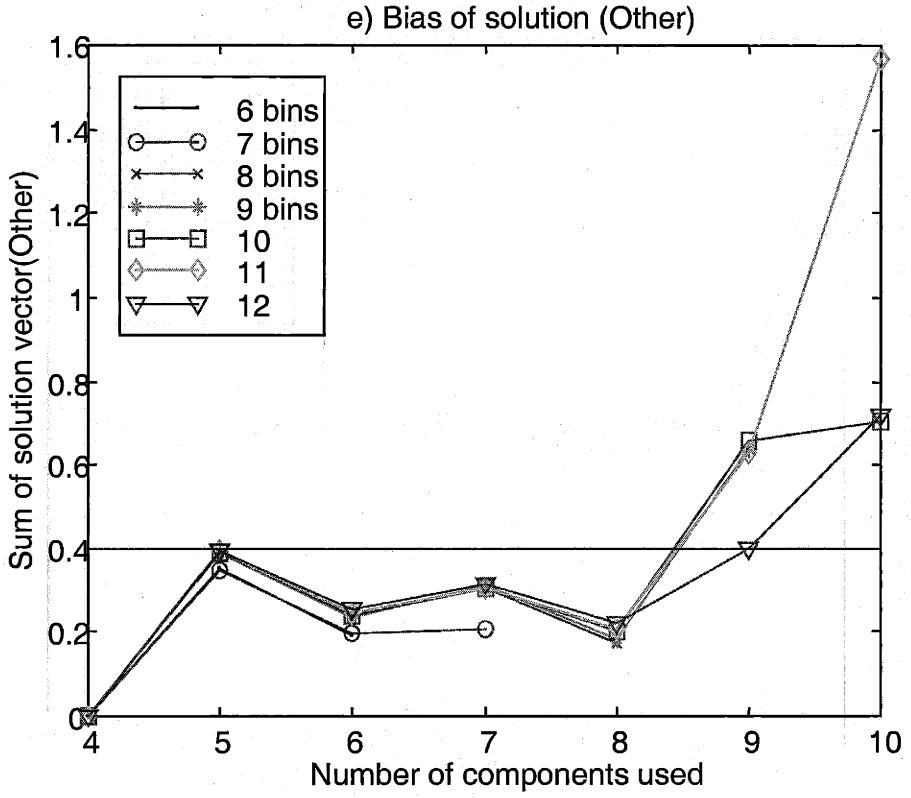

Figure 3.14 Bias of solutions for H, C, N, O, and sum of other elements

While the solution vector x_{LS} as a whole is generally unbiased, solutions for H, C, N, O, and Sum of other element are indeed biased in some situations. We draw the following conclusions from the figures:

1. The bias for individual elements is large when n=4. Four component modeling leads to large deviation when there is neutron scattering or gamma ray background, or other common elements.

2. The bias for individual elements increases when n>8. This is due to an increased singularity of the attenuation coefficient matrix A.

3. To reduce bias, we should include five to eight (5-8) components in our linear model, and the measurement (equation) number should be larger than the component number. (That is: $5 \leq n \leq 8$, and $m > n$.)

3.4.4 Relative Error

The analysis of stability and bias does not involve the measured total attenuation vector b. We only studied the properties of the content coefficient matrix C, which is derived from the attenuation coefficient matrix A. A more direct way to study stability and bias is to check the relative error of the solution for measured samples.

We use MCNP to simulate the measurement (of one pixel in NRR). The same geometry is used for simulating the measurement and obtaining attenuation coefficients. The "samples" are not actual materials, instead a specific elemental composition (number of atoms per square centimeter, #/cm^2) is assigned to each pseudo sample. Samples 1-5 only have H, C, N, O; samples 6-17 are randomly generated; samples 18-23 have reduced total content; and samples 24-29 have only one of the less interesting elements each. Table 3.4 lists the composition of these pseudo samples.

A five-constituent (H, C, N, O, Other) solution is calculated from $x_{LS} = Cb$, for various combinations of m and n. In the simulation, statistical error in the measurement vector b is typically 1-2%. (More constituents were used when calculating matrix C.)

After the five-constituent solution is obtained, three types of relative error are calculated. They are: Error3, the relative vector error of (C, N, O); Error4, the relative vector error of (H, C, N, O); and Error5, the relative vector error of (H, C, N, O, Other). We do this because the constituents (or elements) are not of equal importance to us. Regardless what each sample may consist of, its relative errors are defined as:

$$Error3 = \sqrt{\frac{(x_{LSC} - x_{tC})^2 + (x_{LSN} - x_{tN})^2 + (x_{LSO} - x_{tO})^2}{(x_{LSC})^2 + (x_{LSN})^2 + (x_{LSO})^2}} \tag{3.25}$$

$$Error4 = \sqrt{\frac{(x_{LSH} - x_{tH})^2 + (x_{LSC} - x_{tC})^2 + (x_{LSN} - x_{tN})^2 + (x_{LSO} - x_{tO})^2}{(x_{LSH})^2 + (x_{LSC})^2 + (x_{LSN})^2 + (x_{LSO})^2}} \tag{3.26}$$

$$Error5 = \sqrt{\frac{(x_{LSH} - x_{tH})^2 + (x_{LSC} - x_{tC})^2 + (x_{LSN} - x_{tN})^2 + (x_{LSO} - x_{tO})^2 + (x_{LSOther} - x_{tOther})^2}{(x_{LSH})^2 + (x_{LSC})^2 + (x_{LSN})^2 + (x_{LSO})^2 + (x_{LSOther})^2}} \tag{3.27}$$

Table 3.4 Composition of pseudo samples (unit: 10^{24} #/cm^2)

No.	H	C	N	O	Al	Si	P	S	Cl	Fe
1	0.25	0.25	0.25	0.25	0.0	0.0	0.0	0.0	0.0	0.0
2	0.1	0.2	0.3	0.4	0.0	0.0	0.0	0.0	0.0	0.0
3	0.4	0.1	0.2	0.3	0.0	0.0	0.0	0.0	0.0	0.0
4	0.3	0.4	0.1	0.2	0.0	0.0	0.0	0.0	0.0	0.0
5	0.2	0.3	0.4	0.1	0.0	0.0	0.0	0.0	0.0	0.0
6	0.0	0.1	0.3	0.2	0.1	0.0	0.0	0.1	0.0	0.2
7	0.3	0.0	0.1	0.0	0.2	0.1	0.1	0.0	0.1	0.1
8	0.1	0.4	0.0	0.1	0.0	0.1	0.0	0.0	0.3	0.0
9	0.2	0.2	0.1	0.0	0.0	0.2	0.0	0.1	0.2	0.0
10	0.3	0.1	0.0	0.2	0.0	0.1	0.1	0.1	0.1	0.0
11	0.2	0.1	0.1	0.0	0.1	0.1	0.1	0.1	0.1	0.1
12	0.0	0.0	0.0	0.5	0.0	0.1	0.0	0.0	0.3	0.1
13	0.1	0.0	0.5	0.2	0.0	0.0	0.0	0.0	0.2	0.0
14	0.1	0.5	0.1	0.0	0.2	0.0	0.1	0.0	0.0	0.0
15	0.5	0.0	0.2	0.1	0.1	0.0	0.1	0.0	0.0	0.0
16	0.0	0.4	0.0	0.0	0.1	0.1	0.2	0.0	0.1	0.1
17	0.1	0.1	0.3	0.2	0.0	0.0	0.0	0.2	0.1	0.0
18	0.1	0.1	0.2	0.2	0.1	0.1	0.0	0.0	0.0	0.0
19	0.1	0.0	0.1	0.1	0.0	0.1	0.1	0.1	0.1	0.0
20	0.1	0.1	0.1	0.1	0.0	0.0	0.0	0.0	0.1	0.1
21	0.0	0.2	0.0	0.1	0.0	0.1	0.0	0.0	0.0	0.1
22	0.1	0.1	0.0	0.1	0.0	0.1	0.0	0.0	0.0	0.0
23	0.0	0.2	0.0	0.0	0.0	0.0	0.0	0.0	0.1	0.0
24	0.2	0.2	0.2	0.2	0.2	0.0	0.0	0.0	0.0	0.0
25	0.2	0.2	0.2	0.2	0.0	0.2	0.0	0.0	0.0	0.0
26	0.2	0.2	0.2	0.2	0.0	0.0	0.2	0.0	0.0	0.0
27	0.2	0.2	0.2	0.2	0.0	0.0	0.0	0.2	0.0	0.0
28	0.2	0.2	0.2	0.2	0.0	0.0	0.0	0.0	0.2	0.0
29	0.2	0.2	0.2	0.2	0.0	0.0	0.0	0.0	0.0	0.2

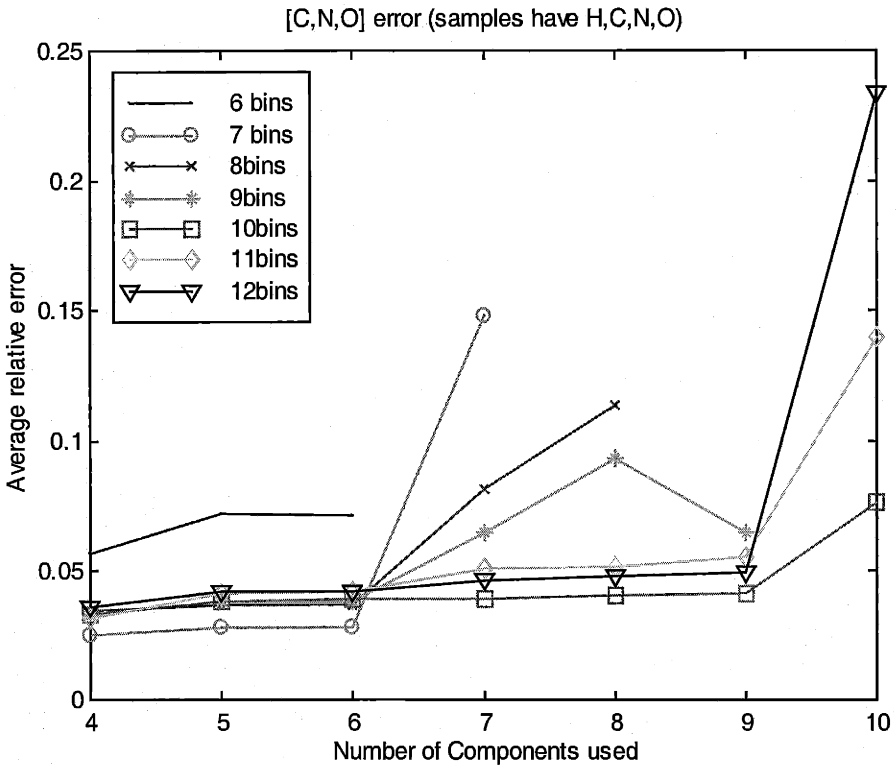

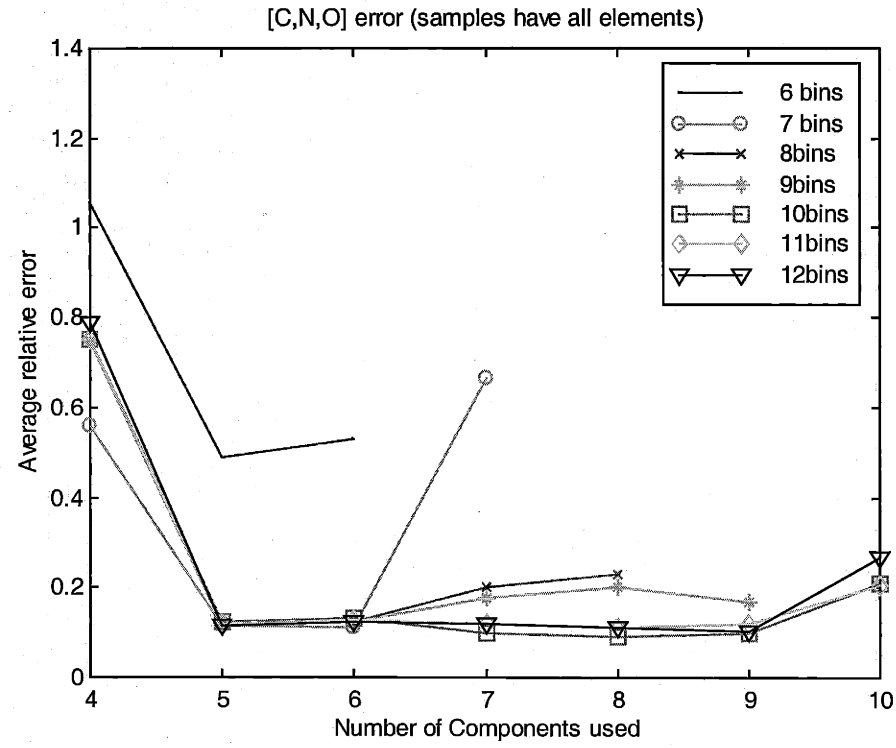

Figure 3.15 (C, N, O) error for various combinations of m and n.

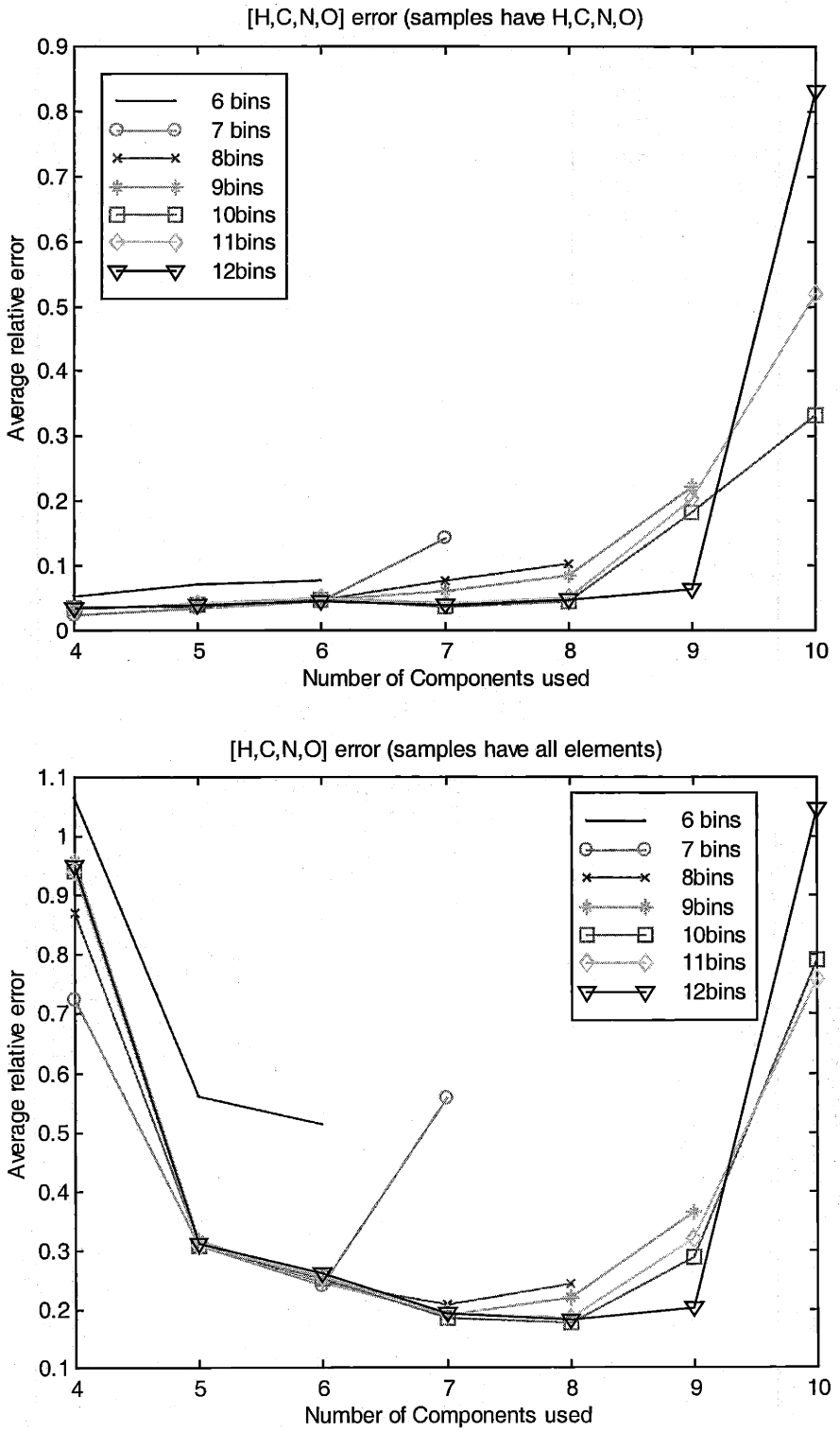

Figure 3.16 (H, C, N, O) error for various combinations of m and n.

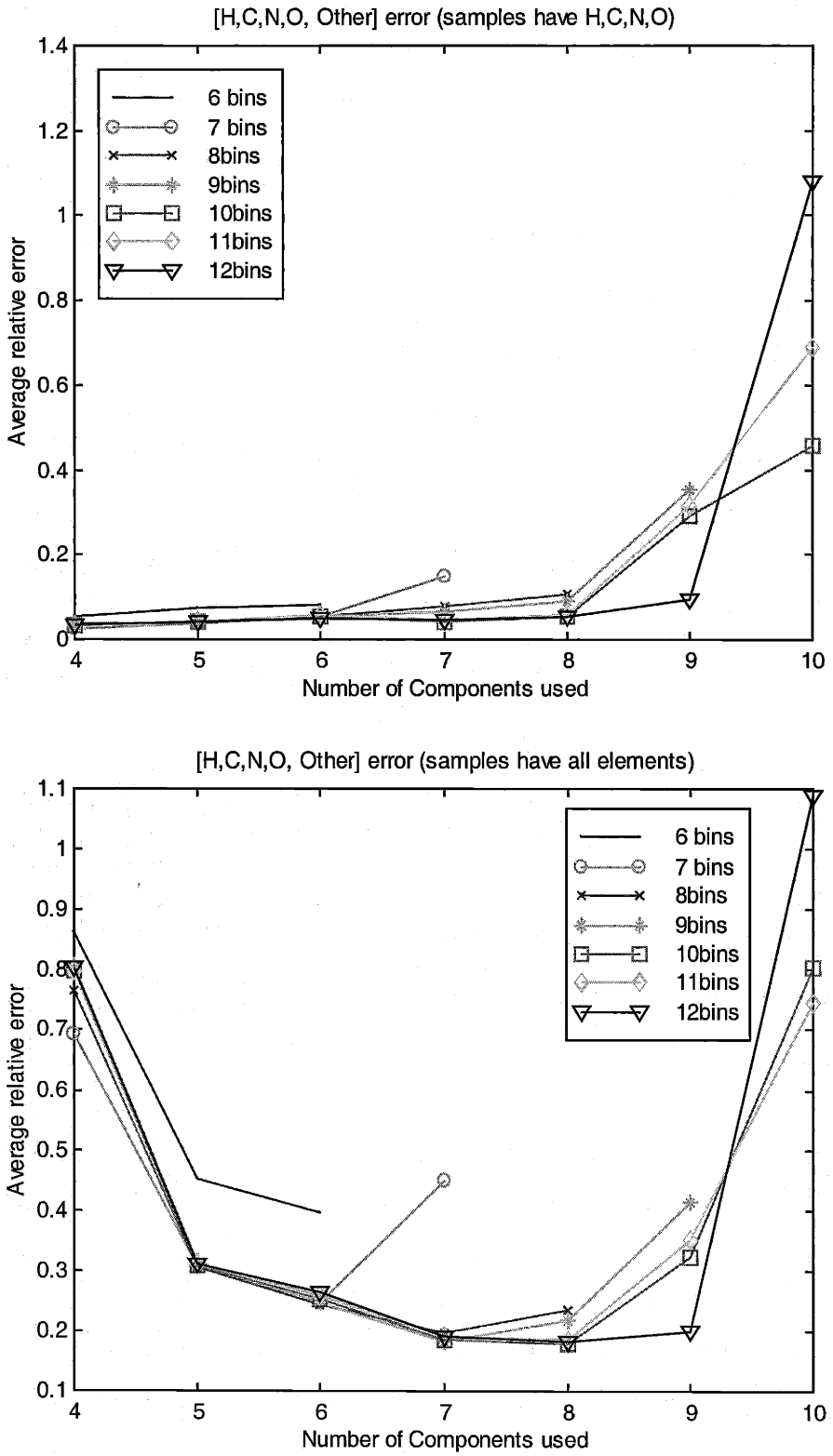

Figure 3.17 (H, C, N, O, Other) error for various combinations of m and n.

Each type of error is analyzed both for samples with all elements and for samples that have only H, C, N, and O. Figures 3.15, 3.16, and 3.17 plot (C, N, O) error (or Error3), (H, C, N, O) error (or Error4), and (H, N, O, N, Other) error (or Error5), respectively, for samples without less interesting elements and samples with all elements.

The behavior of the relative error is consistent with the previous analysis of stability and bias. The conclusions are listed below (For all cases, $m \geq n$).

1. If $m = n$, there is no data redundancy and errors increase greatly.
2. When $m = 6$, the error is significantly larger than the error when $m > 6$. This may be because six energy bins do not contain sufficient resonance features of H, C, N, and O.
3. If the samples have only H, C, N and O, four components ($n = 4$) best describe the system and give the best solution. That is, the error of (C, N, O), the error of (H, C, N, O), and the error of (H, C, N, O, Other) are all minimized at n = 4. When n increases, the solution deteriorates gradually for samples with only H, C, N and O. Since these samples only have the four most important elements, 4 components best model the system. Any additional components in the model only serve as an additional error source.
4. If the samples have all elements (H, C, N, O, and some elements of less importance), $n = 4$ leads to a large error. The system is poorly represented by only 4 components. When n increases from 5 to 9, the (C, N, O) error does not change much, but the (H, C, N, O) error and the (H, C, N, O, Other) error decrease first and increase thereafter, with a minimum at $n = 7$. The overall error at $n = 5$ is larger than n = 6 or $n = 7$ only because the errors on hydrogen and sum of other elements are larger at $n = 5$. Increasing n from 5 to 7 does not decrease the errors of C, N, and O, it only decreases the errors of hydrogen and sum of other elements.

Most system we investigate will contain H, C, N, and O, and C, N, and O are the critical measurements. Five components and seven to nine energy bins (equations) may be a good choice. In this arrangement ($m = 7\text{-}9$, and $n = 5$), we use the attenuation coefficients of Fe to describe all of the unimportant elements (Al, Si, P, S, Cl, Fe). When there are only H, C, N, O, the relative error is ~5%. When all elements mentioned above are present, the overall relative error is ~30% and the relative error of (C, N, O) is ~10%. The highest energy bin should cover the nitrogen valley at 4.75-5 MeV and the lowest energy bin should cover the oxygen valley at 2.25-2.5 MeV.

3.4.5 Measurement Error

In general, when measurement error decreases, we expect a more precise solution. This is true if the measurement is the major error source. In the previous analysis, the measurement error on vector b is about 1-2% and matrix A is obtained with higher accuracy. This measurement error (together with the modeling error) leads to ~5% solution error when only H, C, N, and O are present. To decrease measurement error means more detected neutrons and can be very expensive. The measurement error should be controlled to a "reasonable" level.

We simulated a series of measurements on pseudo sample No.1. The average measurement errors range between 0.5% and 15%. Using five components (n = 5) and seven energy bins (m = 7) in the model, we find that the resulting solution errors range between 5% and 25%. When measurement error decreases from 1.5% to 0.5%, the solution error does not change much (see Figure 3.18.) This may be due to modeling error and indicates the limit of the effectiveness of more precise measurements.

We have studied how to optimize the NRR method. The basic tradeoff is that we want a more precise and accurate solution from fewer and shorter-time measurements. It was found that using seven components (n = 7) minimizes the overall solution error, while using five components (n = 5) is the best choice for minimizing (C, N, O) error. The number of energy bins should be at least seven ($m \geq 7$) to contain important resonance features. Finally, the measurement error should be 1-2%, which leads to ~5% solution error (vector) if the material only contains hydrogen, carbon, nitrogen, and oxygen. Nitrogen content is generally lower than H, C and O in most ordinary goods (the subject of luggage inspection). Special attention should be given to nitrogen in further research.

As long as each energy bin contains some resonance feature, the linear model introduces no restriction on how to select the energy bins (width or spacing). nor is there a restriction on the distribution of source neutrons within each bin. There is no limitation

on how many elements could be present. The conclusion is not restricted to the 12 equally spaced energy bins and the 12 elements mention above either.

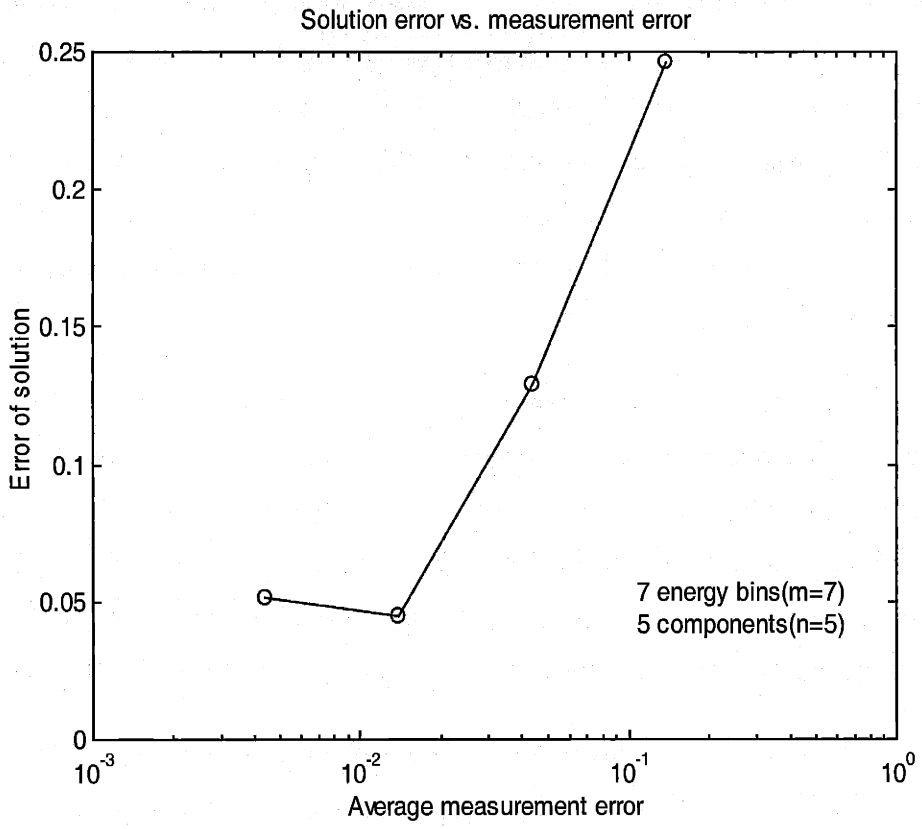

Figure 3.18 Relation between solution error and measurement error.

Chapter 4

Fast Neutron Resonance Radiography for Security Applications

The NRR principle as described in the last chapter can be used in drugs and explosives detection. The 2-D elemental maps of hydrogen, carbon, nitrogen, oxygen and the sum of other elements are calculated from fast neutron radiographic images, taken at different neutron energies that are chosen to cover resonance features of one or more elements. Limited 3-D information is possible from image and topology analysis. Drugs and explosives can be identified by their characteristic elemental composition. Different energy (2-6 MeV) neutrons are obtained at different angles from the DD reaction and a compact fixed energy RFQ with thick target can be used as the neutron source.

4.1 Variable Energy Neutron Source

For the (H, C, N, O, other) system, neutron energy should vary from as high as 4.75 MeV-5 MeV to cover the broad valley of nitrogen to as low as 2.25 MeV-2.5 MeV to cover the valley of oxygen. A series of different energy neutrons are needed to form an over-determined linear equation set. This requirement is fulfilled with neutrons from different angles of a DD neutron source, which employs a compact RFQ accelerator running at fixed deuteron energy.

4.1.1 D-D Angular Distribution

The DD nuclear reaction

$$^2H + ^2H = ^3He + n + 3.27\,MeV \tag{2.5}$$

has a Q-value of 3.27 MeV, which is comparable to the bombarding deuteron energy. Thus the resulting neutron energy has a large range. (In DT reaction, Q-value is 14.6MeV while bombarding deuteron energy is only about 0.1 MeV, and the resulting neutron energy is almost the same (14 MeV) at all angles.) The neutron energy from the DD reaction falls off rapidly with angle, as shown in figure 2.5. A DD neutron source is a poor choice as a mono-energetic source for radiography.

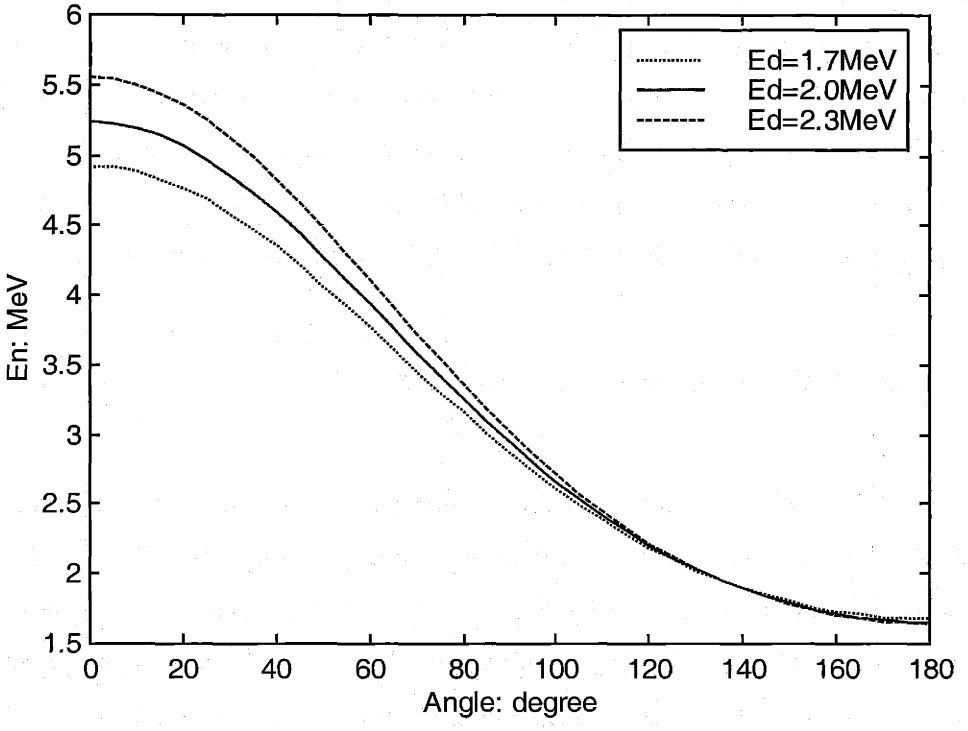

Figure 4.1 DD neutron energy as a function of angle

Figure 4.1 gives the angular dependence of DD neutron energy. When Ed=1.7-2.3 MeV, neutron energy falls off from 4.92-5.55 MeV at 0° to 2.28-2.33 MeV at 115°, which meets our requirement for the neutron source. At angles smaller than 90°, neutron

energy is significantly dependent on deuteron energy. Since the target (deuteron) has some thickness, the projectile (d^+) might lose some energy before generating a neutron. As a result, neutron energy at any angle has a spectrum, which is broad at small angles and narrow at 100^o or more. If the incident deuteron energy is 2.3 MeV and target thickness is 0.6 MeV, the generated neutrons have energies ranging from 4.92 MeV to 5.55 MeV at 0^o.

The object under inspection always has finite size, therefore different parts of the object are generally at a different angle and subject to neutrons of different energy. That is, neutrons have an energy spectrum at each pixel of the image, and the spectrum varies across the image.

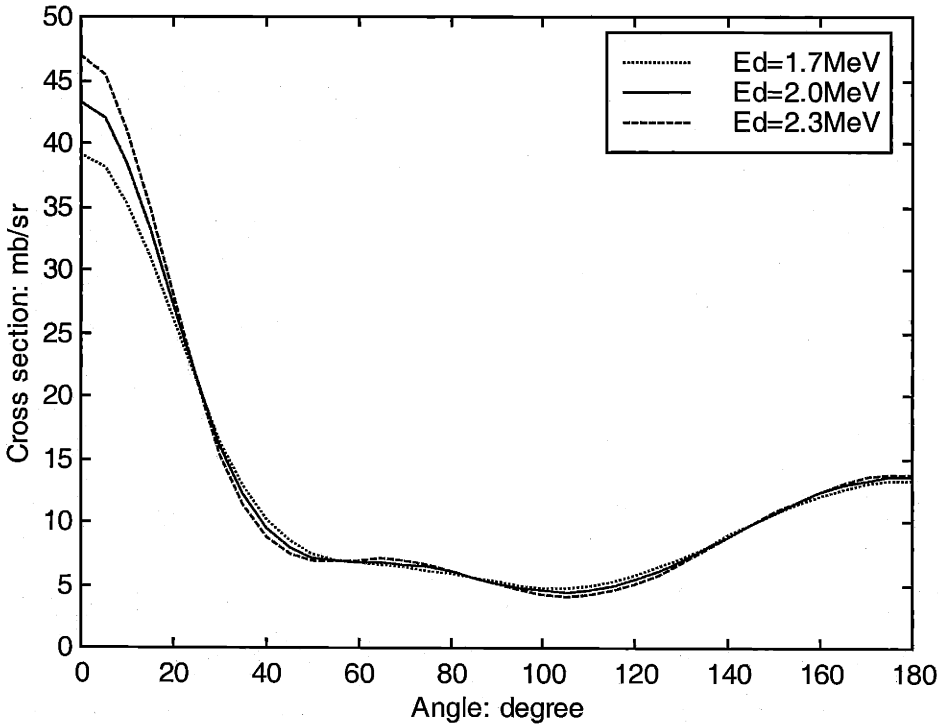

Figure 4.2 DD differential cross section as a function of angle

Neutron energy depends on deuteron energy, and a thick target leads to a neutron spectrum at each angle. Neutron energy is angularly dependent, therefore the neutron spectrum varies across the image. However, the neutron spectra are roughly flat at all angles. Figure 4.2 gives the differential cross section of a DD neutron source. The cross

section only changes slightly with deuteron energy at angles greater than 40°. Since dE/dx (and therefore dx/dE) of the deuteron changes very little over its energy range in the target, the resulting neutron energy spectrum is essentially flat at any angle.

4.1.2 Rotational Geometry

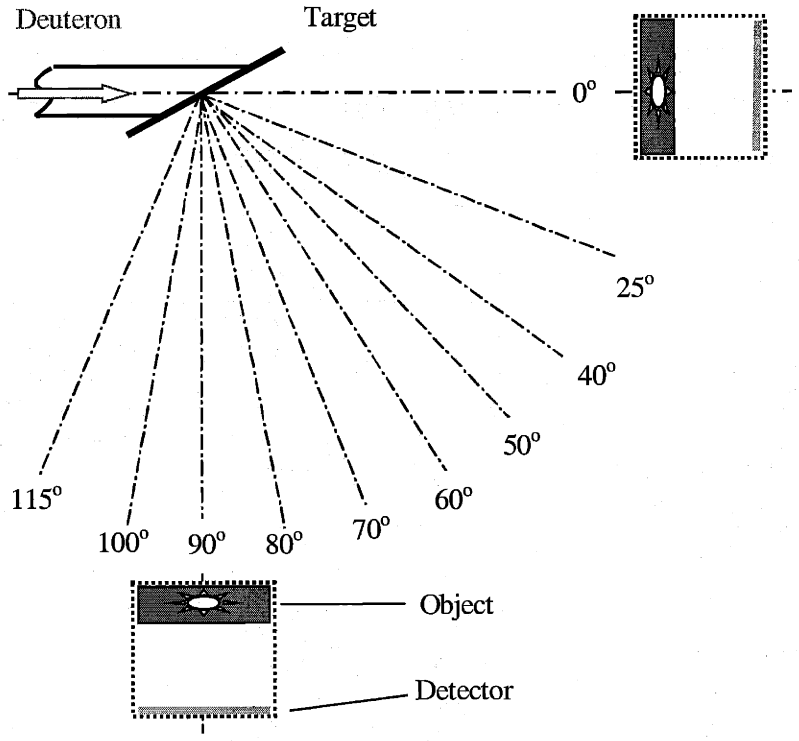

Figure 4.3 Rotational geometry

When deuterons of fixed energy bombard a deuteron target, neutrons at different angles have different energy. We can rotate the object-detector assembly around the neutron source to fulfill the requirement for neutron resonance radiography. The object stays for an exposure period at each nominal angle and then moves on to the next one. When enough (8-10) images have been taken, the resulting over-determined linear equation set for each pixel can be solved for elemental mapping of hydrogen, carbon, nitrogen, oxygen and sum of other elements. Since neutron energy varies across the image, different attenuation coefficients are used for different pixels.

Although moving the object in a straight line also leads to different energy neutrons, it is very important to be aware that translational geometry does not work. A radiographic image is a 2-D projection of the object and a linear equation set describes the measured total attenuation of one pixel in the images. That is, a pixel in all 8-10 images must correspond to the same projection line in the object. Since both the object and the detector are thick in practice, translational geometry violates the basis of our linear model, (see figures 2.14 & 2.15).

The rotational geometry is different from that in tomography. In the latter, the source and detector are aligned and the object rotates around a fixed axis, or the aligned source-detector assembly rotates around the object. The purpose of rotation in tomography is to obtain different projections. While in NRR, we want the projections to be exactly the same, but with different energy neutrons.

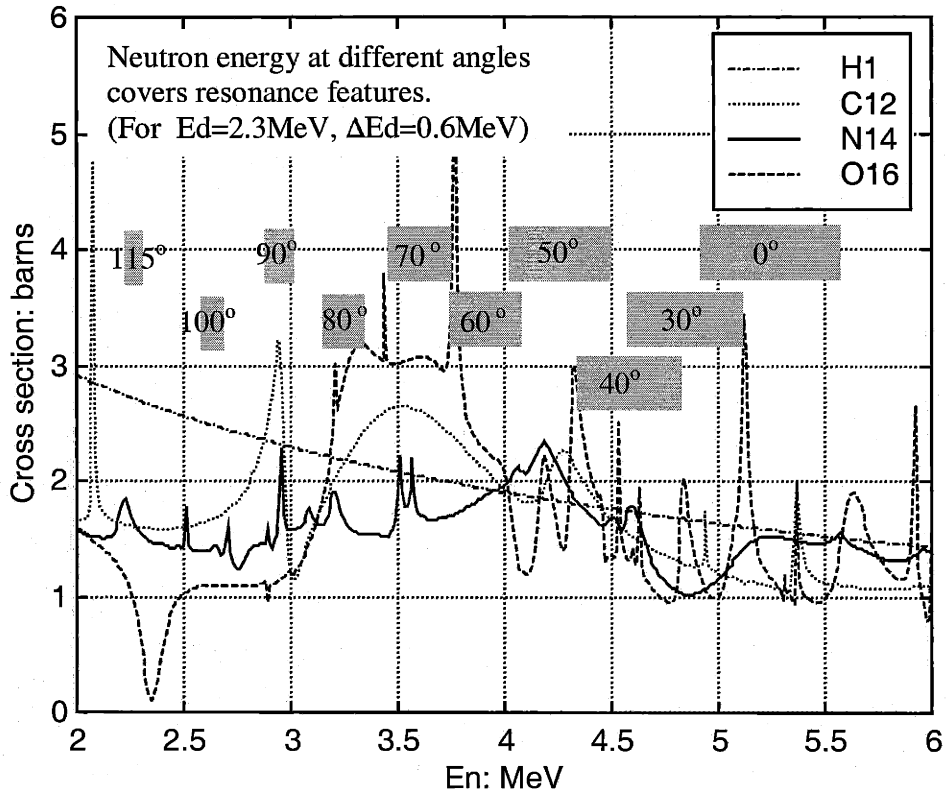

Figure 4.4 Neutron energy at different angles

Figure 4.4 shows neutron energies obtained at different angles. In the figure, it is assumed that Ed=2.3 MeV and ΔEd=0.6 MeV.

It is important to emphasize that different parts of the object are projected at different angles. In other words, the angle changes across the image. When one part of the object is at a certain angle so that the neutron energy matches a resonance peak perfectly, other parts are not. It is not possible to do single peak resonance radiography. In addition, since only some part of the object is imaged with the desired energy neutrons, redundancy in data (more images) is required for solving the linear equation set for each pixel. Attenuation coefficients for hydrogen, carbon, nitrogen, oxygen and other elements can be measured experimentally at these angles, under the same geometric conditions as the object will be inspected.

4.2 Deuteron Target

Fast neutrons for resonance radiography are generated by bombarding a deuteron target with energetic deuterons accelerated by an RFQ linac. The target could be in any form as long as it contains the required deuterons—D_2 gas or deuterated material [28].

4.2.1 Gas Cell

A gas cell is usually a cylindrical container with a thin entrance window at one end. The other end is closed and serves as a beam stop. D_2 gas inside the cell is the target that produces fast neutrons. The entrance window separates the D_2 gas from the d^+ particle path, which is in vacuum.

D_2 Gas

A d^+ beam loses energy when traveling in D_2 gas. That is, deuterons have different energies when they react with the target gas. As a result, the generated neutrons have an energy spread at all angles. The deuteron dE/dx can be calculated from Bethe's formula:

$$-\frac{dE}{dx}=\frac{4\pi e^4 z^2}{m_0 v^2}\cdot NZ\cdot[\ln\frac{2m_0v^2}{I}-\ln(1-\frac{v^2}{c^2})-\frac{v^2}{c^2}] \tag{4.1}$$

Figure 4.5 gives the calculated dE/dx for 3 atm D_2 Gas. Energy loss is about 0.2 MeV/cm at deuteron energy of around 2 MeV. Neutrons at 0^o have about the same energy spread as deuteron energy spread in the target. Since neutron energy spectrum doesn't need to fit single resonance peaks, the target can be as thick as 0.8 MeV, or 12 cm-atm.

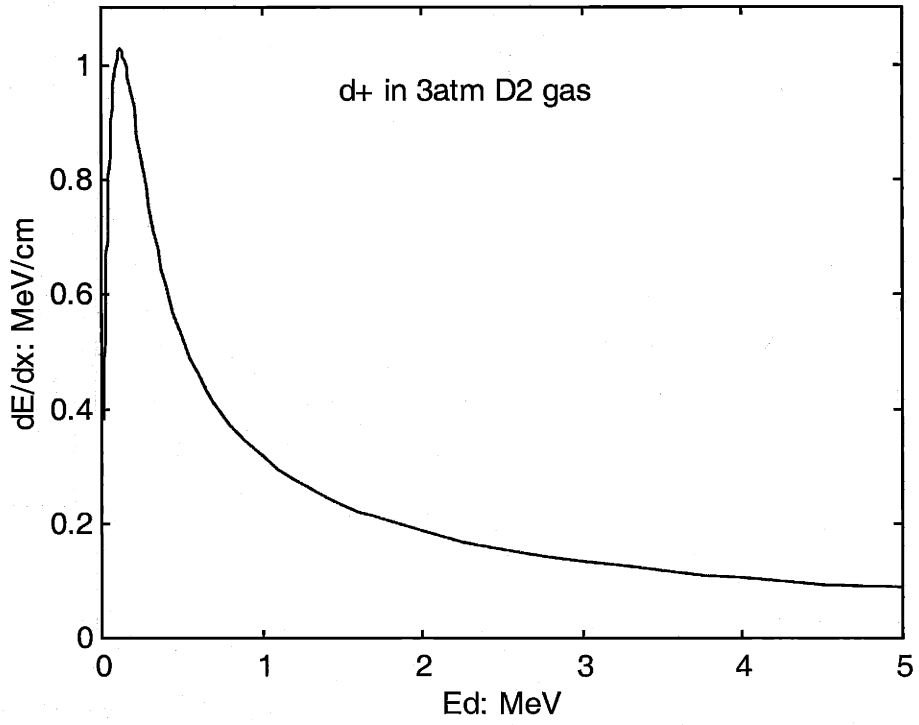

Figure 4.5 d^+ energy loss in 3 atm D_2 gas

Lateral straggling is the transverse deviation from its original direction. This leads to a larger source dimension than the accelerated beam spot size and deteriorates the overall spatial resolution. When a 2 MeV deuteron travels through 2 cm of D_2 gas (3 atm), the lateral straggling is only a fraction of a millimeter.

Neutron yield Y is determined by the DD reaction cross section, deuteron beam current and D_2 target thickness. Figure 4.6 shows the total and 0^o cross sections.

$$Y = \frac{I}{1.6x10^{-13}} \cdot \sigma \cdot 10^{-27} \cdot n \cdot x \tag{4.2}$$

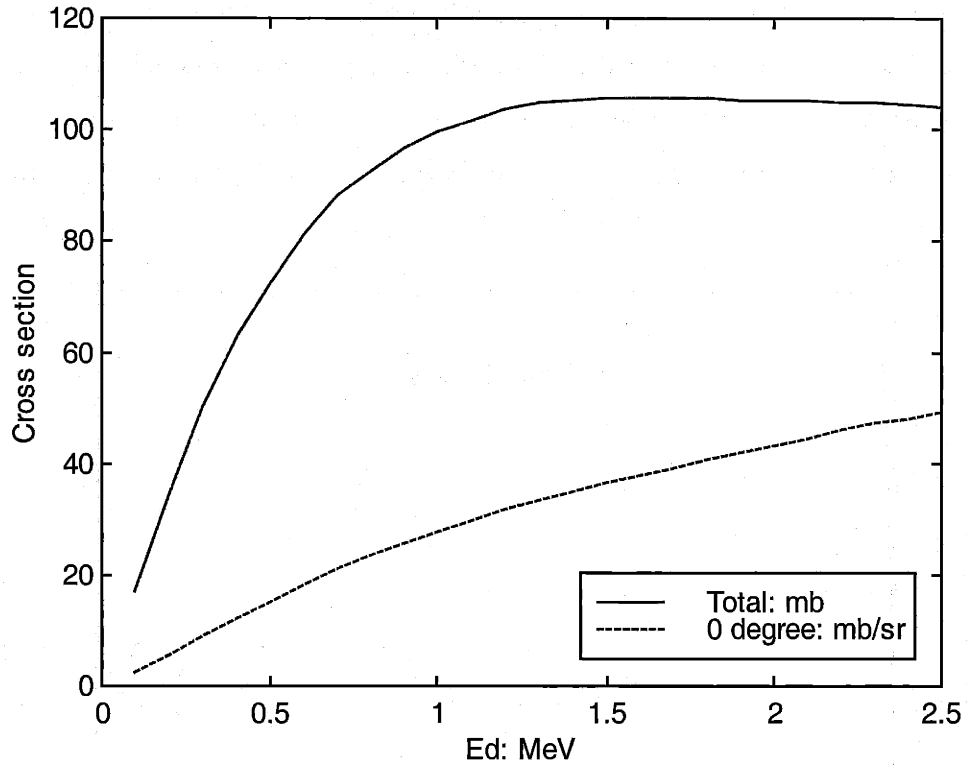

Figure 4.6 Total and 0° DD cross section

Beam current I is in μA and reaction cross section σ is in *mb* or *mb/sr*. Atomic density n of a 3 atm D_2 gas is $1.6x10^{20}$ #/cm^3. The total neutron yield (Ed=2.3 MeV, x=2 cm and ΔEd=0.4 MeV) is ~$2.0x10^8$ neutrons/sec/μA. The differential yield is ~$9.0x10^7$ neutrons/sec/sr/μA at 0° and ~$1.0x10^7$ neutrons/sec/sr/μA at 90°.

The DD neutron source itself is not contaminated. There is no gamma ray background or second group neutron at our low deuteron energy.

Entrance Window

The entrance window must be thin to minimize deuteron energy loss and energy straggling. It must also be strong enough to sustain a pressure difference of several

atmospheres. It must withstand heat delivered by the particle beam and should have low neutron and gamma ray yield, if any. Commonly used window materials are listed in Table 4.1.

Table 4.1 Properties of window materials

Material	Density g/cm^3	Melting Point °C	20°C Tensile Strength: MPa	Thermal Cond. W/m/K
Havar	8.3	--	1860	14.7
Si_3N_4	3.2	1800	570	27
Tungsten	19.4	3410	1000-1800	182
Molybdenum	10.2	2617	850-1400	139
Nickel	8.9	1453	~400	94

Accelerated d^+ loses part of its energy in the entrance window. This energy loss can be compensated by raising the accelerator energy. Energy straggling is negligible considering that a thick D_2 target is used. However, heat deposited in the window is a serious problem. Figure 4.7 shows deuteron energy loss in 1 μm thick materials. Heat deposited is the product of dE/dx, window thickness and beam current.

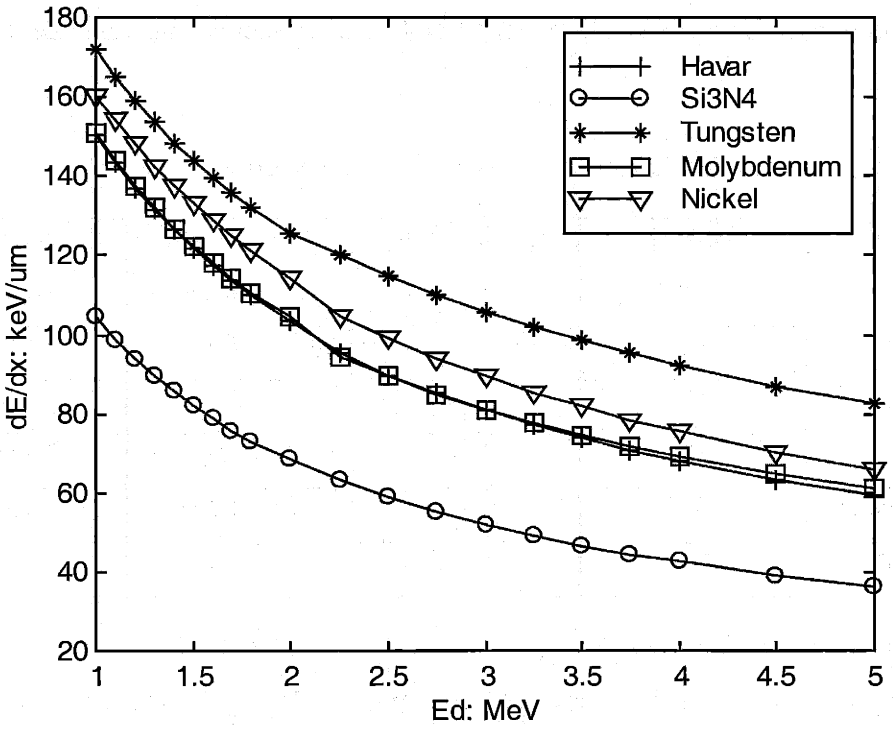

Figure 4.7 Deuteron energy loss in window materials

Heat Removal

A 10 μA beam (Ed=2.3 MeV when enters Gas chamber) delivers ~3 W of power to a 5 μm Si_3N_4 window (dE/dx~60 keV/μm), or ~5.5 W of power to 5 μm tungsten window (dE/dx~110 keV/μm). In addition, the beam delivers ~4 W of power to the 3 atm, 2 cm thick D_2 gas (d^+ losses 0.4 MeV energy in gas) and ~19 W of power to the beam stop.

While heat on the beam stop (rear end of gas cell) can be removed with exterior cooling (usually an air jet or a turbulent water film), it is difficult to apply active cooling to the entrance window. Heat deposited in the window material is dissipated in the following ways: (1) radial thermal conduction; (2) radiation from both surfaces; (3) D_2 gas convection. Let us first consider window heat removal without gas circulation.

(i) Conduction

If only conduction is important, the radial conduction equations are:

$$\frac{dT}{dr} = -\frac{P}{2\pi rtk}; \qquad R1 \le r \le R2 \tag{4.3}$$

$$\frac{d}{dr}(r\frac{dT}{dr}) = -\frac{P}{\pi R1^2}\cdot\frac{r}{kt}; \qquad r \le R1 \tag{4.4}$$

In the equations, T is local temperature and $R1$, $R2$ and t are radius of beam area, radius of window and thickness respectively. k is thermal conductivity. The power P is treated as uniformly distributed in the beam area of radius $R1$. Boundary conditions are: $T=T0$ at $r=R2$; and $dT/dr=0$ at $r=0$. $T0$ is environment temperature (soft solder or compressing the foil between O-rings).

The highest temperature is at the center (r=0) and the value is:

$$T_{\max} = \frac{P}{4\pi kt}(1 + 2\ln\frac{R2}{R1}) + T0 \tag{4.5}$$

When a 10 μA beam passes through a 5 μm tungsten foil (R1=0.5 cm; R2=0.75 cm), temperature at the center is ~900°C (for T0 at room temperature).

(ii) Radiation

If only radiation is important, the radiated power at two surfaces is:

$$P = 2\pi R1^2 \cdot \varepsilon \cdot \sigma T^4 \tag{4.6}$$

The emitance ϵ is 0.03-0.1 for metal foils and about 0.85 for Si_3N_4. When a 10 μA beam travel through a 5 μm Si_3N_4 (R1=0.5 cm), its maximum temperature is ~550°C.

(iii) Convection

The convection equation is $P = h \cdot \pi R1^2 \cdot (T_H - T_L)$. If the target chamber is an enclosure of 0.75 cm radius and 2 cm length, only natural convection exists and the heat

transfer coefficient h is not significant enough to consider for window heat removal. In addition, the power delivered to D_2 gas will significantly increase the gas temperature and thus the pressure, increasing window strength requirement.

Material tensile strength drops with increasing temperature. We conclude that using a Si_3N_4 window and circulating D_2 gas through a cooling system is preferable for a 10 μA or higher beam current. the D_2 gas is returned through a jet aimed at the center of the entrance window. An additional nice feature of Si_3N_4 is that it can be made stress free. This is generally not true for metal foils.

4.2.2 Windowless Gas Target

An improvement to the simple gas cell target is using a plasma porthole to separate the high-pressure gas in the target chamber and vacuum beam path [29 & 30]. Figure 4.8 shows a closed loop windowless gas target. Because a low density plasma blocks gas flow, accelerated d^+ particles pass through the porthole (from the right in the figure) with very small energy loss, but very little D_2 gas leaks (from the left in the figure) into the vacuum beam path. Any D_2 gas that does leak through is pumped out of the beam duct to maintain the vacuum and a condenser re-circulates it back into the target chamber to maintain the gas pressure.

A gas pressure of 6 atm in the target chamber is achievable while 10^{-6} mbar vacuum is maintained for the beam path. Since there is no longer a window heating problem, high beam currents (100 μA or more) can be applied. Higher gas pressure also reduces lateral straggling of the projectile (d+), leading to a smaller neutron source dimension.

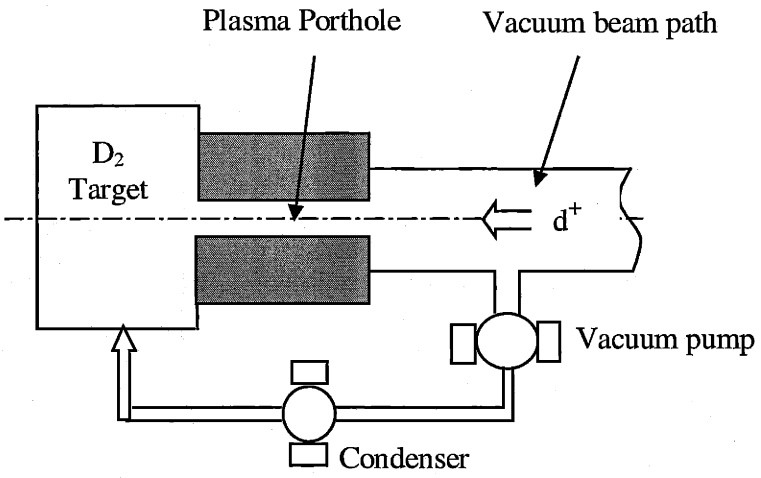

Figure 4.8 A closed loop windowless gas target

Plasma Porthole

The plasma porthole is a stable plasma arc used as a high-pressure gas-vacuum interface. The device consists of cooled copper discs sandwiched between boron nitride disks with a hole in the center (beam path). At one end of the tube (the central hole) is a large anode plate; and at the other end (near the target chamber) are three cathodes, equally spaced in a circle. High voltage is applied to the cathodes causing an arc towards the anode. The boron nitride disks serve as electrical insulators and the alternating disk structure stabilizes the plasma discharge.

Gas temperature in the plasma porthole (the central hole, or beam path) is between 12000 K at the edge and 15000 K at center. This temperature is sufficiently low so that the plasma flow is dominated by intermolecular collisions and acts as a high temperature gas. The high temperature gas in the porthole has low density (1/40 that of the gas in target chamber) and is able to support a large pressure difference while being almost transparent to the accelerated beam. Gas leakage to the vacuum beam path is greatly reduced as compared with an ordinary hole of same diameter. (The leaked gas must be pumped out.)

The pressure difference that the plasma arc can support is determined by the flow rate of the plasma:

$$\frac{dp}{dx} = \frac{8 \cdot \mu}{\pi \cdot R^4} \cdot Q \tag{4.7}$$

where Q is the flow rate, μ is the viscosity and R the ideal gas constant. Viscosity is proportional to the square root of temperature. However, the temperature cannot be so high that intermolecular collisions become less of a factor and viscosity becomes proportional to temperature itself.

An additional benefit of the plasma porthole is that it has a focusing effect on the deuteron beam. When electric current flows in the plasma arc it creates a circular magnetic field around the center of the beam path, which focuses the beam. The plasma porthole is suitable for high beam current, small spot size applications.

4.2.3 Solid Target

It is advantageous to employ solid state targets because they can be directly mounted at the end of a vacuum beam path, with deuterated material bombarded by a deuteron beam. Isotopes of hydrogen are readily absorbed in titanium or zirconium to form metal hydrides. These metals are usually evaporated onto a metal backing. Titanium is the most commonly used occluding metal because it has the lowest stopping cross section of elements with a strong affinity for hydrogen and a high thermal conductivity.

Titanium tritide is widely used as DT accelerator targets and titanium deuteride is in general equally relevant. In fact, titanium deuteride has nicer properties: (1) Tritium is radioactive but deuterium is not and (2) titanium deuteride targets under deuteron bombardment give a uniform neutron yield with time, while titanium tritide targets often have a decreasing neutron yield.

A typical ratio of occluded deuteron atoms to titanium atoms is 1.5, and the evaporated titanium layer ranges from 0.2 to 4 mg/cm^2. When the incident deuteron

energy is 2.3 MeV, the calculated energy loss in a 4-5 mg/cm^2 titanium deuteride target is 0.6-0.8 MeV. (Equation 4.1.) Neutron yield can be calculated with equation 4.2.

Based on 5 mg/cm^2 TiD, a 1.5 atomic ratio and Ed=2.3 MeV:

$$n \cdot x = \frac{5\times10^{-3} g/cm^2 \times 6.022\times10^{23} \#/mol}{(1\times2+\frac{1}{1.5}\times48) g/mol} = 8.86\times10^{19} \#/cm^2$$

The resulting total neutron yield is 5.8x10^7 neutrons/sec/μA, or 2.5x10^7 neutrons/sec/sr/μA at 0^o and 2.8x10^6 neutrons/sec/sr/μA at 90^o. With the same neutron energy spread, neutron yield from a solid state target is about 1/8 that from a D_2 gas target. Lower neutron yield is the major drawback of a deuterated target.

Titanium deuteride breaks up at 250°C and therefore target cooling is required. The metal backing spreads the heat deposited by the deuteron beam and an air jet applied to the exterior can satisfactorily dissipate 50 Watts power. While copper is generally not recommended for a proton beam because of its neutron and gamma ray yield, it is suitable for a deuterated target backing. Deuteron energy is 1.5-1.7 MeV when entering the backing material and there is very little gamma ray contamination.

When heat deposited by the beam is removed reliably, the lifetime of a titanium deuteride target depends on maintaining clean vacuum conditions. Building up of surface contamination leads to a dead layer and affects the neutron energy.

4.3 NRR Simulation

A NRR simulation was performed. A series of radiographic images were simulated with different neutron spectra, as obtained from different angles of a DD neutron source. The attenuation coefficients were also simulated with these neutron spectra, for interesting elements like hydrogen, carbon, nitrogen and oxygen. A constant attenuation coefficient (2.5x10^{-24} cm^2) was used for the fifth component, which represents

all other elements. Elemental images were calculated for each pixel from the attenuation coefficients and radiographs, using the linear equations.

4.3.1 Configuration

Simulation Tools

The imaging simulation is based on Monte Carlo method of tracking individual particles and uses the radiation transport code "COG" developed at Lawrence Livermore National Laboratory (LLNL) [31]. COG is a detailed, high-resolution code designed to simulate coupled neutron, photon, and/or electron transport through arbitrary 3-D geometry. The code uses point-wise-correct interaction cross sections with exact angular scattering functions and provides users with a full range of statistical biasing options to speed up the simulation.

The problem geometry can be set up manually using combinations of complex, built-in pseudo-surfaces (*e.g.* boxes, spheres, cylinders, and cones) or developed offline using common CAD tools and then read directly into the code through the use of a built-in translator. COG allows users to score the results of a simulation using a number of standard built-in detector types (*e.g.* boundary crossing detectors, reaction detectors, point flux estimators, and pulse detectors) or specialized, "user-defined" detector packages linked into the code at run time (*e.g.* radiographic imaging detectors [32]).

Attenuation coefficients were simulated with MCNP(4B) code [33], with the same source specification and geometry. MCNP is also based on Monte Carlo but does not provide imaging simulation. The objects used in the simulation were slabs of pseudo materials (pure hydrogen, carbon, nitrogen or oxygen). In practice, these coefficients should be measured experimentally under the same geometry as set for object inspection.

Objects

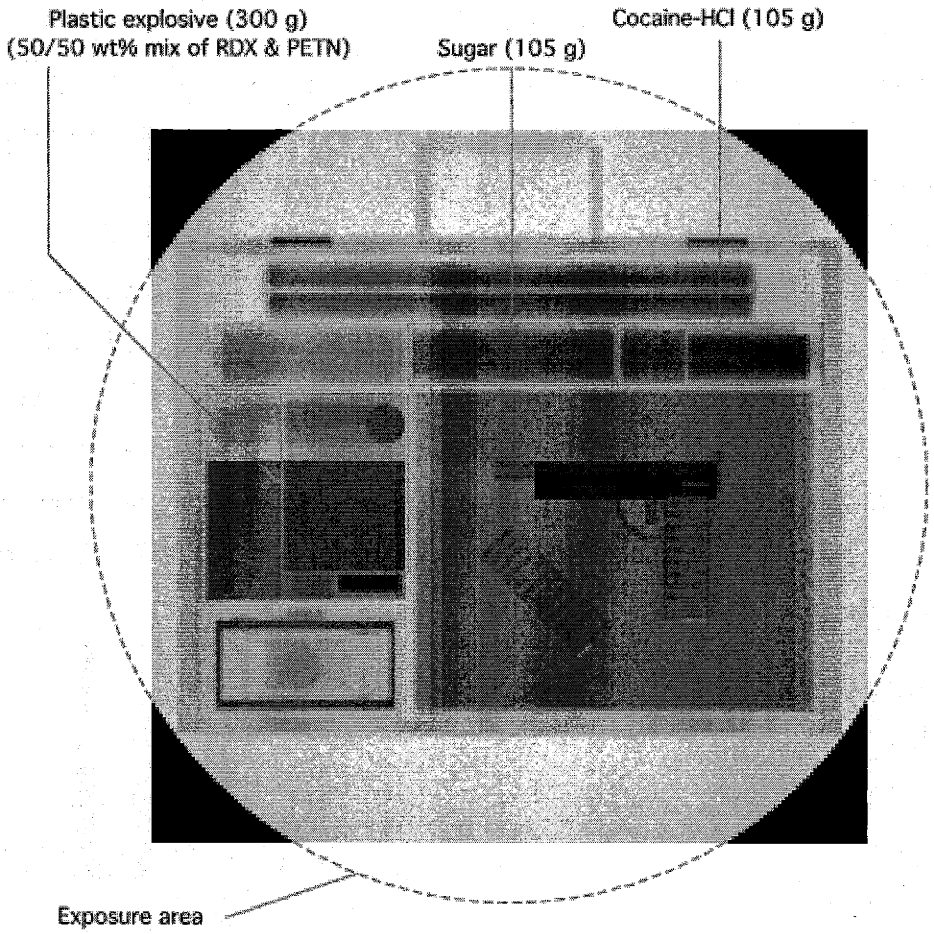

Figure 4.9 Terrorist Overnight Bag

The object modeled in the simulations is a "Terrorist Overnight Bag." The bag itself consists of a thin aluminum shell (≈ 40 x 30 x 10 cm^3) with a wood handle, thick cloth covering and steel fittings. It contains a newspaper, a bag of sugar (≈ 100 g), a stash of cocaine-HCl (≈ 100 g), a travel umbrella, a 4" switchblade knife, a paperback book (presumably the "*Anarchist's Handbook*"), a 300 g block of plastic explosive (50/50 wt.% mix of RDX and PETN), a pen and pencil set, a small camera, an automatic pistol with extra ammunition clip, a flat paper notebook and a selection of cotton, wool and nylon clothing items (see Figure 4.9). The bag is heavily loaded with an average density of ~0.5 g/cm^3.

Source and Geometry

The source-to-object and object-to-image distances used in the simulations were ~150 cm and ~50 cm, respectively, giving an imaging angle of ± 10° and a magnification factor of 1.33. The energy spectrum of the neutron source was adjusted downward from ~5.55 - 4.70 MeV to ~ 2.33 - 2.27 MeV in a series of 10 runs to simulate scanning the object through angles ranging from 0° to 115° relative to the axis of a real DD neutron source. Images of the direct (unscattered) neutron flux from the source and scattered neutrons in several bins at lower energies were generated using 200 x 200 pixel imaging detectors with appropriate energy and scattered-particle masks. In this simulation, neutron energy did not change across the image. The simulations were run with 500,000,000 test particles on the LLNL ASCI Blue Pacific supercomputer using 256 processors operating in parallel. For purposes of comparison, additional images of the bag were generated using a simulated 140 keV X-ray source.

4.3.2 NRR Results

Radiographs

Figure 4.10 shows a neutron radiograph at 0^{o} and a X-ray radiograph. Fast neutron radiographs were simulated at nominal angles of 0, 25, 40, 50, 60, 70, 80, 90, 100 and 115 degrees but the results are not all shown here. X-ray radiography was simulated at 140 keV.

X-ray attenuation coefficients depend upon the atomic number of the target material. Dark area in the X-ray radiograph means high density and/or metal components in the object. The most obvious features seen in the X-ray image are the pistol, bulletin heads, the knife blade and hinge, the battery and aluminum hinges. Other objects may be identified by their shapes. It is not possible to tell the plastic explosive sheet form the book or the bag of drug from sugar.

Fast neutron attenuation coefficients are related to the total neutron cross-sections over the energy spectrum of the source neutrons. Unlike X-ray attenuation, fast neutron

attenuation coefficients vary only moderately from energy to energy and from element to element. The difference is typically within a factor of 2 to 3 (Figure 4.4). As a result, the linear equation set is a "good" problem. In the neutron radiograph, the contrast is not as much as that in the X-ray radiograph. Objects may also be identified by their shapes. As in the X-ray image, there is not sufficient information to detect the plastic explosive sheet or drug bag.

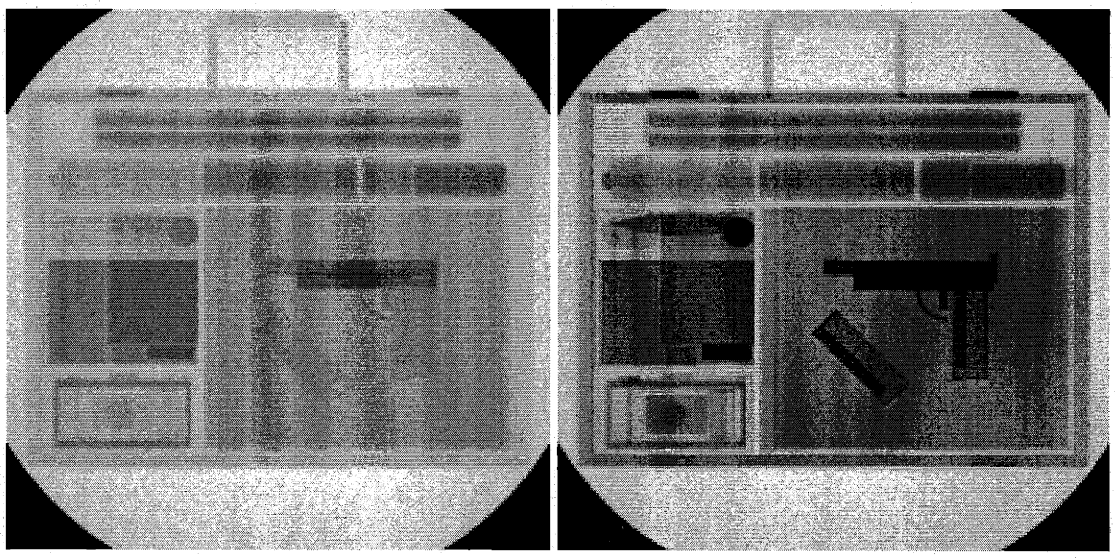

Figure 4.10 Fast neutron radiograph at 0^{o} (left) and X-ray radiograph.

Elemental Images

NRR is designed to calculate elemental images from a series of neutron radiographs. The calculated elemental mappings are given in Figures 4.11 and 4.12. The calculation uses five components: hydrogen, carbon, nitrogen, oxygen and a flat component representing all other elements and scattered neutron/gamma ray background. In this situation, the content of most elements other than hydrogen, carbon, nitrogen and oxygen is split between "hydrogen" and "other", because their attenuation profiles (vs. neutron energy) fall between that of hydrogen and the flat profile representing "other". Therefore a larger error is expected for hydrogen, especially when a lot of aluminum is present.

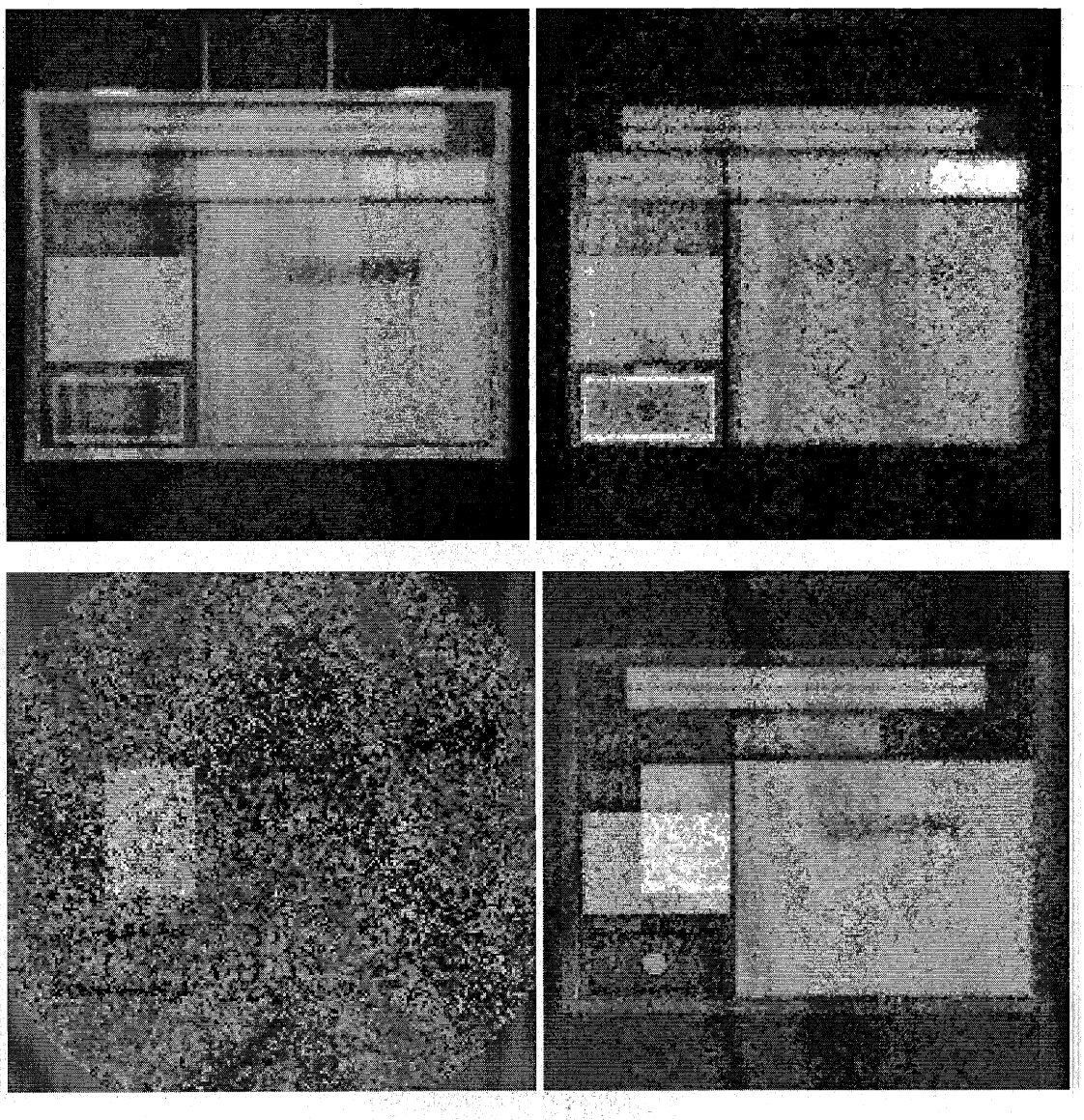

Figure 4.11 Calculated elemental images (Top left: hydrogen; top right: carbon; bottom left: nitrogen; bottom right: oxygen)

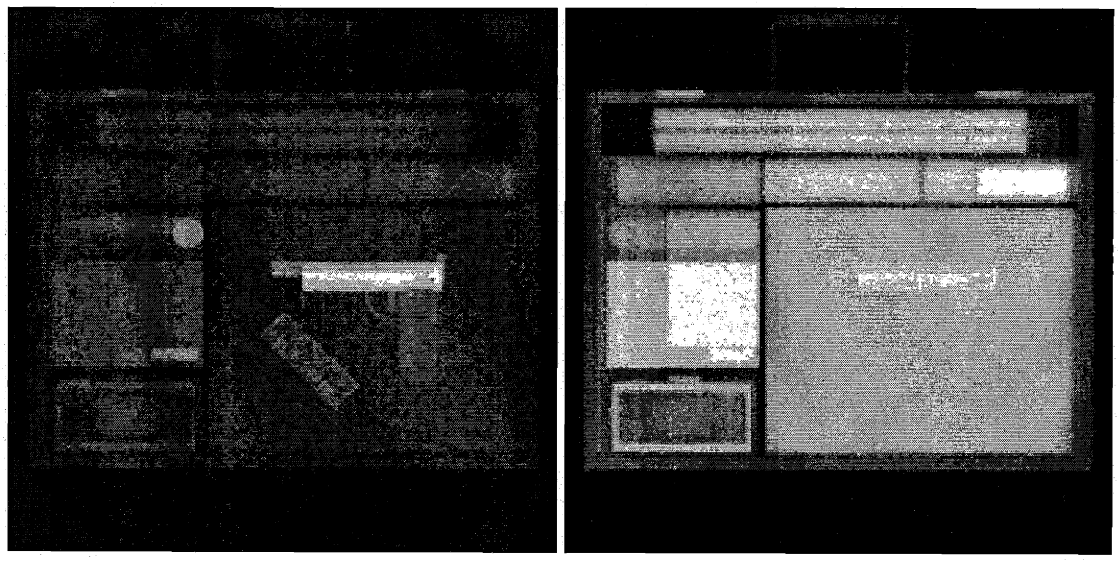

Figure 4.12: Calculated elemental images (Left: sum of others; right: all elements)

With NRR results, we know the elemental composition of items as well as their shapes, which makes it possible to distinguish between organic materials of similar density. The plastic explosive can be identified by its high nitrogen & oxygen content and low hydrogen & carbon content. The stash of cocaine looks different from sugar in that the drug has about equal amounts of hydrogen and carbon but very little oxygen. The bright bar overlapping the drug bag in the carbon image is the polystyrene handle of an umbrella. The pistol, knife blade and the battery are visible in the "other" picture. A glass lens in the camera is also very clear in the oxygen picture. Two aluminum buckles can be seen on the top in the hydrogen picture. As we have mentioned, the calculation splits aluminum content into hydrogen and "other" results.

There are two differences between the neutron radiograph (Figure 4.10) and image of "all elements" (Figure 4.12). The neutron radiograph is an attenuated image (negative) and darker represents more material, while the "all elements" image is positive and brighter means more material. The "all elements" image is the projected atomic density of the object, while the neutron radiograph results from the projected attenuation, which is the product of atomic density and attenuation coefficients.

4.4 NRR Performance

The performance of an imaging method is ultimately measured by spatial resolution (Point Spread Function or Modulation Transfer Function) and Detective Quantum Efficiency (DQE). DQE is a measure of how efficiently an imaging system makes use of the information content of a radiation beam. Because of limited data availability, we will only analyze the spatial resolution and sensitivity issues.

4.4.1 Spatial Resolution

Spatial resolution has been addressed previously in Chapter 2. It is related to size of the neutron source, thickness of the object and the neutron detector, projection angle, geometry factor and performance of the lens. In our application, spatial resolution will not be limited by CCD pixel size. The analysis of spatial resolution is based on sufficiently good statistics. That is, we are talking about spatial resolution under the condition that detected neutron number is sufficiently large and its statistical fluctuation will not affect spatial resolution.

Security applications do not require very good resolution (1-2 cm is good enough). We will discuss spatial resolution that can be provided by practical radiography hardware, and also that required by NRR. All quantitative measures of spatial resolution are transferred to the object plane (see figure 2.11).

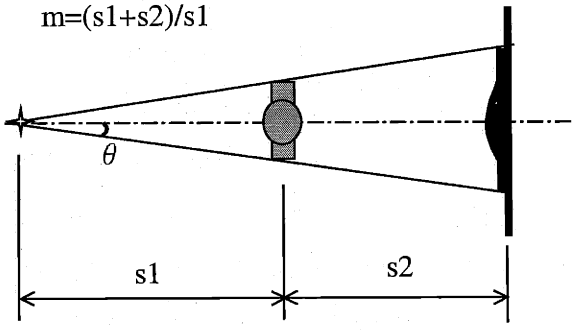

Copy of Figure 2.11 Imaging magnification

In luggage inspection, the object size is typically 50-70 cm and the viewing angle should be restricted to 10-15 degrees for reasonable spatial resolution (thick detector). A 30-50 cm object-detector distance is adequate to prevent scattered neutrons from casting a sharp pattern onto the detector. The following analysis will be based on these parameters:

- Viewing angle: θ=10°
- Source-object distance: s1=150 cm
- Object-detector distance: s2=50 cm
- Detector thickness: t=4 cm
- Source size: ϕ1 cm x 2 cm (gas target)

Radiography Hardware Limits

(1) Detector Intrinsic Resolution

Fast neutrons interact with matter primarily by scattering and therefore the neutron is not absorbed after an interaction. If a neutron is scattered by a hydrogen nucleus, its kinetic energy is reduced to half of its original energy on average. The remaining kinetic energy is larger if the neutron is scattered by any other nucleus. The scattered neutron may interact with detector material again after it travels a distance, leading to another energetic recoil charged particle in a different location. So, one fast neutron deposits it energy in different locations within the detector and leads to multiple scintillation centers. This causes image blurring and is a fact contributing to intrinsic resolution.

Recoil protons travel a distance before they stop, emitting light along their path. Only recoil protons with the maximum energy (from a head-on collision with neutrons) travel along the projection path (neutron direction). Most recoil protons are knocked out at an angle and have a transverse velocity component. As a result, neutrons along a specific project path generate a cylindrical region of light emitting centers (protons). To a less extent, a proton does not travel in a straight line and this straggling also contributes to blurring.

Scintillation light spreads out. Since the lens has only one focal plane, light emitted in other parts of the detector will not be focused sharply onto the CCD camera. In addition, light is scattered in non-transparent detectors. The light path has changed when it exits the surface. Light spread and scattering also contribute to image blurring.

Intrinsic spatial resolution has been measured experimentally with 12 MeV neutrons. The object-detector distance is set to zero (s2=0) so that finite source size makes no contribution. The image is restricted near the center (θ=0°) so there is no non-parallel effect. There is a minor contribution from non-ideal focusing of the lens and the finite pixel size of CCD. The result is given in table 2.2. For 2 cm and 4 cm thick transparent detectors (BC400), the intrinsic spatial resolution (12 MeV neutron) is 0.79 mm and 1.10 mm (FWHM), respectively.

(2) Neutron Source Size

Because of the low density of D_2 gas, a considerable thickness of gas is required for reasonable neutron yield. A 2.3 MeV deuteron (Ed=2.3 MeV) loses 0.4 MeV energy in a 2 cm thick D_2 gas (3 atm) and this is what we need for NRR. The beam can be defocused to minimize the window-heating problem. This leads to increased transverse dimensions. For example, the source size can be 1 cm in diameter and 2 cm in depth (ϕ1 cm x 2 cm). The source size seen at 0° and 90° is 1 cm and 2 cm, respectively.

Under different geometric conditions, source size has a different contribution to the overall spatial resolution. When the object-detector distance is zero (s2=0), the imaging system sees no effect from finite source size and this fact is used to measure detector intrinsic resolution. In general, the shadow of the source on the detector is s2/s1 times as big as the source itself. The contribution to resolution is scaled to the object plane. Recall equation (2.10) and figure 2.13.

$$R_o = R_d \cdot \frac{1}{m} = [R_s \cdot (m-1)] \cdot \frac{1}{m} = R_s \cdot \frac{s2}{s1+s2}. \qquad (2.10)$$

For R_s=2 cm, s1=150 cm and s2=50 cm, spatial resolution caused by finite source size is calculated to be 5 mm in the object plane. In another application (detecting

~1 mm^3 defects), s1=s2=2.5 m and R_s=2 mm (focused deuteron beam, seen at 0°), spatial resolution caused by finite source size is 1 mm.

(3) Non-Parallel Effect

Another big contributor of image blurring is the non-parallel effect. The neutron detector has a thickness (4 cm is proposed for security applications.) and detected neutron events at different depths of a projection path could be registered into different pixels in the image if the projection is at an angle. (See figure 2.15.) This is a combined effect of two factors: (1) projection is at an angle (except for the center of image); and (2) neutron detector has a thickness. The detector thickness is uniform across the image but the projection angle is zero at the center and largest at the edge.

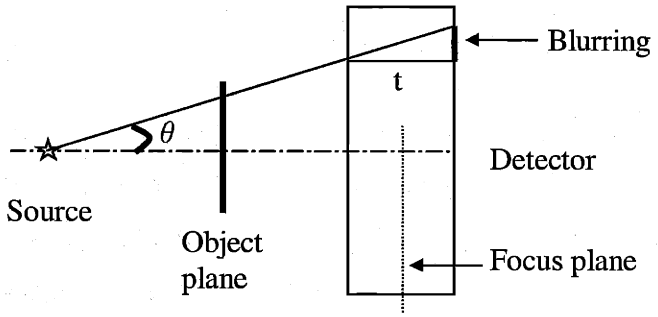

Copy of Figure 2.15 Image distortion and blurring in thick detector

Spatial resolution caused by the non-parallel effect is $t*tan(\theta)$ on the detector plane and it scales to $t*\tan(\theta)*\frac{s1}{s1+s2}$ on the object plane (equation 2.9). For θ=10°, t=4 cm, s1=150 cm and s2=50 cm, spatial resolution is 5.3 mm.

The overall spatial resolution is the combination of that from all three contributions and its value in the object plane is estimated to be ~5 mm at the image center and ~7.5 mm at the edge (10 degree).

Limit Required by NRR

Elemental images are solved from a series of radiographs, with one linear equation set for each pixel. There are two conflicting factors to be considered in choosing pixel size.

The total error in elemental images is related to and larger than the measurement error. (Figure 3.17 gives the vector error of HCNO versus measurement error.) Measurement error is in turn dominated by neutron statistics. Therefore we could have more neutron events and could achieve better measurement S/N by using larger pixel size. The spatial resolution provided by the hardware is estimated to be ~7.5 mm, which is better than what we need for security applications. A 3-5 mm pixel size is satisfactory for S/N considerations and will not significantly degrade spatial resolution (Nyquist's theory requires that sampling frequency is at least twice as high as signal frequency).

On the other hand, our linear model favors small pixel size. We take images at different angles to use different energy neutrons. Unfortunately neutron energy varies across the image in each single measurement, because different parts of the image are at different angles (relative to the d+ beam path, Figure 4.3). As a result, different attenuation coefficients are required for different pixels. These data can be measured experimentally. For example, we can take two images at a nominal angle, with or without a slab of graphite between the neutron source and the detector and we can use the two images to calculate the carbon attenuation coefficients at that nominal angle. A polyethylene slab can used to measure hydrogen attenuation coefficients thereafter. The problem is that neutron energy varies continuously and what we can measure is the attenuation coefficient averaged within an individual pixel area. As a result, our linear model (and equation set method) is correct only for small areas. Using larger pixel size generally decreases the effectiveness of the linear model, especially when neutron cross section varies rapidly with neutron energy (as examples, ~3 MeV and ~4 MeV, the broad resonances of carbon and oxygen). It is difficult to estimate the best pixel size for this reason. Preliminary study suggests 2-10 mm.

The choice of pixel size is a trade off between the need for better S/N (favors large pixel size) and the need to satisfy the linear model (favors small pixel size). Careful experiments are necessary when equipment is available. The final spatial resolution is either ~7.5 mm as provided by the hardware (if the pixel size is small), or at least twice the pixel size (if the pixel size is large, recalling Nyquist's theory.)

4.4.2 Sensitivity and Decision Making

Neutron Resonance Radiography is an absolute measurement method. The attenuation coefficients of hydrogen, carbon, nitrogen and oxygen at each nominal angle are predetermined experimentally. Measurements with an unknown object must be made under the same conditions (accelerated deuteron energy, target type and thickness, source-object distance, object-detector distance and nominal angles). If such requirements are fulfilled, projected elemental contents (absolute value units of atoms/cm^2) in each pixel can be calculated from the linear equation set described previously. Figures 4.13 and 4.14 plot the projected content of the drug region and explosive region of the terrorist overnight bag, respectively.

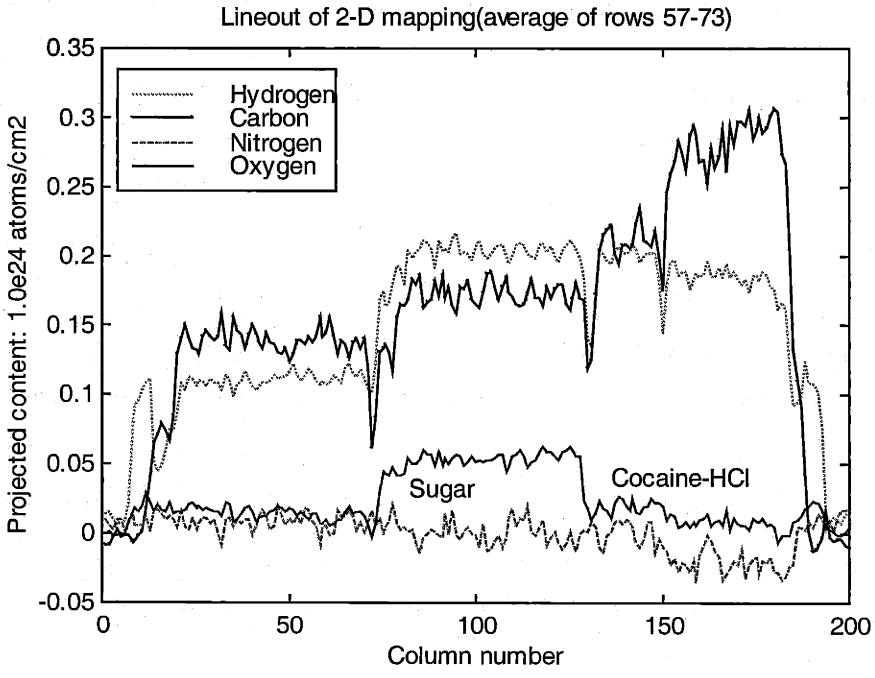

Figure 4.13 Projected content in drug region

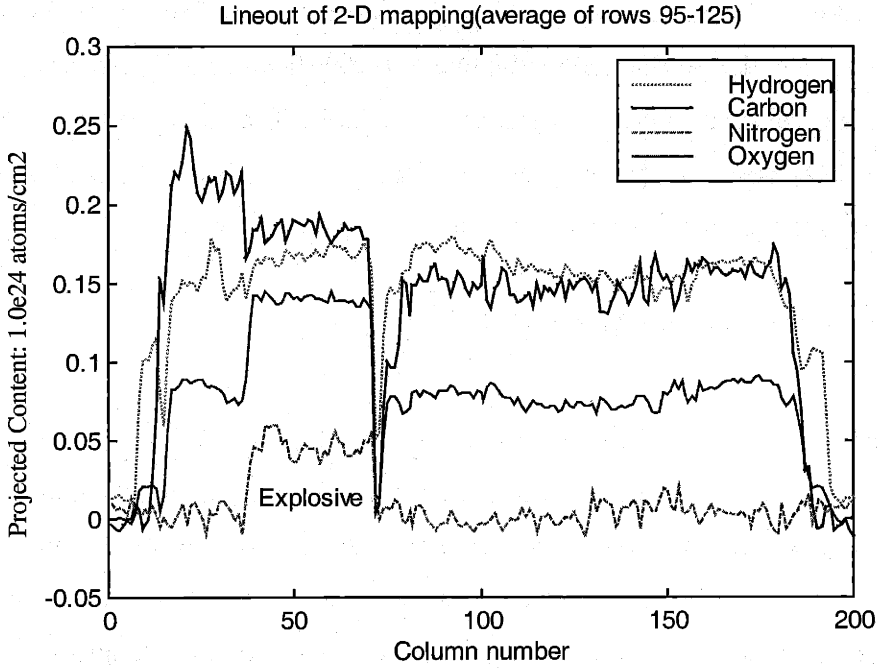

Figure 4.14 Projected content in explosive region

Errors in projected contents have two components: bias and variance. If we repeat the NRR measurement and calculation many times, the difference between the averaged results and the true projected contents is bias. We have noted in chapter 3 that NRR and the least squares methods are unbiased. Variance represents the fluctuation of results, or how repeatable the result is.

The major causes of error are modeling error and measurement error. When neutrons travel through a thickness in the object, their energy spectrum is changed, resulting in non-linearity between the projected contents and total attenuation. In security applications, all elements other than hydrogen, carbon, nitrogen and oxygen are represented with a constant attenuation coefficient. These approximations cause modeling error. Since a constant attenuation profile is close to hydrogen attenuation coefficient, hydrogen has a larger error as observed in the elemental images. Measurement error leads to fluctuation. Figure 3.17 gives an estimate of the relationship. A 2-3% measurement error leads to ~10% vector error in elemental contents. In practice, there is more hydrogen and carbon than oxygen and nitrogen in most organic goods. The same

amplitude of absolute measurement error leads to a much larger relative error in the nitrogen image than in the carbon image.

The lower limit of detection is largely determined by the error level. As observed from the simulation results, 0.01×10^{24} atoms/cm^2 of material should be detectable. In mass thickness, this is equivalent to 0.016 g/cm^2 hydrogen, 0.2 g/cm^2 carbon, 0.23 g/cm^2 nitrogen or 0.26 g/cm^2 oxygen.

To make a decision whether or not there exist drugs or explosives, elemental content information over a region (rather than that in individual pixels) should be employed. A 5 cm by 5 cm area has more than 100 pixels (assuming 3-5 mm pixel size) and therefore a decision based on the area can be expected to be more reliable than that based on one pixel. NRR is a 2-D imaging method and the final result is the projected elemental contents. Decision should not be made directly on the total projected content. Instead, differences among neighboring regions should be considered. That is, we should be concerned about how much more (or less) atoms per square centimeter exist in one region than in its neighborhood, not just the absolute value. After the radiographs at different angle and calculated elemental images become available, decisions can be made in the following manner.

The first step is shape analysis. Both original radiographs and deduced elemental images should be used. In general, original radiographs have better quality (S/N) but are complicated; and elemental images (especially nitrogen and oxygen images) are simpler. Radiographs and elemental images should all be processed with edge-filters. Items with sharp edges will appear very clearly and other items are less clear. Some shapes will appear in all images and others in only some of the images.

The second step is topology analysis. A lot of shapes are overlapped and the purpose of this step is to obtain some sense of the spatial relationship of different items within the inspected object (limited 3-D information). We expect the following information from topology analysis: (1) the thickness (atoms/cm^2 of each element) of each interested item and (2) the region of extension of each interested item. Although we

know that several items overlap in a region, we have no way to tell which item is in the front and which is behind. It's neither possible nor necessary.

The third step is to search a drugs/explosives composition library. Once items of interest have been assigned their total elemental content (atoms/cm^2 of each element), we should search our library to decide whether or not attention should be called to each item. Decisions should be made on the contents of all elements, not just nitrogen or any other element.

4.5 Exposure Requirement and Neutron Shielding

4.5.1 Exposure Requirement

Neutron yield for the DD reaction has been discussed previously. When incoming deuteron energy is 2.3 MeV after penetrating the entrance window, neutron yield with a D_2 gas target (3 atm, 2 cm thick) is $2x10^8$ neutrons/sec/μA total, $9x10^7$ neutrons/sec/Sr/μA at 0°, or $1x10^7$ neutrons/sec/Sr/μA at 90°. For a 150 cm source-object distance (s1) and 5x5 mm^2 pixel size, the number of neutrons reaching each pixel is (assuming 10 μA deuteron current) $1x10^4$ neutrons/sec at 0°, or $1.11x10^3$ neutrons/sec at 90°.

We further assume the object thickness is ~$0.6x10^{24}$ atoms/cm^2. (This is what we may expect in practice.) The average attenuation coefficient is ~$2x10^{-24}$ cm^2 and the resulting ratio of transmission is 0.3. Neutron detection efficiency is ~25% with a 4 cm thick plastic scintillator (Figure 2.7). With the object introduced, the detected neutrons are (assuming 10 μA deuteron current) 750 neutrons/sec at 0° and 83 neutrons/sec at 90°, respectively. Exposure time needed to reach 2-3% statistics is ~2 seconds at 0° and ~20 seconds at 90°.

Neutron yield could be increased with higher gas pressure and/or higher deuteron beam current. This will reduce exposure time.

4.5.2 Shielding

Fast neutrons have a high penetration power and will generate high-energy gamma rays when they interact with matter. These direct fast neutrons and induced gamma rays are harmful to both human beings and equipment. The general method of shielding fast neutrons is to absorb them with light material (polyethylene or wax) and to absorb gamma rays with an outer shell of heavy material (lead). The radiation dose allowed for a controlled area is 2.5 mrem/hr, and it is 0.25 mrem/hr for a non-controlled area [34].

Total neutron yield (10 μA, 3 atm, 2 cm) has been estimated to be $2x10^9$ neutrons/sec. Only a small fraction of the 4π solid angle is used for object inspection and therefore unused neutrons should be shielded locally (source shielding). Additional shielding should be employed behind the neutron detector to absorb transmitted neutrons (safety shielding). This two-step arrangement is very important. Unusable neutrons are killed near the source in order to reduce radiation background in the imaging process and to reduce the outer shielding (beam stop behind the imaging station). Figure 4.15 shows an artist's design of source shielding. Two aperture slits, one at each side, allow fast neutrons to come out for imaging use.

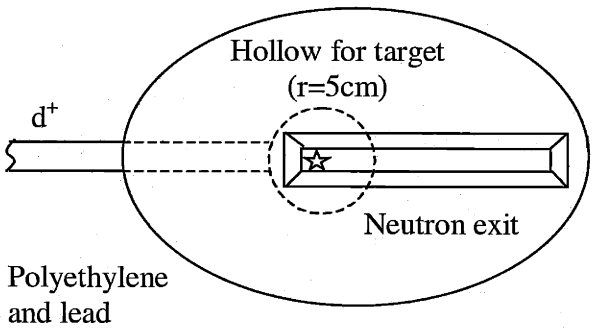

Figure 4.15 Artist's design of source shielding

A DD neutron source is strongly forward focused. In addition, neutrons in the forward direction have high energy and therefore higher penetration power. In the

backward direction, shielding material is removed to allow the beam pipe in. Figure 4.16 gives the dimensions of the source shielding. A piece of polyethylene (ellipsoid, a=55, b=45) sits inside and a lead shell surrounds the polyethylene structure (outer ellipsoid, a=65, b=52). The two ellipsoids are concentric. The DD neutron source is back from the center by 10 cm and there is an R=5 cm spherical hollow region around the source point to facilitate target installation.

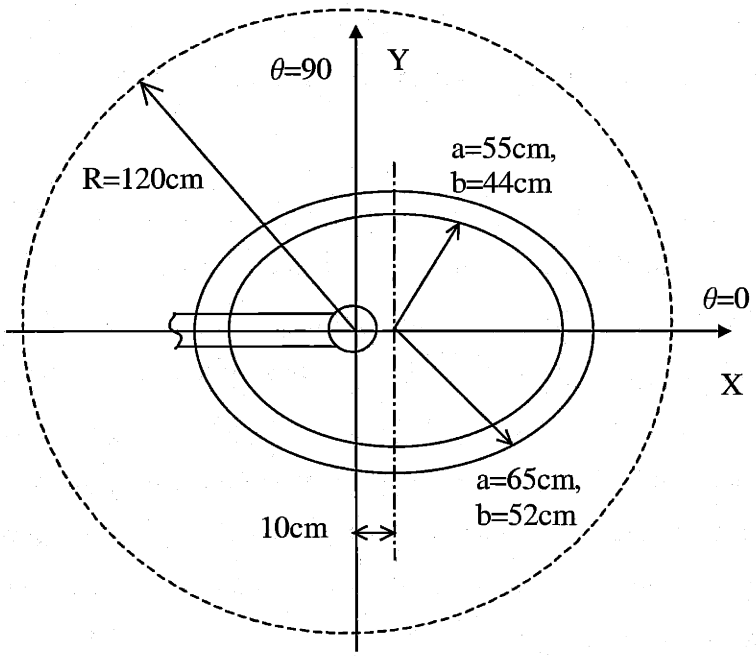

Figure 4.16 Dimensions of source shielding.

The radiation dose at the surface of the source shielding is higher than the allowed 2.5 mrem/h limit. If we enclose the R=120 cm region (centered at the source point, not the shielding structure center), the dose outside the enclosure is below 2 rem/h and meets NCRP standards. The 120 cm distance is allowed by imaging geometry (source-object distance 1.5 m or 2 m). Figures 4.17&4.18 plot Dose at different locations for $2x10^9$ neutrons/s. In figure 4.17, points are designated with viewing angle from the source and point are 10cm (normal) away from the lead surface. In figure 4.18, points are also designated with viewing angle but they are located on the R=120cm sphere.

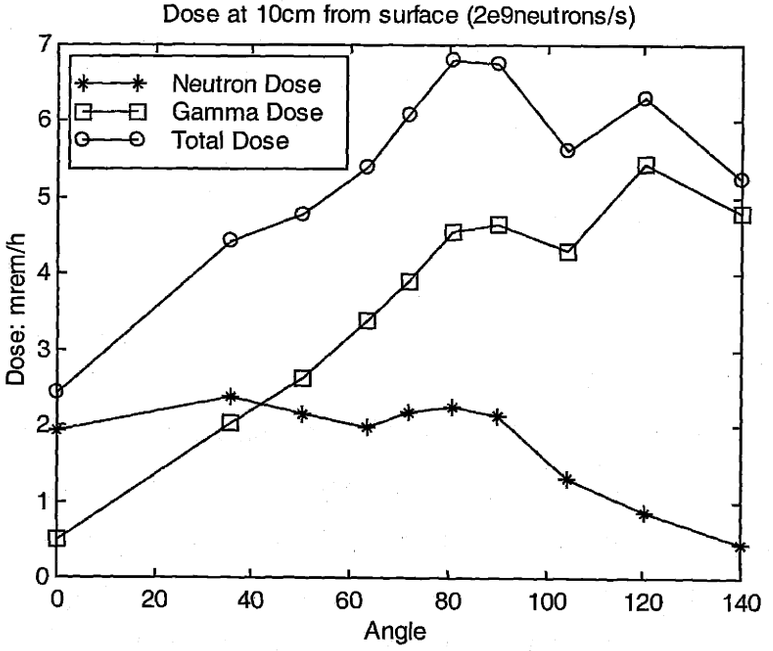

Figure 4.17 Dose near shielding surface ($2x10^9$ neutrons/s)

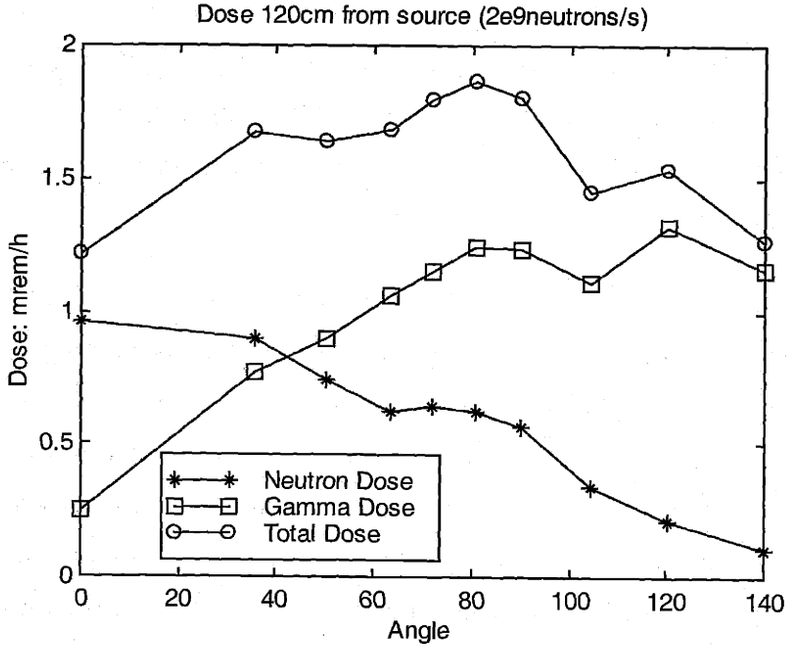

Figure 4.18 Dose outside enclosure ($2x10^9$ neutrons/s)

Chapter 5

Summary

We have discussed a new imaging method, which does more than just image an object in the ordinary way. Fast neutron resonance radiography (NRR) provides images of individual elements so that interesting items may be identified by their elemental signatures. Hydrogen, carbon, nitrogen and oxygen are the major elements of organic goods and that have raised the need for elemental imaging methods. NRR calculates the 2-D mapping of these elements (and of any others) from a series of radiographs taken with different energy fast neutrons. Immediate application can be found in explosives/drugs detection. The major features of NRR are: (1) fast neutron radiography equipment; (2) a method of obtaining neutrons of different energies; (3) an algorithm to solve for projected elemental contents from radiographs; and (4) a way to identify drugs and explosives security applications). This thesis work dealt with the first three parts.

Fast neutron radiography has not been widely used since fast neutrons are relatively expensive. The physics of image formation has not been well studied as in X-ray radiography or in thermal neutron radiography. The exclusive way to detect fast neutrons is through proton-recoil. Small cross sections (~2 barns in our application) raise the need for a thick detector and the short range of recoil protons requires a way to carry the detection information outside the detector. Scintillation material has been chosen as a fast neutron detector. Two types of scintillators, a PP-converter (loaded with ZnS) and a plastic scintillator, have been investigated. PP-converter has a much higher light output but it is only available in ~2 mm thickness, leading to very inefficient use of the neutron beam. Thicker (2-4 cm) plastic scintillator has proven to be the right choice. Other facts that affect image quality (neutron source size, geometry, optics, etc.) have been studied in

detail. Non-linear filtering is required to preprocess the recorded images in order to remove sparkles.

An RFQ accelerator and the DD reaction have been recommended to generate fast neutrons. An RFQ is compact and reliable but is often designed to accelerate a specific particle to a specific energy. A 2.3 MeV deuteron beam energy (if there is an entrance window, this is the energy after passing the window) and a thick target (up to 0.8 MeV deuteron energy) are able to generate 2-5.5 MeV neutrons. By rotating the object-detector assembly, 2.2-5.5 MeV neutrons are obtained for images at different angles from the source. This energy range covers the most noticeable broad resonances of carbon, nitrogen and oxygen. The hydrogen cross section has a monotonic decrease over the same energy range. Radiographic images at different angles (neutron energies) will show some differences. These differences add up when solving the linear equation set for each pixel.

Elemental images are calculated from radiographs taken at different angles (neutron energies). One radiograph forms an equation for each pixel, stating that the total attenuation is the sum of attenuation by different elements. A series of radiographs lead to a linear equation set for each pixel. These equation sets are generally ill-conditioned and care must be taken to solve them. The direct Householder transform has been suggested. The criterion of choosing the angles at which radiographs are taken is to maximize attenuation contrast. Attenuation coefficients of different elements at various nominal angles should be determined experimentally in advance and measurements of the inspected object provide total attenuation.

This work is the very first stage of NRR, mainly dealing with the physics concepts and pointing out a possible engineering approach. The next step in this work should be concentrated on experimental study rather than engineering design. Experiments should permit optimizing pixel size, imaging angles, detector thickness, deuteron target type/size and image geometry. An existing electrostatic accelerator could be used to accelerate deuterons to a fixed energy but a better CCD camera system is necessary.

References

[1] ONDCP report, National Drug Control Strategy: 2000 Annual Report.

[2] T. Gozani, "Principles of Nuclear-Based Explosive Detection Systems". Proceedings of the First International Symposium on Explosive Detection Technology. Atlantic City, November 1991.

[3] R. A. Krauss, "Signatures of Explosives by Elemental Composition Analysis". Proceedings of the Second International Symposium on Explosive Detection Technology. Atlantic City, November 1991.

[4] T. Gozani, "Advances in Accelerator Based Explosives Detection Systems". Proceedings of the First International Symposium on Explosive Detection Technology. Atlantic City, November 1991.

[5] T. Gozani, "Thermal Neutron Analysis for Explosives Detection". Proceedings of the First International Symposium on Explosive Detection Technology. Atlantic City, November 1991.

[6] T. Gozani et al, US Patent # 5076993.

[7] G. Vourvopoulos, F. J. Schultz and J. Kehayias, "A Pulsed Fast-Thermal Neutron Interrogation System". Proceedings of the First International Symposium on Explosive Detection Technology. Atlantic City, November 1991.

[8] Richard C. Lanza, et al, "CAFNA, Coded Aperture Fast Neutron Analysis: Application to Contraband and Explosive Detection". Proceedings of Third International Topical Meeting on Nuclear Applications of Accelerator Technology. Long Beach, CA, November 14-18, 1999.

[9] Richard C. Lanza et al, "CAFNA, Coded Aperture Fast Neutron Analysis: Application to Contraband and Explosive Detection". Proceedings of 1999 ONDCP International Technology Symposium. Washington, DC, March 8-10, 1999.

[10] Z. P. Sawa and T. Gozani, "A PFNA Technique for the Detection of Explosives". Proceedings of the First International Symposium on Explosive Detection Technology. Atlantic City, November 1991.

[11] Beyerle, R. Durkee, G. Headley, J. P. Hurley and L. Tunnell, "Associated Particle Imaging". Proceedings of the First International Symposium on Explosive Detection Technology. Atlantic City, November 1991.

[12] J. C. Overlay, "Neutron Resonance Attenuation for Explosive Detection". Proceedings of 12th International Conference on the Applications of Accelerators in Research and Industry. Denton, Texas, 1992.

[13] H. J. Gomberg and B. G. Kushner, "Neutron Elastic Scatter for Explosives Detection Systems". Proceedings of the First International Symposium on Explosive Detection Technology. Atlantic City, November 1991.

[14] NMAB-482-6. The Practicality of Pulsed Fast Neutron Transmission Spectroscopy for Aviation Security. Washington D.C., 1999.

[15] Fast Neutron Resonance Radiography for Security Applications. Presented at the Sixteenth International Conference on Application of Accelerators in Research and Industry. Denton, Texas, November 1-4, 2000. To be published in the American Institute of Physics Conference Proceedings.

[16] M. Goldberg, "Gamma Resonance Attenuation for Explosive Detection". Proceedings of 12th International Conference on the Applications of Accelerators in Research and Industry. Denton, Texas, 1992.

[17] J. R. Clifford and R. B. Miller, "Photon Nuclear Activation for Explosive Detection". Proceedings of the First International Symposium on Explosive Detection Technology. Atlantic City, November 1991.

[18] R. W. Hamm, "The RFQ Linac: A High-Current Compact Ion Accelerator for Explosive Detection". Proceedings of the First International Symposium on Explosive Detection Technology. Atlantic City, November 1991.

[19] Richard M. Ambrosi, A Model for the Physics of Image Formation in Fast Neutron Radiography. Ph.D. Thesis, University of Witwatersrand, Johannesburg, 1999.

[20] Princeton Instruments, TEA/CCD-1242E User's Manual.

[21] Mario Conte and William W. Mackay, Physics of Particle Accelerators. World scientific publishing Co., 1991.

[22] ShuangHe Shi, An Accelerator-Based Neutron Imaging System and Its Application to Detection of Corrosion in Aircraft. MIT PhD thesis, 1995.

[23] Kingslake, Editor, Applied Optics & Optical Engineering. Academic Press, 1965.

[24] Charles Kittel, Introduction to Solid State Physics. John Wiley & Sons, Inc., 1986.

[25] L. E. Antouk et al, "Large Area Amorphous Silicon Potodiode Arrays for Radiotherapy and Diagnostic Imaging". NIM(A), Vol. 310, 1991, pp. 460-464.

[26] G. Chen et al, "A Special Error in On-Line Industry Monitors by Gamma rays". *Proceedings of the Seventh National Conference on Nuclear Electronics & Nuclear Detection Technology*. Lushan, China, October 6-12, 1994.

[27] Dongwei Hei, *EDXRF Rare Earth Elements Fast Analysis*. S. B. Thesis, Tsinghua University, 1992.

[28] OECD/NEA report: Neutron Sources for Basic Physics and Applications. Pergamon Press, 1983.

[29] R. C. Lanza, et al, "The Plasma Porthole: a Windowless Vacuum-Pressure Interface with Various Accelerator Applications". Proceedings of 15th International Conference on Applications of Accelerators in Research and Industry. Denton, TX, 1998.

[30] Eric R. Empey, Implementation of a Closed Loop Windowless Gas Target System for Neutron Production. MIT M.S. thesis, 2000.

[31] T. Wilcox and E. Lent, COG - A Particle Transport Code Designed to Solve the Boltzman Equation for Deep-Penetration (Shielding) Problems, Vol. 1 Users Manual, LLNL Rept. # M-221-1 (1989); see also R. Buck and E. Lent, "COG: A New, High-Resolution Code for Modeling Radiation Transport," LLNL Energy and Technology Review (June 1993); additional information on COG may be obtained at URL http://www-phys.llnl.gov/N_Div/COG/.

[32] J. Hall, "Monte Carlo Modeling of Neutron and Gamma-Ray Imaging Systems". SPIE **2867**, 465 (1996).

[33] Judith F. Briesmeister, *MCNP—A General Monte Carlo N-Particle Transport Code*, LANL, March 1997.

[34] NCRP Report No. 51: *Radiation Protection Design Guidelines for 0.1-100MeV Particle Accelerator Facilities*. Washington, D.C., 1977.

[35] K. S. Krane, *Introduction to Nuclear Physics*. John Wiley & Sons Inc., 1988.

[36] R. Evans, *The Atomic Nucleus*. McGraw Hill, 1955.

[37] J. Byrne, *Neutrons, Nuclei and Matter*. IOP Publishing Ltd., 1994.

[38] G. E. Baconn, *Neutron Physics*. Wykeham Publications, London, 1969.

[39] *Atomic Data and Nuclear Data Tables*, Vol. 15, No. 7, 1975, pp. 57-84.

[40] A. Z. Kiss et al, "Measurement of Relative Thick Target Yields for PIGE Analysis on Light Elements in the Proton Energy Interval 2.4-4.2MeV". *Journal of Radioanalytical and Nuclear Chemistry*, Vol. 89, No. 1, 1985, pp.123-141.

[41] *Nuclear Data Tables*, Vol. 11, No. 7, 1973, pp. 586-599.

[42] Nuclear Data Viewer, http://t2.lanl.gov

[43] H. Berger, *Neutron Radiography*. Elsevier Press, 1965.

[44] A. A. Harms, *Mathematics and Physics of Neutron Radiography*. D. Reidel Publishing Company.

[45] J. B. Birks, *The Theory and Practice of Scintillation Counting*. Pergamon Press, 1964.

[46] R. L. Craun et al, "Analysis of Response Data for Several Organic Scintillators", *NIM* (80). 1970, pp. 239-244.

[47] Nicholas Tsoulfanidis, *Measurement and Detection of Radiation*. Hemisphere Publishing Company, 1983.

[48] G. F. Knoll, *Radiation Detection and Measurement*. John Wiley & Sons Inc., 1989.

[49] Changsong Ji, *Handbook of Nuclear Radiation Detectors & Their Experiment Techniques*. Atomic Energy Press, China, 1990.

[50] Alan V. Oppenheim, *Discrete-Time Signal Processing*. Prentice Hall, Inc., 1989.

[51] Sabine Van Huffel, et al, *The Total Least Squares Problem, Computational Aspects and Analysis*. Society for Industrial and Applied Mathematics, Philadelphia, 1991.

[52] Anthony F. Milis, *Heat Transfer*. Richard D. Irwin, Inc., 1992

[53] Gerhard S. Lewin, *Fundamentals of Vacuum Science and Technology*. McGraw-Hill, 1965.

[54] A. Chambers, *Basic Vacuum Technology*. IOP Publishing, 1998.

[55] F. Chen, *Introduction to Plasma Physics*. Plenum, New York, 1977.

[56] Chad Lee, *The Design of an Intense Accelerator-Based Epithermal Neutron Beam Prototype for BNCT Using Near-Threshold Reactions*. Ph.D. thesis, MIT, 1998.

Appendix

A.1 Variance-Checking median filter

Images recorded with a CCD camera usually have sparkles (dark or white points, lines or clusters). This is caused by either device defects or radiation hitting the CCD chip. Median filters are commonly used to remove these sparkles. Median filters are nonlinear filters, by which a pixel value is changed to have the median value of the pixels within its neighborhood (usually 3x3 or 5x5), i.e. half of the pixels in the neighborhood will have values above the median and half will have values below the median. The median filter changes values of almost all pixels, whether they are sparkles or not. This eliminates the chance of improving S/N with a linear filter thereafter.

An improved median filter has been used in our study. Sparkles are detected with a deviation check. That is, the pixel value is replaced with the median value only if it deviates from the median within the neighborhood to a certain extent. (For example, one standard deviation of the neighborhood values.) The modified median filter removes sparkles but preserves fine structures in the digital images.

A Matlab code of a 3x3 variance-checking median filter is given below. It is given as a Matlab function. Input parameter 'a' and output parameter 'y' are the original and cleaned images, respectively. Input parameter 'ratio' tells the function what multiple of the standard deviation is to be used and 'count' returns the total numbers of downward modified pixels and of upward modified pixels.

```
function [y,count]=removestar3(a,ratio)
%remove stars in the image
%3x3 area is used
%the 9 values is first sorted
%median, mean and std are then calculated
%the central pixel is modified if its values goes beyond median+/-rat*std
[rows,cols]=size(a);
count=[0 0];
for m=1:rows,
   if  m == 1
       mm=-1;
   elseif m==rows
```

```
        mm=-3;
    else
        mm=-2;
    end

for n=1:cols,
    if  n == 1
        nn=-1;
    elseif n==cols
        nn=-3;
    else
        nn=-2;
    end

    y(m,n)=a(m,n);
    clear b;
    for i=1:3,
    for j=1:3,
       b(i*3-3+j)=a(m+mm+i, n+nn+j);
    end;
    end
    b=sort(b);
    median=b(5);
    ave=mean(b);
    dev=std(b);
    dev=dev*dev+(median-ave)*median-ave);
    dev=sqrt(dev);
  if  (y(m,n)<median-rat*dev)
      y(m,n)=median;
      count(1)=count(1)+1;
  end
  if ( y(m,n) > ave+rat*dev)
        y(m,n)=ave;
       count(2)=count(2)+1;
  end;

end;
end
```

A.2 Householder Transform for Least-Squares fitting

Linear equation sets encountered in NRR are typically ill-conditioned. That is, some row or column vectors are almost parallel to each other. Large errors will occur if a linear equation set is not handled properly. An equation set is always over-determined in NRR to obtain a more stable solution so it is a least-squares problem. It is not advised to form and solve its normal eqautions. Instead, the direct Householder Transform has been found to be successful.

Following is the Matlab code to solve the least squares problem with Householder transform. It is written as a function. The input parameter 'ab' is the input matrix of [A | B] and 'n' is the number of columns in matrix A (or the number of elements of one 'x' vector). The returned parameter 'x' is a matrix the size of matrix B. When B is a vector, so is 'x' and the function call solves one equation set. If we put several 'b' vectors into matrix B, the function call solves these equation sets in a more efficient way.

```
function x=householder(ab,n)
% Solve the least square problem 'ax=b'
%with Householder transform method
%input 'ab' is the augmented matrix [a b]
%input the number of 'x's, or columns of 'a'
%output the solution 'x'

[row,col]=size(ab);
if row<n
error('The solution is not definite');
end

%Upper trianglize a
for k=1:n
  s=sqrt(ab(k:row,k)'*ab(k:row,k));
  if ab(k,k)<0.0
    s=0.0-s;
  end
  u(k)= sqrt(1.0+ab(k,k)/s);
  c=1.0/(s*u(k));
  for i=k+1:row
    u(i)=c*ab(i,k);
  end
  for i=k:col
    c=u(k:row)*ab(k:row,i);
    ab(k:row,i)=ab(k:row,i)-c*u(k:row)';
  end
end
```

```
%Back solve equations
x=ab(1:n,n+1:col);
for k=1:col-n
  x(n,k)=x(n,k)/ab(n,n);
  for i=n-1:-1:1
    s=ab(i,i+1:n)*x(i+1:n,k);
    x(i,k)=(x(i,k)-s)/ab(i,i);
  end
end
```

A.3 COG Code for NRR Simulation

This code was provided by Dr. James Hall at Lawrence Livermore National Laboratory.

```
Radiography problem (Hall; 09/08/00) (Filename "nscn01")

$  Simulation of MIT radiation scanner for luggage inspection.

$  Luggage case (16" X 12" X 4") located 147.45 cm from source.
$  Detector located 50 cm behind case (=> magnification ‰ 1.3391).
$  Blurring radius due to finite source size ‰ 0.200 cm.

$  ********************* Imaging @  0° **********************

$  Density of explosive mix set to 1.0 g/cc (=> 268.8 g total).
$  Density of cocaine-HCl set to 0.90 g/cc (=> 105.2 g total).

$  LONG RUN (500,000,000 particles)

BASIC

$  Track neutrons only.
$  Units of the problem: centimeters, MeVs, and seconds.

   neutron
   cm
   MeV
   sec

PVM

   nslaves 127     $ run with 127 slaves
   tslaves 10      $ report every 10 minutes

SURFACES

$  Luggage case (aluminum shell with cloth cover)

   101   box         +40.6400  +30.4800  +10.1600  $ luggage case
            TR    +0.0000   +0.0000   +0.0000
   102   box         +40.3225  +30.1625   +9.8425
            TR    +0.0000   +0.0000   +0.0000
   103   box         +40.0050  +29.8450   +9.5250
            TR    +0.0000   +0.0000   +0.0000
   104   cylinder     +0.6350   +5.0800   -5.0800
            TR    +0.0000  -21.4314   +0.0000
   105   box          +0.6350   +6.3500   +1.2700
            TR    +5.3976  -18.2564   +0.0000
   106   box          +0.6350   +6.3500   +1.2700
            TR    -5.3976  -18.2564   +0.0000
   107   cylinder     +0.4763   +1.9050   -1.9050
```

```
        TR  +13.0176  +15.0813   +0.0000
108  cylinder     +0.4763   +1.9050   -1.9050
        TR  -13.0176  +15.0813   +0.0000
109  box          +3.8100   +0.6350   +3.8100
        TR  +13.0176  -15.3989   +0.0000
110  box          +3.8100   +0.6350   +3.8100
        TR  -13.0176  -15.3989   +0.0000

$  Pistol (packed in cotton shirts)

111  cylinder     +0.6350  +12.0650   -1.9050 $ pistol assembly
        TR  +0.0000   -5.0800   +0.0000
112  cylinder     +0.3175  +12.0650   -1.2700
        TR  +0.0000   -5.0800   +0.0000
113  cylinder     +1.2700   +9.5250   -1.9050
        TR  +0.0000   -4.4450   +0.0000
114  box          +3.8100   +8.8900   +2.5400
        TR  +0.0000   +0.0000   +0.0000
115  cylinder     +2.5400   +0.3175   -0.3175
        TR  +1.9050   -3.1750   +0.0000
           +1.9050   -3.1750   +1.0000
116  cylinder     +2.2225   +0.3175   -0.3175
        TR  +1.9050   -3.1750   +0.0000
           +1.9050   -3.1750   +1.0000
117  box          +0.6350   +1.9050   +0.6350
        TR  +2.2226   -2.5400   +0.0000
118  box          +0.6350   +2.5400   +0.6350
        TR  -1.9050   -5.0800   +0.0000
119  box          +1.2700   +0.6350   +0.3175
        TR  +11.4300   -5.7150   +0.0000
120  cylinder     +0.3175   +8.8900   +3.8100
        TR  +0.0000   -3.9688   +0.0000
121  box          +2.7395   +8.8895   +0.8345
        TR  +0.0000   +0.0000   +0.0000
122  box          +2.5400   +8.2550   +0.6350
        TR  +0.0000   +0.0000   +0.0000
123  plane        +0.0000   +0.0000   +0.0000
           +0.0000   -1.0000   +0.0000
        TR  +0.0000   +4.2275   +0.0000
124  cylinder     +0.3075   +1.1700   -1.1700
        TR  +0.0000   -3.7100   +0.0000
126  cylinder     +0.3075   +1.1700   -1.1700
        TR  +0.0000   -2.9750   +0.0000
128  cylinder     +0.3075   +1.1700   -1.1700
        TR  +0.0000   -2.2400   +0.0000
130  cylinder     +0.3075   +1.1700   -1.1700
        TR  +0.0000   -1.5050   +0.0000
132  cylinder     +0.3075   +1.1700   -1.1700
        TR  +0.0000   -0.7700   +0.0000
134  cylinder     +0.3075   +1.1700   -1.1700
        TR  +0.0000   -0.0350   +0.0000
136  cylinder     +0.3075   +1.1700   -1.1700
        TR  +0.0000   +0.7000   +0.0000
138  cylinder     +0.3075   +1.1700   -1.1700
        TR  +0.0000   +1.4350   +0.0000
140  cylinder     +0.3075   +1.1700   -1.1700
```

```
        TR  +0.0000  +2.1700  +0.0000
142 cylinder    +0.3075  +1.1700  -1.1700
        TR  +0.0000  +2.9050  +0.0000
144 plane       +0.0000  +0.0000  +0.0000
            +1.0000  +0.0000  +0.0000
        TR  +0.3175  +0.0000  +0.0000
145 box         +25.4000 +20.3200 +7.6200 $ shirts
        TR  +4.4450  +0.0000  +0.0000

321 box         +2.7400  +8.8899  +0.8350 $ unit cell (guncp1)
        TR  +0.0000  +0.0000  +0.0000
            +1.0000  +0.0000  +0.0000
            +0.0000  +1.0000  +0.0000
322 box         +2.7400  +8.8899  +0.8350 $ unit cell (guncp2)
        TR  +8.8900  +2.5400  +0.0000
            +9.5971  +3.2471  +0.0000
            +8.1829  +3.2471  +0.0000
345 box         +25.4000 +20.3200 +7.6200 $ unit cell (shirts)
        TR  -6.6675  +4.1276  -0.6350
            -5.6675  +4.1276  -0.6350
            -6.6675  +5.1276  -0.6350

$  Umbrella (nylon with aluminum supports)

146 cylinder    +0.4763  +18.7325  -15.2400 $ umbrella assembly
        TR  +0.0000  +0.0000  +0.0000
147 cylinder    +0.3175  +18.7325  -15.2400
        TR  +0.0000  +0.0000  +0.0000
148 cylinder    +0.7938  +19.0500  +18.4150
        TR  +0.0000  +0.0000  +0.0000
149 cylinder    +1.5875  -11.4300  -19.0500
        TR  +0.0000  +0.0000  +0.0000
150 cylinder    +0.0313  +17.7800  -10.7950
        TR  +0.0000  +1.1906  +0.0000
151 cylinder    +0.0313  +17.7800  -10.7950
        TR  +0.0000  +0.8419  +0.8419
152 cylinder    +0.0313  +17.7800  -10.7950
        TR  +0.0000  +0.0000  +1.1906
153 cylinder    +0.0313  +17.7800  -10.7950
        TR  +0.0000  -0.8419  +0.8419
154 cylinder    +0.0313  +17.7800  -10.7950
        TR  +0.0000  -1.1906  +0.0000
155 cylinder    +0.0313  +17.7800  -10.7950
        TR  +0.0000  -0.8419  -0.8419
156 cylinder    +0.0313  +17.7800  -10.7950
        TR  +0.0000  +0.0000  -1.1906
157 cylinder    +0.0313  +17.7800  -10.7950
        TR  +0.0000  +0.8419  -0.8419
158 cylinder    +1.9050  +18.4149  -11.1125
        TR  +0.0000  +0.0000  +0.0000

359 cylinder    +1.9050  +19.0500  -19.0500 $ unit cell (umbrll)
        TR  +0.0000  -8.2549  -2.5400
            +1.0000  -8.2549  -2.5400
            +0.0000  -7.2549  -2.5400
```

```
$  Camera (plastic body)

  160  box        +11.4300   +5.7150   +3.8100 $  camera assembly
          TR   +0.0000   +0.0000   +0.0000
  161  box        +10.7950   +4.4450   +3.1750
          TR   +0.0000   +0.0000   +0.0000
  162  box         +2.5400   +0.6350   +1.9050
          TR   +0.0000   -3.1745   -0.9525
  163  cylinder    +1.2700   +0.4763   -0.4763
          TR   +0.0000   +0.0000   +2.0633
             +0.0000   +0.0000   +3.0633
  164  cylinder    +0.9525   +0.4763   -0.4763
          TR   +0.0000   +0.0000   +2.0633
             +0.0000   +0.0000   +3.0633
  165  cylinder    +0.3175   +3.3338   -2.5400
          TR   +3.8100   +0.0000   +0.0000
             +3.8100   -1.0000   +0.0000
  166  cylinder    +0.9525   +0.3175   -0.3175
          TR   +3.8100   -2.8575   +0.0000
             +3.8100   -3.8575   +0.0000
  167  cylinder    +0.3175   +3.3338   -2.5400
          TR   -3.8100   +0.0000   +0.0000
             -3.8100   -1.0000   +0.0000
  168  box         +1.9050   +0.3175   +0.6350
          TR   -4.7625   -3.1750   +0.0000
  169  box         +5.0800   +3.1750   +0.1588
          TR   +0.0000   +0.0000   +0.7144
  170  box         +5.0800   +3.1750   +1.2700
          TR   +0.0000   +0.0000   -0.6350
  171  cylinder    +1.0319   +2.0638   -2.0638
          TR   -3.8100   +0.0000   +0.0000
             -3.8100   -1.0000   +0.0000
  172  cylinder    +0.9525   +1.9050   -1.9050
          TR   -3.8100   +0.0000   +0.0000
             -3.8100   -1.0000   +0.0000

  373  box        +11.4300   +6.3500   +4.4450 $  unit cell (camera)
          TR  +13.0175  +11.1126   -2.2225
            +14.0175  +11.1126   -2.2225
            +13.0175  +12.1126   -2.2225

$  Paperback book (book paper)

  174  box        +12.7000   +8.8900   +2.5400 $  book
          TR   +0.0000   +0.0000   +0.0000

  374  box        +12.7000   +8.8900   +2.5400 $  unit cell (pbbook)
          TR  +13.0175   +2.8576   -3.1750
            +14.0175   +2.8576   -3.1750
            +13.0175   +3.8576   -3.1750

$  Switchblade knife (steel blade with wooden handle)

  175  box        +10.1600   +2.5400   +1.5875 $  knife assembly
          TR   +0.0000   +0.0000   +0.0000
  176  cylinder    +1.2700   +0.7938   -0.7938
```

```
          TR  +5.0800  +0.0000  +0.0000
              +5.0800  +0.0000  +1.0000
  177  cylinder    +1.2700  +0.7938  -0.7938
          TR  -5.0800  +0.0000  +0.0000
              -5.0800  +0.0000  +1.0000
  178  cylinder    +1.2700  +0.4763  -0.4763
          TR  -5.0800  +0.0000  +0.0000
              -5.0800  +0.0000  +1.0000
  179  prism   6  -1.2700  +0.0000
              -1.5875  -3.4925
              -1.5875  -7.3025
              -0.6350  -10.7950
              +0.3175  -6.0325
              +0.0000  +0.0000
              +0.1588
              -0.1588
          TR  -5.0800  +0.0000  +0.0000
              -5.0800  +0.0000  +1.0000

  380  box       +12.7000  +2.8575  +1.5875 $ unit cell (swknfe)
          TR  +13.0175  -4.1274  -3.6513
              +14.0175  -4.1274  -3.6513
              +13.0175  +3.1274  -3.6513

$  Plastic explosive (with electrical detonator)

  181  box       +7.6200  +11.1125  +3.1750 $ bomb assembly
          TR  +0.0000  -0.9525  +0.0000
  182  box       +2.5400  +1.8256  +2.5400
          TR  +2.1167  +5.5959  +0.0000
  183  cylinder    +0.6350  +1.9050  -1.9050
          TR  -1.4817  +5.3181  +0.6747
  184  cylinder    +0.6350  +1.9050  -1.9050
          TR  -1.4817  +5.3181  -0.6747

  385  box       +7.6200  +13.0175  +3.1750 $ unit cell (plexpl)
          TR  +10.2658  +0.7939  +0.0000
              +11.2658  +0.7939  +0.0000
              +10.2658  +1.7939  +0.0000

$  Writing set (with plastic case)

  186  box       +5.0800  +13.0175  +1.9050 $ writing set
          TR  +0.0000  +0.0000  +0.0000
  187  box       +4.7625  +12.7000  +1.5875
          TR  +0.0000  +0.0000  +0.0000
  188  cylinder    +0.4763  +5.7150  -5.7150
          TR  +0.7938  +0.0000  +0.0000
              +0.7938  -1.0000  +0.0000
  189  cylinder    +0.1588  +5.7150  -5.7150
          TR  +0.7938  +0.0000  +0.0000
              +0.7938  -1.0000  +0.0000
  190  cylinder    +0.5556  +0.4763  -0.4763
          TR  +0.7938  +5.3975  +0.0000
              +0.7938  -4.3975  +0.0000
  191  cone      +0.9525  +0.4763
```

```
            +0.0000  +11.4300
         TR  +0.7938   -5.7150   +0.0000
            +0.7938   -4.7150   +0.0000
192  cylinder     +0.4763   +5.7150   +0.0000
         TR  -0.7938   +0.0000   +0.0000
            -0.7938   -1.0000   +0.0000
193  cylinder     +0.3968   +0.0000   -0.6350
         TR  -0.7938   +0.0000   +0.0000
            -0.7938   -1.0000   +0.0000
194  cylinder     +0.2381   +5.7150   -0.6350
         TR  -0.7938   +0.0000   +0.0000
            -0.7938   -1.0000   +0.0000
195  cylinder     +0.4763   -0.0001   -5.0800
         TR  -0.7938   +0.0000   +0.0000
            -0.7938   -1.0000   +0.0000
196  cylinder     +0.3969   -0.0001   -4.9213
         TR  -0.7938   +0.0000   +0.0000
            -0.7938   -1.0000   +0.0000
197  cylinder     +0.1588   +5.7150   -5.7150
         TR  -0.7938   +0.0000   +0.0000
            -0.7938   -1.0000   +0.0000
198  cone         +0.9525   +0.4763
            +0.0000  +11.4300
         TR  -0.7938   -5.7150   +0.0000
            -0.7938   -4.7150   +0.0000

386  box          +5.0800  +13.0175   +1.9050 $ unit cell (wrtset)
         TR +17.0392   +0.7939   -0.6350
           +18.0392   +0.7939   -0.6350
           +17.0392   +1.7939   -0.6350

$  Wool sweater

199  box          +12.9117  +24.4475   +3.8100 $ wool sweater
         TR  +0.0000   +0.0000   +0.0000

200  box          +8.8900  +14.2875   +3.8100 $ exclusion zone
         TR +10.2658   +0.7939   +0.0000
           +11.2658   +0.7939   +0.0000
           +10.2658   +1.7939   +0.0000

399  box          +12.9117  +24.4475   +3.8100 $ unit cell (woolsw)
         TR +12.9117   +2.0639   +2.5400
           +13.9117   +2.0639   +2.5400
           +12.9117   +3.0639   +2.5400

$  Note pad (with plastic cover)

201  box          +22.8600  +27.9400   +0.9525 $ note pad
         TR  +0.0000   +0.0000   +0.0000
202  box          +22.6219  +27.9400   +0.4763
         TR  -0.1191   +0.0000   +0.0000
203  box          +21.5900  +26.6700   +0.4761
         TR  +0.0000   +0.0000   +0.0000

401  box          +22.8600  +27.9400   +0.9525 $ unit cell (notpad)
```

```
          TR  -6.6675  +0.3175  +3.9688
              -5.6675  +0.3175  +3.9688
              -6.6675  +1.3175  +3.9688

$  Cocaine stash (in plastic bag)

  204  ecylinder   +1.9050  +1.7463        $ cocaine stash
              +6.1913  -6.1913
          TR  +0.0000  +0.0000  +0.0000
  205  ecylinder   +1.8256  +1.6669
              +6.1119  -6.1119
          TR  +0.0000  +0.0000  +0.0000

  404  ecylinder   +1.9050  +1.7463        $ unit cell (costsh)
              +6.1913  -6.1913
          TR  -13.1762  -8.2549  +1.4288
              -12.1762  -8.2549  +1.4288
              -13.1762  -7.2549  +1.4288

$  Sugar (in plastic bag)

  206  ecylinder   +1.9050  +1.7463        $ sugar bag
              +6.1913  -6.1913
          TR  +0.0000  +0.0000  +0.0000
  207  ecylinder   +1.8256  +1.6669
              +6.1119  -6.1119
          TR  +0.0000  +0.0000  +0.0000

  406  ecylinder   +1.9050  +1.7463        $ unit cell (sugbag)
              +6.1913  -6.1913
          TR  -0.1586  -8.2549  +1.4288
              +0.8414  -8.2549  +1.4288
              -0.1586  -7.2549  +1.4288

$  Rolled newspaper (newsprint)

  208  ecylinder   +1.9050  +3.8100        $ newspaper
             +15.2400  -15.2400
          TR  +0.0000  +0.0000  +0.0000
  209  ecylinder   +0.3175  +2.2225
             +15.2400  -15.2400
          TR  +0.0000  +0.0000  +0.0000

  408  ecylinder   +1.9050  +3.8100        $ unit cell (newpap)
             +15.2400  -15.2400
          TR  +0.0000  -12.3824  -0.6350
              +1.0000  -12.3824  -0.6350
              +0.0000  -11.3824  -0.6350

$  Boundary-crossing detectors (rectangular plates)

  500  box       +60.0000  +60.0000  +1.0000 $ pbcd assembly
          TR  +0.0000  +0.0000  -50.0000
  501  plane      +0.0000  +0.0000  +0.0000
              +0.0000  +0.0000  -1.0000
          TR  +0.0000  +0.0000  -50.0000
```

```
$  Position markers

  504   sphere      +0.5000                  $ source position
            TR   +0.0000   +0.0000 +147.4533

$  Problem boundary (rectangular box)

  999   box         +100.0000 +100.0000 +250.0000 $ boundary
            TR   +0.0000   +0.0000   +50.0000

GEOMETRY

  unit   345 shirts   -345
            TR  -11.1125   +4.1276   -0.6350
              -10.1125   +4.1276   -0.6350
              -11.1125   +5.1276   -0.6350

  unit   359 umbrll   -359
            TR   +0.0000   -8.2549   -2.5400
               +1.0000   -8.2549   -2.5400
               +0.0000   -7.2549   -2.5400

  unit   373 camera   -373
            TR  +13.0175  +11.4301   -2.5400
              +14.0175  +11.4301   -2.5400
              +13.0175  +12.4301   -2.5400

  unit   374 pbbook   -374
            TR  +13.0175   +2.8576   -3.1750
              +14.0175   +2.8576   -3.1750
              +13.0175   +3.8576   -3.1750

  unit   380 swknfe   -380
            TR  +13.0175   -3.9687   -3.6513
              +14.0175   -3.9687   -3.6513
              +13.0175   -2.9687   -3.6513

  unit   385 plexpl   -385
            TR  +10.2658   +0.7939   +0.0000
              +11.2658   +0.7939   +0.0000
              +10.2658   +1.7939   +0.0000

  unit   386 wrtset   -386
            TR  +17.0392   +0.7939   -0.6350
              +18.0392   +0.7939   -0.6350
              +17.0392   +1.7939   -0.6350

  unit   399 woolsw   -399 +200
            TR  +12.9117   +2.0639   +2.5400
              +13.9117   +2.0639   +2.5400
              +12.9117   +3.0639   +2.5400

  unit   401 notpad   -401
            TR   -6.6675   +0.3175   +3.9688
              -5.6675   +0.3175   +3.9688
```

```
            -6.6675   +1.3175   +3.9688

unit   404 costsh   -404
         TR  -13.1762   -8.2549   +1.4288
            -12.1762   -8.2549   +1.4288
            -13.1762   -7.2549   +1.4288

unit   406 sugbag   -406
         TR   -0.1586   -8.2549   +1.4288
             +0.8414   -8.2549   +1.4288
             -0.1586   -7.2549   +1.4288

unit   408 newpap   -408
         TR   +0.0000  -12.3824   -0.6350
             +1.0000  -12.3824   -0.6350
             +0.0000  -11.3824   -0.6350

sector 101 ccover   -101 +102 +105 +106
                    +107 +108
                    +109 +110
sector 102 alshel   -102 +103 +107 +108
sector 104 wdhndl    -104
sector 105 alhndl   -105
sector 106 alhndl   -106
sector 107 alhing   -107
sector 108 alhing   -108
sector 109 alltch   -109
sector 110 alltch   -110

sector 500 pbcd_a   -500 -501
sector 501 pbcd_b   -500 +501

sector 508 srcmkr   -504

fill   998

boundary    vacuum   +999

define unit 321  $  gun clips
   sector  121  ssbody   -121 +122 +123
   sector  123  wdbase    -121 -123
   sector  124  bull01   -124 +144
   sector  125  bull01   -124 -144
   sector  126  bull02   -126 +144
   sector  127  bull02   -126 -144
   sector  128  bull03   -128 +144
   sector  129  bull03   -128 -144
   sector  130  bull04   -130 +144
   sector  131  bull04   -130 -144
   sector  132  bull05   -132 +144
   sector  133  bull05   -132 -144
   sector  134  bull06   -134 +144
   sector  135  bull06   -134 -144
   sector  136  bull07   -136 +144
   sector  137  bull07   -136 -144
   sector  138  bull08   -138 +144
```

```
  sector 139 bull08  -138 -144
  sector 140 bull09  -140 +144
  sector 141 bull09  -140 -144
  sector 142 bull10  -142 +144
  sector 143 bull10  -142 -144
  fill  998

define unit 345 $ shirts (pistol)
  sector 111 ssbarl  -111 +112
  sector 113 ssbody  -113 +111 +120 +321
  sector 114 wdhndl  -114 +113 +321
  sector 115 sstgrd  -115 +116 +113 +114
  sector 117 sstrgr  -117 +113
  sector 118 sshamr  -118 +113 +111
  sector 119 sssigt  -119 +111
  unit  321 guncp1  -321
        TR  +0.0000  +0.0000  +0.0000
           +1.0000  +0.0000  +0.0000
           +0.0000  +1.0000  +0.0000
  unit  321 guncp2  -322
        TR  +8.8900  +2.5400  +0.0000
           +9.5971  +3.2471  +0.0000
           +8.1829  +3.2471  +0.0000
  sector 145 shirts  -145 +111 +113 +114
                     +115 +117 +118
                     +119 +321 +322
  fill  998

define unit 359 $ umbrella
  sector 146 alctrd  -146 +147
  sector 148 aledcp  -148 +146
  sector 149 plhndl  -149 +146
  sector 150 alsprd  -150
             or -151
             or -152
             or -153
             or -154
             or -155
             or -156
             or -157
  sector 158 nycovr  -158 +146 +150 +151 +152 +153
                     +154 +155 +156 +157
  fill  998

define unit 373 $ camera
  sector 160 plbody  -160 +161 +162 +163 +165 +166
                     +167
  sector 162 plvwfd  -162
  sector 163 pllens  -163 +164
  sector 164 gllens  -164
  sector 165 alspnd  -165
  sector 166 alwhll  -166 +165
  sector 167 alspnd  -167
             or -168
  sector 169 alplte  -169
  sector 170 sielec  -170
```

```
  sector 171 alfmcn   -171 +172 +167
  fill  998

define unit 374 $ paperback book
  sector 174 pabook   -174
  fill  998

define unit 380 $ switchblade knife
  sector 175 wdbody   -175 +178 +179
  sector 176 wdedcp   -176 +175 +179
  sector 177 wdedcp   -177 +175 +178 $ +179
  sector 178 ssmech   -178 +179
  sector 179 ssblde   -179
  fill  998

define unit 385 $ plastic explosive
  sector 181 wdbody   -181
  sector 182 sielec   -182
  sector 183 batt01   -183
  sector 184 batt02   -184
  fill  998

define unit 386 $ writing set
  sector 186 plcase   -186 +187
  sector 188 wdpncl   -188 +189 -191
  sector 189 grlead   -189 -191
  sector 190 alpcap   -190 +188
  sector 192 plplow   -192 +194 -198
             or -193 +194
  sector 195 alpupr   -195 +196 +197
  sector 197 alpcar   -197 -198
  fill  998

define unit 399 $ wool sweater
  sector 199 woolsw   -199
  fill  998

define unit 401 $ note pad
  sector 201 plshll   -201 +202
  sector 203 pappad   -203
  fill  998

define unit 404 $ cocaine stash
  sector 204 plabag   -204 +205
  sector 205 cocain   -205
  fill  998

define unit 406 $ sugar bag
  sector 206 plabag   -206 +207
  sector 207 gsugar   -207
  fill  998

define unit 408 $ newspaper
  sector 208 panews   -208 +209
  fill  998
```

```
picture cs m color  +50.0000   +0.0000 +175.0000 $ boundary (xz)
                    -50.0000   +0.0000 +175.0000
                    -50.0000   +0.0000  -75.0000

picture cs m color   +0.0000  -50.0000 +175.0000 $ boundary (yz)
                     +0.0000  +50.0000 +175.0000
                     +0.0000  +50.0000  -75.0000

picture cs m color   +3.8100   -3.8100   -0.6350 $ pistol (xy)
                     +3.8100  +12.0650   -0.6350
                    -15.5575  +12.0650   -0.6350

picture cs m color  +21.5900  -13.3350   -2.5400 $ umbrella (xy)
                    +21.5900   -3.1750   -2.5400
                    -21.5900   -3.1750   -2.5400

picture cs m color  +21.2725   +5.0800   -2.5400 $ camera (xy)
                    +21.2725  +16.5100   -2.5400
                     +4.7625  +16.5100   -2.5400

picture cs m color  +21.9075   -4.1275   -3.1750 $ book (xy)
                    +21.9075   +9.8425   -3.1750
                     +4.1275   +9.8425   -3.1750

picture cs m color  +21.9075   -7.7787   -3.6513 $ knife (xy)
                    +21.9075   -0.1587   -3.6513
                     +4.1275   -0.1587   -3.6513

picture cs m color  +16.6158   -8.2549   +0.0000 $ explosive (xy)
                    +16.6158   +9.8426   +0.0000
                     +3.9158   +9.8426   +0.0000

picture cs m color  +22.1192   -8.2549   -0.6350 $ writing set (xy)
                    +22.1192   +9.8426   -0.6350
                    +11.9592   +9.8426   -0.6350

picture cs m color  +21.9076  -12.6999   +2.5400 $ wool sweater (xy)
                    +21.9076  +16.8277   +2.5400
                     +3.9159  +16.8277   +2.5400

picture cs m color   +7.3025  -16.1925   +3.9688 $ note pad (xy)
                     +7.3025  +16.8275   +3.9688
                    -20.6375  +16.8275   +3.9688

picture cs m color   -4.4454  -12.6999   +1.4288 $ cocaine stash (xy)
                     -4.4454   -3.8099   +1.4288
                    -21.9080   -3.8099   +1.4288

picture cs m color   +8.5727  -12.6999   +1.4288 $ sugar bag (xy)
                     +8.5727   -3.8099   +1.4288
                     -8.8899   -3.8099   +1.4288

picture cs m color  +17.7800  -16.8274   -0.6350 $ newspaper (xy)
                    +17.7800   -7.9374   -0.6350
                    -17.7800   -7.9374   -0.6350
```

```
MIX

$  Density breakdowns for component materials (gm/cc):

   usezeroxs  $ substitute zero for unknown cross sections

   mat = 1   C      0.2222   $ cotton
             H      0.0311
             O      0.2467
   mat = 2   Al     2.6970   $ aluminum
   mat = 3   ss304  7.7940   $ stainless steel
   mat = 4   air    0.00129  $ air @ 20°
   mat = 5   C      0.3277   $ wood (12% moisture)
             H      0.0410
             N      0.0717
             O      0.3072
             H2O    0.0224
   mat = 6   Pb     11.3300  $ lead
   mat = 7   C      0.3881   $ gunpowder
             H      0.0380
             N      0.2263
             O      0.9477
   mat = 8   C      1.7780   $ graphite
   mat = 9   C      0.9675   $ polystyrene
             H      0.0755
             O      0.0070
   mat = 10  C      0.3184   $ nylon
             H      0.0490
             N      0.0619
             O      0.0707
   mat = 11  Si     1.2340   $ glass
             O      1.4060
   mat = 12  Si     1.1650   $ electronics
   mat = 13  C      0.6667   $ book paper
             H      0.0933
             O      0.7400
   mat = 14  C      0.1760   $ explosive (RDX & PETN)*
             H      0.0265
             N      0.2780
             O      0.5195
   mat = 15  Pb     5.6650   $ battery
             H2O    0.5000
   mat = 16  C      0.3098   $ wool
             H      0.0156
             N      0.0600
             O      0.1018
             S      0.0129
   mat = 17  C      0.5404   $ cocaine-HCl (0.90 c/cc)*
             H      0.0589
             N      0.0370
             O      0.1698
             Cl     0.0939
   mat = 18  C      0.3777   $ sugar (0.90 c/cc)
             H      0.0581
             O      0.4612
   mat = 19  C      0.3333   $ newsprint
```

```
        H       0.0466
        O       0.3700

ASSIGN-ML

 1   101 145 /
 2   102 105 106 107 108 109 110 146 148
     150 165 166 167 169 171 190 195 197 /
 3   111 113 115 117 118 119 121 178 179 /
 4   998 /
 5   104 114 123 175 176 177 188 /
 6   124 126 128 130 132 134 136 138 140 142 /
 7   125 127 129 131 133 135 137 139 141 143 /
 8   189 /
 9   149 160 162 163 186 192 201 204 206 /
10   158 /
11   164 /
12   170 182 /
13   174 203 /
14   181 /
15   183 184 /
16   199 /
17   205 /
18   207 /
19   208 /
 0   500 501 508

ASSIGN-MC

 1   Tan      $ cotton
 2   Gray     $ aluminum
 3   Moss     $ steel
 4   Sky      $ air
 5   Brown    $ wood
 6   Black    $ lead
 7   Yellow   $ gunpowder
 8   Black    $ graphite
 9   Black    $ polystyrene
10   Orange   $ nylon
11   Lime     $ glass
12   Rose     $ electronics
13   Brown    $ book paper
14   Yellow   $ explosive
15   Black    $ battery
16   Magenta  $ wool
17   Lavender $ cocaine-HCl
18   Purple   $ sugar
19   Tan      $ newsprint
 0   White    $ void
-1   Rose     $ absorber

SOURCE

$  The source model consists of a 0.20 cm diameter disk.

  nparticles     = 500000000
```

```
$  Source position geometries:

   define position  =  1  $  circular disk
                ss-disk   +0.0000  +0.0000  +147.4533
                      +0.0000  +0.0000  +146.4533
                      +0.1000

$  Source energy distributions:

   define energy   =  1  $  distribution @   0°
                neutron
                bin              4.703    37.200
                                4.813    38.500
                                4.921    39.900
                                5.028    41.300
                                5.134    42.600
                                5.240    43.900
                                5.345    45.100
                                5.449    46.400
                                5.553

   define energy   =  2  $  distribution @  25°
                neutron
                bin              4.487    21.000
                                4.586    21.100
                                4.683    21.200
                                4.779    21.200
                                4.875    21.200
                                4.970    21.200
                                5.065    21.200
                                5.159    21.100
                                5.252

   define energy   =  3  $  distribution @  40°
                neutron
                bin              4.180    10.500
                                4.264    10.300
                                4.346    10.100
                                4.428     9.880
                                4.509     9.640
                                4.590     9.390
                                4.670     9.150
                                4.750     8.930
                                4.829

   define energy   =  4  $  distribution @  50°
                neutron
                bin              3.927     7.620
                                3.998     7.500
                                4.068     7.400
                                4.139     7.320
                                4.208     7.230
                                4.278     7.120
                                4.346     7.050
                                4.415     7.000
```

4.483

define energy = 5 $ distribution @ 60°
neutron
bin 3.650 6.640
3.709 6.680
3.767 6.730
3.825 6.780
3.883 6.820
3.940 6.860
3.997 6.910
4.053 6.980
4.109

define energy = 6 $ distribution @ 70°
neutron
bin 3.366 6.250
3.412 6.350
3.458 6.460
3.504 6.550
3.550 6.640
3.595 6.720
3.640 6.800
3.685 6.880
3.730

define energy = 7 $ distribution @ 80°
neutron
bin 3.086 5.760
3.121 5.840
3.156 5.920
3.190 5.980
3.225 6.030
3.260 6.070
3.294 6.120
3.328 6.160
3.362

define energy = 8 $ distribution @ 90°
neutron
bin 2.821 5.170
2.846 5.170
2.871 5.180
2.896 5.170
2.921 5.160
2.946 5.140
2.971 5.120
2.995 5.110
3.020

define energy = 9 $ distribution @ 100°
neutron
bin 2.580 4.810
2.595 4.750
2.612 4.680
2.628 4.620

```
                    2.645   4.550
                    2.662   4.460
                    2.679   4.390
                    2.696   4.320
                    2.713

  define energy   = 10 $ distribution @ 115°
                neutron
                bin          2.269   5.390
                             2.275   5.270
                             2.282   5.150
                             2.288   5.040
                             2.296   4.930
                             2.303   4.810
                             2.311   4.690
                             2.320   4.590
                             2.328

$  Source time distributions:

  define time     = 1 $ steady state distribution
                steady

$  Source angular distributions:

  define angle    = 1 $ uniform distribution
               +0.0000 +0.0000 -1.0000
                distribution +1.000000000  1.000E+00
                        +0.984650738  1.000E+00

$  Source increments (1):

  increment 1.00000E+00 position   = 1 $ circular disk
                  energy     = 1 $ bin structure ( 0°)
                  time       = 1 $ steady state
                  angle      = 1 $ uniform dist.
                  importance = 1.00000E+00

WALK-COLLISION

  neutron
   region all
    energy    0.000 to    0.050   +0.950

DETECTOR

  number = pbcd01
   title = "Pbcd usrdet (energy bin #1) (scattered) (pbcd01)"
   usrdet pbcd region 500 region 501 passpvm 3.60000E+03
    counts $ weighted counts/pixel
    detbndry   +30.0000  -30.0000  -50.0000
           +30.0000  +30.0000  -50.0000
           -30.0000  +30.0000  -50.0000
    meshsize 200 200
    particle 1
    a-mask  0.0000 1.0000
```

```
  e-mask  1.5000 2.4999
  c-mask  1 250

number = pbcd02
 title = "Pbcd usrdet (energy bin #2) (scattered) (pbcd02)"
 usrdet pbcd region 500 region 501 passpvm 3.60000E+03
  counts $ weighted counts/pixel
  detbndry  +30.0000  -30.0000  -50.0000
         +30.0000  +30.0000  -50.0000
         -30.0000  +30.0000  -50.0000
  meshsize 200 200
  particle 1
  a-mask  0.0000 1.0000
  e-mask  2.5000 3.4999
  c-mask  1 250

number = pbcd03
 title = "Pbcd usrdet (energy bin #3) (scattered) (pbcd03)"
 usrdet pbcd region 500 region 501 passpvm 3.60000E+03
  counts $ weighted counts/pixel
  detbndry  +30.0000  -30.0000  -50.0000
         +30.0000  +30.0000  -50.0000
         -30.0000  +30.0000  -50.0000
  meshsize 200 200
  particle 1
  a-mask  0.0000 1.0000
  e-mask  3.5000 4.7029
  c-mask  1 250

number = pbcd04
 title = "Pbcd usrdet (energy bin #4) (measured)  (pbcd04)"
 usrdet pbcd region 500 region 501 passpvm 3.60000E+03
  counts $ weighted counts/pixel
  detbndry  +30.0000  -30.0000  -50.0000
         +30.0000  +30.0000  -50.0000
         -30.0000  +30.0000  -50.0000
  meshsize 200 200
  particle 1
  a-mask  0.0000 1.0000
  e-mask  4.7030 5.5530

number = pbcd05
 title = "Pbcd usrdet (energy bin #4) (scattered) (pbcd05)"
 usrdet pbcd region 500 region 501 passpvm 3.60000E+03
  counts $ weighted counts/pixel
  detbndry  +30.0000  -30.0000  -50.0000
         +30.0000  +30.0000  -50.0000
         -30.0000  +30.0000  -50.0000
  meshsize 200 200
  particle 1
  a-mask  0.0000 1.0000
  e-mask  4.7030 5.5530
  c-mask  1 250

number = bcd01
 title = "Standard bcd (measured)  (bcd01)"
```

```
    boundary counts 500 501 3.60000E+03
    drf-a normal +1.00000000 +1.00000000 +0.00000001 +1.00000000
            -0.00000001 +0.00000000 -1.00000000 +0.00000000
    bin energy neutron 401 [0.0000E+00 I 1.0000E+01] $ 0.025 MeV
     Elabel = "Neutron Energy (MeV)"
     Ylabel = "Differential Response (counts/Mev/inc)"

  number = bcd02
   title = "Standard bcd (scattered) (bcd02)"
   boundary counts 500 501 3.60000E+03
   drf-a normal +1.00000000 +1.00000000 +0.00000001 +1.00000000
            -0.00000001 +0.00000000 -1.00000000 +0.00000000
   mask-c 1 250
   bin energy neutron 401 [0.0000E+00 I 1.0000E+01] $ 0.025 MeV
    Elabel = "Neutron Energy (MeV)"
    Ylabel = "Differential Response (counts/Mev/inc)"

END
```

A.4 MCNP Code for Source-Shielding Simulation

Source-shielding design has been simulated in MCNP-4B. Following is the code used.

```
DD Neutron Shielding
c
c Cell Cards
1 0 -1
2 1 -1.0 1 -2
3 2 -13.6 2 -3
4 0 3 -4
5 0 4

c Surface Cards
1 so 5
2 sq 0.64 1 1 0 0 0 -1936 10 0 0   $b=44 a=55
3 sq 0.64 1 1 0 0 0 -2704 10 0 0   $b=52 a=65
4 sx 10 100

c Data Cards
mode n p
imp:n  1 1 1 1 0
imp:p  1 1 1 1 0
sdef DIR=d1 ERG FDIR d2 VEC=1 0 0
si1 h -1.0 -0.9397 -0.766 -0.5 -0.1736 0.1736 0.5 0.766 0.9397 1.0
sp1 d 0 4.68 11.38 11.66 9.61 11.27 13.5 12.5 17.34 13.56
ds2 h 1.657 1.714 1.956 2.203 2.662 3.26 3.94 4.59 5.065 5.24
f2:n 3
f12:p 3
f22:n 3
f32:p 3
de22 2.5e-8 1e-7 1e-6 1e-5 1e-4 1e-3 1e-2 1e-1 5e-1 1 2.5 5.0 7.0
df22 3.67e-3 3.67e-3 4.46e-3 4.54e-3 4.18e-3 3.76e-3 3.56e-3 2.17e-2 &
     9.26e-2 0.132 0.125 0.156 0.147
de32 0.01    0.1     0.3    0.7     1.0      5.0
df32 2.51e-3 4.01e-3 5.6e-3 1.03e-2 1.33e-2 6.65e-2
c
f5:n 85 0 0 10  $mrem/h; x=75
f105:p 85 0 0 10  $mrem/h
de5 2.5e-8 1e-7 1e-6 1e-5 1e-4 1e-3 1e-2 1e-1 5e-1 1 2.5 5.0 7.0
df5 3.67e-3 3.67e-3 4.46e-3 4.54e-3 4.18e-3 3.76e-3 3.56e-3 2.17e-2 &
     9.26e-2 0.132 0.125 0.156 0.147
de105 0.01    0.1     0.3    0.7     1.0      5.0
```

```
df105 2.51e-3 4.01e-3 5.6e-3 1.03e-2 1.33e-2 6.65e-2
c
f15x:n 60 43 10  $mrem/h; x=60
f115x:p 60 43 10  $mrem/h
de15 2.5e-8 1e-7 1e-6 1e-5 1e-4 1e-3 1e-2 1e-1 5e-1 1 2.5 5.0 7.0
df15 3.67e-3 3.67e-3 4.46e-3 4.54e-3 4.18e-3 3.76e-3 3.56e-3 2.17e-2 &
     9.26e-2 0.132 0.125 0.156 0.147
de115 0.01    0.1     0.3    0.7     1.0      5.0
df115 2.51e-3 4.01e-3 5.6e-3 1.03e-2 1.33e-2 6.65e-2
c
f25x:n 45 54 10  $mrem/h; x=45
f125x:p 45 54 10  $mrem/h
de25 2.5e-8 1e-7 1e-6 1e-5 1e-4 1e-3 1e-2 1e-1 5e-1 1 2.5 5.0 7.0
df25 3.67e-3 3.67e-3 4.46e-3 4.54e-3 4.18e-3 3.76e-3 3.56e-3 2.17e-2 &
     9.26e-2 0.132 0.125 0.156 0.147
de125 0.01    0.1     0.3    0.7     1.0      5.0
df125 2.51e-3 4.01e-3 5.6e-3 1.03e-2 1.33e-2 6.65e-2
c
f35x:n  30 60 10  $mrem/h; x=30
f135x:p 30 60 10  $mrem/h
de35 2.5e-8 1e-7 1e-6 1e-5 1e-4 1e-3 1e-2 1e-1 5e-1 1 2.5 5.0 7.0
df35 3.67e-3 3.67e-3 4.46e-3 4.54e-3 4.18e-3 3.76e-3 3.56e-3 2.17e-2 &
     9.26e-2 0.132 0.125 0.156 0.147
de135 0.01    0.1     0.3    0.7     1.0      5.0
df135 2.51e-3 4.01e-3 5.6e-3 1.03e-2 1.33e-2 6.65e-2
c
f45x:n 20 62 10  $mrem/h; x=20
f145x:p 20 62 10  $mrem/h
de45 2.5e-8 1e-7 1e-6 1e-5 1e-4 1e-3 1e-2 1e-1 5e-1 1 2.5 5.0 7.0
df45 3.67e-3 3.67e-3 4.46e-3 4.54e-3 4.18e-3 3.76e-3 3.56e-3 2.17e-2 &
     9.26e-2 0.132 0.125 0.156 0.147
de145 0.01    0.1     0.3    0.7     1.0      5.0
df145 2.51e-3 4.01e-3 5.6e-3 1.03e-2 1.33e-2 6.65e-2
c
f55x:n 10 62 10  $mrem/h; x=10
f155x:p 10 62 10  $mrem/h
de55 2.5e-8 1e-7 1e-6 1e-5 1e-4 1e-3 1e-2 1e-1 5e-1 1 2.5 5.0 7.0
df55 3.67e-3 3.67e-3 4.46e-3 4.54e-3 4.18e-3 3.76e-3 3.56e-3 2.17e-2 &
     9.26e-2 0.132 0.125 0.156 0.147
de155 0.01    0.1     0.3    0.7     1.0      5.0
df155 2.51e-3 4.01e-3 5.6e-3 1.03e-2 1.33e-2 6.65e-2
c
f65x:n 0 62 10  $mrem/h; x=0
f165x:p 0 62 10  $mrem/h
de65 2.5e-8 1e-7 1e-6 1e-5 1e-4 1e-3 1e-2 1e-1 5e-1 1 2.5 5.0 7.0
df65 3.67e-3 3.67e-3 4.46e-3 4.54e-3 4.18e-3 3.76e-3 3.56e-3 2.17e-2 &
```

```
     9.26e-2 0.132 0.125 0.156 0.147
de165 0.01    0.1     0.3    0.7     1.0      5.0
df165 2.51e-3 4.01e-3 5.6e-3 1.03e-2 1.33e-2 6.65e-2
c
f75x:n -15 62 10  $mrem/h; x=-15
f175x:p -15 62 10  $mrem/h
de75 2.5e-8 1e-7 1e-6 1e-5 1e-4 1e-3 1e-2 1e-1 5e-1 1 2.5 5.0 7.0
df75 3.67e-3 3.67e-3 4.46e-3 4.54e-3 4.18e-3 3.76e-3 3.56e-3 2.17e-2 &
     9.26e-2 0.132 0.125 0.156 0.147
de175 0.01    0.1     0.3    0.7     1.0      5.0
df175 2.51e-3 4.01e-3 5.6e-3 1.03e-2 1.33e-2 6.65e-2
c
f85x:n -30 51 10  $mrem/h; x=-30
f185x:p -30 51 10  $mrem/h
de85 2.5e-8 1e-7 1e-6 1e-5 1e-4 1e-3 1e-2 1e-1 5e-1 1 2.5 5.0 7.0
df85 3.67e-3 3.67e-3 4.46e-3 4.54e-3 4.18e-3 3.76e-3 3.56e-3 2.17e-2 &
     9.26e-2 0.132 0.125 0.156 0.147
de185 0.01    0.1     0.3    0.7     1.0      5.0
df185 2.51e-3 4.01e-3 5.6e-3 1.03e-2 1.33e-2 6.65e-2
c
f95x:n -45 38 10  $mrem/h; x=-45
f195x:p -45 38 10  $mrem/h
de95 2.5e-8 1e-7 1e-6 1e-5 1e-4 1e-3 1e-2 1e-1 5e-1 1 2.5 5.0 7.0
df95 3.67e-3 3.67e-3 4.46e-3 4.54e-3 4.18e-3 3.76e-3 3.56e-3 2.17e-2 &
     9.26e-2 0.132 0.125 0.156 0.147
de195 0.01    0.1     0.3    0.7     1.0      5.0
df195 2.51e-3 4.01e-3 5.6e-3 1.03e-2 1.33e-2 6.65e-2
m1 06000 1 01001 2
m2 82000 1
nps 1.5e7
```